EFFECTS OF MICROSTRUCTURE AND CHEMISTRY ON THE IGNITION SENSITIVITY OF PBX UNDER SHOCK LOADING

A Dissertation
Presented to
The Academic Faculty

by

Christopher Miller

In Partial Fulfillment
of the Requirements for the Degree
Doctor of Philosophy in the
School of Mechanical Engineering

Georgia Institute of Technology
December, 2019

EFFECTS OF MICROSTRUCTURE AND CHEMISTRY ON THE IGNITION SENSITIVITY OF PBX UNDER SHOCK LOADING

Approved by:

Dr. Min Zhou, Advisor
School of Mechanical Engineering
Georgia Institute of Technology

Dr. Julian Rimoli
School of Aerospace Engineering
Georgia Institute of Technology

Dr. Richard Neu
School of Mechanical Engineering
Georgia Institute of Technology

Dr. Cole Yarrington
Materials, Mechanics, and Tribology Department
Sandia National Laboratories

Dr. Ting Zhu
School of Mechanical Engineering
Georgia Institute of Technology

Date Approved: November 5, 2019

To Bonnie and my family

ACKNOWLEDGEMENTS

I would like to thank everyone who have guided me on my path through graduate school. I would like to thank my advisor, Dr. Min Zhou, for continually pushing me to pursue and publish the highest quality of research I could. You have taught me not only about science, but what it means to be a researcher and how best to share my ideas with others. I would like to thank the members of my thesis committee: Dr. Richard Neu, Dr. Julian Rimoli, Dr. Cole Yarrington, and Dr. Ting Zhu. I am grateful to both Dr. David Kittell and Dr. Cole Yarrington for serving as my mentors during my summer at Sandia National Laboratories. I also would like to thank Dr. Ryan Austin and Dr. Larry Fried who mentored me during my summer at LLNL.

I would not be where I am today without the support of all of my fellow graduate researchers throughout my studies. Thank you to Yaochi Wei, Amirrezza Keyhani, Ushasi Roy, Daniel Olsen, Chris Coffelt, Jay Shin, Dr. Barrett Hardin, Dr. Siddharth Avachat, and Dr. Chris Lammi. I would especially like to thank Dr. Seokpum Kim for taking the time to show me the ropes and bring me up to speed on research, even while writing his thesis. Much of my work is based on questions he made me consider. I am also grateful for the daily encouragement shown to me by Mr. Robert Manchurian. Finally, I would like to thank the members of my graduate fellowship, including Brooklyn Noble, Nathan Finney, Leo Kirsch, Amy Lovell, and Alison Saunders. This work was supported by the Department of Energy National Nuclear Security Administration Stewardship Science Graduate Fellowship program.

TABLE OF CONTENTS

LIST OF TABLES

LIST OF FIGURES

LIST OF SYMBOLS AND ABBREVIATIONS

Abbreviations

AL	Aluminum
ALE3D	Arbitrary Lagrangian Eulerian Three Dimensional (LLNL hydrocode)
APBX	Aluminized polymer-bonded explosive
ARB	Arrhenius reactive burn
CDF	Cumulative distribution function
CFEM	Coheisive finite element method
CJ	Chapman-Jouguet
CODEX	Cohesive Dynamics for Explosives
CTH	Sandia National Laboratories hydrocode
DoD	Department of Defense
DSRC	DoD Supercomputing Resource Center
EOS	Equation of State
HE	High explosive
HEM	Heterogeneous energetic material
HPC	High performance computing
HMX	Octahydro-1,3,5,7-tetranitro-1,3,5,7-tetrazocine
HNS	Hexanitrostilbene
HTPB	Hydroxyl-terminated polybutadiene
HVRB	History variable reactive burn
IG	Ignition and growth

IHE	Insensitive high explosive
JTF	Johnson-Tang-Forest
LAMMPS	Large-scale Atomic/Molecular Massively Parallel Simulator
ME	Microstructure explicit
MMEI	Mesoscale modeling of explosive initiation
PBX	Polymer-bonded explosive
PDF	Probability density function
PP	Pop plot
PPN	Pop plot number
RDD	run-to-detonation distance
RDX	1,3,5-Trinitro-1,3,5-triazinane
RVE	Representative volume element
SDT	Shock-to-detonation transition
SEMSS	Statistically equivalent microstructure sample sets
SGL	Steinberg-Guinan-Lund
SIA	Specific interface areas
TATB	1,3,5-triamino-2,4,6-trinitrobenzene
TMD	Theoretical maximum density
VE	Void explicit
ZND	Zel'dovich-von Neumann-Doring

Chapter 2 Symbols

CODEX HMX/Al Stress-Strain Model

$\hat{\tau}'$	Deviatoric part of the Jaumann rate of the Kirchhoff stress
L	Elastic moduli tensor
D'	Deviatoric part of the rate of deformation
D'_e	Elastic part of D'
D'_p	Viscoplastic part of D'
λ	Lamé's first constant
μ	Lamé's second constant
$\tilde{I}$	Fourth order identity tensor
$\bar{\sigma}$	Mises equivalent stress
$\dot{\bar{\varepsilon}}$	Equivalent plastic strain rate
τ'	Deviatoric part of the Kirchoff stress
$\bar{\varepsilon}$	Equivalent plastic strain
$\dot{\bar{\varepsilon}}_0$, $\dot{\bar{\varepsilon}}_m$	Reference strain rates
m , α	Rate sensitivity parameters for low and high strains respectively
σ_0	Quasi-static yield stress
ε_0	Reference strain
N	Strain hardening exponent,
T_0	Reference temperature
β , κ	Thermal softening parameters

Birch-Murnaghan EOS

τ_h Hydrostatic part of the Kirchoff stress

K_0 Bulk modulus

P Hydrostatic pressure

V_0 Initial volume

V Current volume

J Jacobian

F Deformation gradient

Estane Viscoelastic Model

σ Cauchy stress

ε^D Deviatoric portions of the Eulerian strain tensor

ε^H Hydrostatic portions of the Eulerian strain tensor

t Physical time

τ Reduced time

G Shear modulus

T_0 Reference temperature

G_∞ Steady-state shear mosulus

g_i Relative shear modulus of the i th term

N_p Number of terms in the Prony series

τ_i^p Relaxation time

Cohesive Finite Element Model

δ	Displacement between bulk elements
δ_0	Maximum elastic displacement
δ_c	Critical displacement beyond which the element is considered fractured
$S_{\max}$	Maximum traction strength

CODEX Ignition Criterion

$\dot{Q}_{chem}$	Heat generated due to chemical reaction
$\dot{Q}_{loss}$	Heat lost to surrounding elements
T	Hotspot temperature
d	Hotspot diameter
d_c	Critical hotspot diameter

CTH Flow Stress Model

σ_Y	Yield stress
$\dot{\varepsilon}_P$	Plastic strain rate
T	Temperature
σ_A	Athermal component of the flow stress
σ_T	Thermally activated component of the flow stress
C_1, C_2, U_K, σ_P	Material constants

Mie-Grüneisen EOS

p	Hydrostatic pressure

ρ_0 Initial density

ρ Current density

Γ_0 Grüneisen parameter

s Slope of the Hugoniot

E Internal energy

V_0 Reference volume

T Temperature

c_v Specific heat at constant volume

History Variable Reactive Burn Model

λ Extent of reaction

τ_0 Scaling constant

p Current pressure

p_i Threshold pressure for reaction

p_R, X, M, Z Reaction rate parameters

Chapter 3 Symbols

d_{avg} Average grain diameter

U_s Shock velocity

U_p Piston velocity

c Longitudinal wave speed

ρ Mass density

V_{fly} Flyer velocity

q	Pressure correction associated the artificial viscosity
l	Characteristic grid length
c_L, c_Q	Viscous parameters for the linear term and the quadratic term
c_v	Specific heat at constant volume
T	Temperature
k	Thermal conductivity
t	Time
η	Fraction of plastic work that is converted into heat
$\dot{W}^p, \dot{W}^{fric}$	Rate of plastic work and frictional dissipation
τ	Pulse duration
P	Shock pressure
E	Energy fluence
Π	Power flux
x_c, x_r	Rarefaction point and decay distance scaling parameter
J	James number
E_c, Π_c	Cutoff energy fluence and power flux in the modified James relation
Φ	Cumulative normal probability distribution
$\mathscr{P}$	Probability of ignition
μ, σ	Mean and standard deviation of the J distribution
τ_c	Material-dependent time-scale constant
R	Hotspot ignition risk determinant
T_i, T_c	Initial reference temperature and critical threshold temperature to observe a

Chapter 4 Symbols

U_p	Piston velocity
ρ	Mass density
t_{pulse}, τ	Pulse duration
P	Shock pressure
E	Energy fluence
Π	Power flux
W	Walker-Wasley number
n, C	Material constants for the Walker-Wasley relation
J	James number
E_c, Π_c	Cutoff energy fluence and power flux in the modified James relation
$\mathcal{P}$	Probability of ignition
μ, σ	Mean and standard deviation of the J distribution
τ_c	Material-dependent time-scale constant
α	Aluminum volume fraction

Chapter 5 Symbols

U_p	Piston velocity
H	Homogeneous sample
V	Homogeneous sample with voids
M	Microstructures sample
M+V	Microstructured sample with voids

x^* Run-to-detonation distance (RDD)

P_s Shock pressure

S, m Pop plot material parameters

D Pop plot number (PPN)

P_0, x_0^* Shock pressure and RDD below which no SDT occurs

$\mathscr{P}$ Probability of ignition

μ, σ_d Mean and standard deviation of the D distribution

Chapter 6 Symbols

U_p Piston velocity

H Homogeneous sample

V Homogeneous sample with voids

M Microstructures sample

M+V Microstructured sample with voids

x^* Run-to-detonation distance (RDD)

P_s Shock pressure

S, m Pop plot material parameters

D Pop plot number (PPN)

P_0, x_0^* Shock pressure and RDD below which no SDT occurs

$\mathscr{P}$ Probability of ignition

μ, σ_d Mean and standard deviation of the D distribution

X, s Sample mean and standard deviation of the Pop plot distribution at a given

$\mathscr{P}_{A<B}$ Probability of the RDD of *A* being shorter than the RDD of *B*

$p_{A<B}$ Probability density of the RDD of a random sample in distribution being

SUMMARY

The ignition sensitivity of heterogeneous energetic materials subject to shock loading is analyzed using both a Lagrangian and Eulerian computational framework. The specific focus here is on the various microstructure heterogeneities (including cracks, granular anisotropy, voids, and aluminum additives) and their relative contributions to the development of critical hotspots and macroscale detonation behavior characteristics, such as the run distance to detonation. A probabilistic approach is developed by generating statistically equivalent microstructure sample sets (SEMSS) and measuring the ignition behavior of each one under similar impact conditions. By varying the material and microstructural characteristics in a controlled fashion, the contribution to ignition of each specific type of microstructural defects is rank-ordered. Thousands of simulations, using dozens of microstructures, are performed on high performance computing (HPC) clusters, and all of these results are combined to create predictive, probability maps of material response over entire regimes of shock loading.

The Lagrangian-based cohesive finite element method (CFEM) is used to track material response prior to the onset of chemical reaction. Hotspots are categorized as critical or non-critical based on chemical kinetics calculations and if a particular density of critical hotspots is achieved, the sample is assumed to reach ignition. A probability threshold is proposed based on a modified form of the Hugh James and Walker-Wasley energy-based ignition criterions. The computations focus on both 100% packed energetic grains (HMX) as well as aluminized polymer-bonded explosives (APBXs). It is found that increasing the HMX grain size as well as increasing the volume fraction of aluminum

particulates decreases the material's sensitivity to ignition. The exact physical mechanisms governing the development of hotspots are quantified, and the friction resulting from transgranular and intergranular fracture is found to be the dominant dissipation mechanism.

The Sandia National Laboratories Eulerian hydrocode, CTH, is then used to simulate the entire shock to detonation transition (SDT) of pressed HMX, and the material sensitivity is ranked based on distance the shock wave travels before the detonation wave fully forms. A range of impact velocities are simulated to examine a wide range of potential shock pressures and the resulting run-to-detonation distances (RDDs) are predicted as a function of this shock pressure (commonly referred to as a Pop plot). The initial probability analysis used in the Lagrangian framework is expanded upon to generate a predictive map of the SDT threshold. This analysis is carried out in both two dimensions (2D) and three dimensions (3D), and it is found that 2D results have a wider variation among data, indicating the necessity of both a probabilistic framework and further 3D modeling efforts in the future. The probability thresholds proposed in this study serve as a useful design metric and may directly influence future shock experimentation as well as the development of new insensitive high explosives.

CHAPTER 1. INTRODUCTION

1.1 Background and Motivation

The study of high impact loading and resulting ignition of energetic materials as a field of research has grown substantially over the past few decades. By better understanding the nature of energetic initiation, explosives can be custom designed and tailored for specific purposes. In particular, the idea for an insensitive high explosive has been of great interest to the shock physics community. In order to fully analyze the physics governing the ignition of high explosives (HEs) under impulse loading, both experimental data and multiscale simulation modeling are required.

A common type of HE is a polymer-bonded explosive (PBX), which consists of energetic crystals mixed with a polymer binder. PBXs were first developed in 1952 at Los Alamos National Laboratory (LANL) and have many potential advantages over normal HEs. Primarily, the polymer binder can act as a shock absorber, which makes them less prone to accidental detonation [1, 2]. This in turn makes them far safer to machine into specific shapes. A typical PBX usually consists of anywhere between 5%-40% polymer by mass, with the remaining material belong to the explosive crystals. Some common energetics used include HMX (Octahydro-1,3,5,7-tetranitro-1,3,5,7-tetrazocine), RDX (1,3,5-Trinitro-1,3,5-triazinane), TATB (1,3,5-triamino-2,4,6-trinitrobenzene), and HNS (Hexanitrostilbene). The polymer matrix in the PBX, once cured, can serve as fuel to the detonation, however the initial ignition of the PBX stems from the explosive crystals [3]. Due to this, there is a trade-off between the benefits associated with PBXs (such as reduced

ignition sensitivity) and the costs to performance (since adding more binder means there is less room for explosive crystals, thereby lowering the strength of the explosion). Some common binders used in PBXs include Estane, HTPB (hydroxyl-terminated polybutadiene), and Viton [4].

One of the longstanding challenges within the field of energetic materials is making accurate predictions of macroscopic ignition safety as well as performance, using fundamental material attributes at lower size scales. For a high-speed impact scenario (~km/s), it is desirable to know what the likelihood is for ignition to occur – this assessment relates to safety and reliability. On the other hand, it is also important to quantify the minimum time and distance from the onset of impact to the development of steady state detonation – the shock-to-detonation transition (SDT) – this assessment relates to the performance of a material. Given the broad range and variability of different impact scenarios, these assessments must be carried out under well-characterized conditions to allow applications to the varying scenarios via macroscopic state variables such as pressure, energy, loading rates, and distance. It is also understood that a heterogeneous energetic material (HEM) will exhibit greater sensitivity to shock than a corresponding homogeneous material, as material heterogeneities and defects enhance localized deformation, heating, failure, and chemical reactivity.

Specifically, the heterogeneous SDT process [5, 6] is fundamentally different than what occurs during the shock initiation of a homogeneous explosive, such as liquid nitromethane [7] or hydrogen peroxide [8]. When homogeneous explosives are shocked, they are heated to a single bulk temperature immediately following the leading shock wave.

When this bulk temperature is sufficiently high (i.e. for a thermal runaway to occur), a super-detonation wave forms in the material that was held at elevated temperatures the longest [9], usually near the interface between a homogeneous explosive and a projectile/impactor. The super-detonation wave must overtake the leading shock before a steady detonation is reached. Consequently, this initiation mechanism underlies the reason as to why homogeneous explosives appear as relatively shock insensitive compared to heterogeneous ones; a critical ignition temperature must be reached during the initial shock or impact that is based on the chemical activation energy (and it is typically higher for solids than liquids). Over the times and distances associated with the SDT process, homogeneous explosives are mostly treated with a continuum modeling approach, using the appropriate mixture theories and rate laws [10].

In contrast, when a heterogeneous explosive is shocked, the SDT process is dominated by the details of the heterogeneous microstructure that lead to heterogeneous reactions. A continuum model treatment suffers from a loss of detailed material information at scales below the resolution of the computational elements or cells. In this case, the average (shocked) bulk temperature is too low for a super-detonation wave (e.g., see [11]); however, it is known that material heterogeneities can cause energy to be localized into regions known as hot spots [12] – it is at these sites where the chemical reaction begins. A successful, heterogeneous SDT results in the more gradual build-up of reaction behind the leading shock wave, which then strengthens the leading shock until it transitions to a detonation wave without any overshoot.

Thus, a pressed, porous explosive is more sensitive to shock and will detonate in less time and distance than a pure explosive crystal, or a homogeneous liquid explosive such as nitromethane, under similar loading conditions. The increased sensitivity of HEMs is a direct result of shock wave interactions with the heterogeneous microstructural features such as small cracks, voids, and discontinuities in the forms of boundaries and interfaces between constituents (binders, grains, metal particles, and oxidizer granules). These heterogeneities cause energy to be localized into regions known as hot spots - it is at these sites where the chemical reaction also begins. These microstructural features can be unique for certain HEMs, and result from available manufacturing and processing methods that must be employed. Typically, microstructural features range in size from tens of nm to hundreds of μm, and sometimes even as large as mm. For SDT, these features play a critical role in determining the explosive's shock sensitivity (i.e., safety and reliability) as well as performance. For example, Welle et al. [13] showed an empirical link between the microstructure and shock initiation behavior of neat HMX via the class of the material (class 3 vs. 5). The existence of this kind of a link was previously hypothesized by Baer [14] who used realistic three-dimensional HEM microstructures in a hydrocode simulation. Hence, both experiments and computations indicate that the overall SDT behavior is influenced by the processes occurring at the meso or grain scale.

Despite such general knowledge that HEM microstructures localize shock wave energy to form hot spots, there is little consensus as to the relative importance of the different hot spot mechanisms, or as to which mechanisms are active in different loading and material regimes. The hydrodynamic hot spot model, as introduced by Mader [15], was one of the very first to consider pore collapse and jet impingement following a shock wave;

this raises the local temperature higher than the bulk (i.e., Hugoniot) temperature. However, more recent pore collapse models by Austin et al. [16] show that the inclusion of a viscoplastic crystal model will lead to shear banding and chemical reaction around the site of the pore. Regardless of the fidelity and the type of different models used, all direct numerical simulations of shock-induced hot spots still require an explicit representation of the material microstructure. With current progress in the field, it is now possible to calculate the interactions of shocks with a much larger volume of the microstructure, which has led to a flurry of recent publications surrounding mesoscale modeling of explosives initiation (MMEI) [17-23]. Historically, these mesoscale simulations were carried out at the micron-scale, with the aim of predicting the effects that the microstructure has on the shock response of the material. However, this scale is much smaller than the scale of the full SDT process, which is observed over a few mm and may take several microseconds to complete. In addition, this scale is also well below the scale of heterogeneities on the order of hundreds of microns or even mm as noted earlier of many common HEMs.

The necessity of a large-scale SDT simulations with explicitly defined microstructure is of paramount importance to fully understanding the ignition sensitivity of an HE. In order to achieve such larger scale simulations without them becoming prohibitively computationally expensive, there is a strong need to determine which microstructural effects are important to consider at various loading intensities or stages of detonation. The work presented in this thesis is focused on answering the question of relative importance of both microstructural and chemical effects when considering the ignition of HEs.

1.2 Process of Ignition

Understanding the physical mechanisms governing the ignition behavior of high explosives (HEs) is a critical challenge when designing insensitive munitions. The most commonly accepted ignition theory involves recognizing the development of hotspots, or localized areas of high temperatures. These hotspots lead to the onset of chemistry [14, 24-26] and are often the results of concentrated mechanical energy dissipation, usually due to the presence of material defects or microstructure heterogeneities. Some of the most common forms of heat generation leading to hotspots are pore collapse, inter-granular and trans-granular fracture followed by frictional sliding, shear banding, and bulk shock heating [27]. As the temperatures of hotspots rise, they may surpass a critical threshold where the heat generation due to exothermic chemical reactions exceeds the rate of heat lost to the surrounding material due to conduction [28]. On the other hand, hotspots may be quenched by rarefaction waves traveling behind the shock front. Once a hotspot ignites, the chemistry leads to thermal runaway, resulting in melting and transformation to gas phases. This chemical process is accompanied by intense and rapid pressure increases which cause shockwaves to radiate from the hotspot ignition sites, leading to criticality at other sites. This avalanche event ultimately results in the formation of a detonation wave and the shock-to-detonation transition (SDT) when the detonation front catches up with the shock front. The distance the shock wave front travels before overtaken by the detonation wave front is known as the run distance to detonation or run-to-detonation distance (RDD) and is a common metric used to gauge the sensitivity and explosive potential of an HE in the form of a Pop plot [29].

Pore collapse has been studied as one of the main hotspot formation mechanism under shock loading. Bourne and Milne [30] studied possible ignition mechanism during pore collapse for a shocked material. The focus of their research, however, was not on stress concentration at the pore, but rather the temperature rise of the gas encapsulated in the pore. Bourne and Field [31] found that the hydrodynamic pressures generated by high-speed jetting during cavity collapse causes the ignition. Austin et al. [32] used ALE3D coupled with a reactive model, and studied the effect of stress concentration at a pore under shock loading, accounting for shear banding on crystallographic planes. Yarrington et al. recently studied the detonation or quenching of a continuum HNS based explosive incorporating a statistical distribution of randomized void sizes and material locations using CTH [23].

Heat generation due to frictional dissipation also affects the material sensitivity. Chidester et al. [33] experimentally tested PBX under low velocity impact, and measured the threshold velocity for reaction. They obtained the frictional coefficient based on frictional work calculation. Chaudhri [34] observed reaction front of β-lead azide using high-speed camera, and found that reaction-generated stress wave induces new reaction site ahead of the existing reaction front, and the new reaction is caused by frictional dissipation. Browning and Scammon [35] coupled three relations: inter-granular frictional dissipation model, chemical kinetics model, and heat transfer equation, and obtained time to ignition and velocities required for reaction. Gruau et al. [36] performed experimental impact tests on PBX and compared the results with numerical results adopted from Browning and Scammon [35]. Curtis et al. [37] used a similar test configuration as Gruau et al. [36] (Steven Test) in their numerical study, and found that friction substantially affects the ignition behavior. Specifically, Barua et al. [38-40] analyzed the energy

dissipation in PBX and observed that frictional dissipation is the dominant heating mechanism.

Another type of material heterogeneity that induces hotspot formation comes from a microstructure morphology such as grain sizes, shapes, and grain-binder interactions. Czerski and Proud [41] studied the effect of grain shapes and size on material sensitivity. They performed a Gap test on RDX granules and failed to observe any clear difference of sensitivity between the sizes of 10-30 μm and 100-300 μm. However, they found that grain shape influences on the sensitivity. Grains that have greater surface roughness with many dimple-like features showed more sensitive results. Bardenhagen et al. [42] analyzed microstructure morphology of a mock PBX (sucrose/HTPB) in 3D using X-ray microtomography, and obtained the bimodal grain size distribution. Skidmore et al. [43] compared the grain size distribution of HMX before and after manufacturing PBX 9501, and found that the peak volume fraction of large particles among bimodal size particles shifted toward smaller diameter, indicating the press processing breaks the large particles. Swallowe and Field [44] carried out drop-weight sensitivity tests on PBXs with different types of binder, and concluded that the mechanical interactions between a binder and energetic crystals influence on the material sensitivity. Rimoli et al. studied potential homogeneous ignition mechanisms for hotspots and found that lamellar structures formed at the sub-grain level of PETN as the result of slip lines led to higher local temperatures than predicted by traditional crystal plasticity models [45]. Welle et al. [13] studied microstructural effect on ignition of pressed HMX. The authors measured specific surface area and void distance distribution for different types of HMX microstructure, and plotted

the ignition criteria on James space (power flux – energy flux). The authors found that the energy threshold is influenced by the microstructure.

All of these mechanisms play an important role in the generation of hotspots. Once the temperature at the hotspot increases enough to overcome the activation energy of the exothermic chemical reaction, then the hotspot location becomes an initiation site. However, it is also possible that a hotspot may not lead to ignition depending on its characteristics. Field et al. [27] used the concept of "critical hotspot" which refer to hotspots which become self-sustaining, and provided the variables that determine the characteristics of critical hotspots – hotspot size, temperature and duration. If a hotspot cannot generate enough heat from its exothermic chemical reactions to cover the loss of heat away from the hotspot due to conduction, the result is a quenched hotspot. Bowden and Yoffe [12, 46] showed that the hotspot needs to have the size of 0.1-10 μm, the duration of 10^{-5}-10^{-3} s, and the temperature higher than 700K.

The concept of "criticality threshold" has been further developed by several researchers, especially focusing on the hotspot size-temperature threshold for thermal runaway. Semenoff [47] obtained a solution of the heat diffusion equation with heat generation due to reaction. Frank-Kamenetskii [48] solved the same heat conduction equation but with varying temperature distribution. Based on the works from Semenoff [47] and Frank-Kamenetzky [48], Thomas [49] studied the effect of surface cooling. The author used one-step zero-order Arrhenius reaction equation together with heat diffusion equation, assuming steady state. Boddington et al. [50] considered the amount of reactant consumption when using chemical reaction, and obtained the critical threshold. Tarver et

al. [28] developed 3-step chemical kinetics models for HMX and TATB decomposition, and obtained the critical size-temperature relations. Later, Tarver et al. [51] further developed the model and proposed 4-step chemical kinetics model for thermal decomposition of HMX. Henson et al. [52] compiled experimental data of temperature-ignition time and obtained a linear relationship on log time-inverse temperature scale over a large range of time (from nanoseconds to a day) and proposed a chemical decomposition model and parameters are calibrated based on the relationship obtained. Walker and Wasley [53] took a different approach to obtain the criticality. Instead of determining critical hotspot threshold, they focused on the critical energy flux input on the material, and obtained the empirical threshold criteria known as $P^2\tau = \text{constant}$. James [54] further developed this empirical threshold by including energy cutoff.

1.2.1 Effect of Aluminum

Aluminized HMX/Estane PBX has historically been used because of its higher net energy output which increases post-detonation blast performance as compared to nonaluminized PBX. Aluminum was first patented to increase explosive performance by Roth in 1900 [55], and over time experiments have optimized the volume fraction of aluminum particulates required to maximize explosive power [56] at around 20%. Reaction of Al is, however, relatively slow due to the oxidized coating of Al particles which have high melting point (2300K) that impedes the reactivity [56]. Therefore, aluminium in explosive composites behaves like an inert particle in the initial detonation zone. Oxygen-containing molecules in the reacted products from the decomposition of energetic solids undergo a secondary reaction process with aluminium [57]. This two-step process enhances

the post-detonation performance of aluminized PBX. Grishkin et al. [57] found that the detonation velocity of explosives (RDX and HMX) decreases as aluminium content increases, but the propulsion action of the explosives increases with the addition of Al up to 7-14% and decreases, indicating there is an optimum range of aluminium content. The heat of explosion also increases as aluminum is introduced, which allows the explosive to maintain its total output power while still being less sensitive to ignition [58]. Gogulya et al. [59] measured pressure and temperature of HMX/Al mixture, and observed two-peak structure in pressure profiles. The temperature profiles the authors obtained indicate that the energy absorbed for aluminium activation is compensated for by heat release from aluminium reaction. Antić and Džingalašević [60] suggested that aluminium does not behave as an inert material, but partially oxidises in the detonation wave front, which contradicts previously reported observations [57]. However, it is still widely accepted that aluminium does not react at the detonation front under moderate or weak shock loading.

1.2.2 Material Shock Response

If particle speed of a material is higher than the wave speed of its uncompressed state, a shock wave forms. Under shock loading, the response of the material shows interesting characteristics that the response under low intensity loading does not. For many solid materials, however, these characteristics are often observed even when the particle speed is less than its wave speed of uncompressed state. One example of shock characteristics is a sharp rise of stress wave front. Even if a gradual impact wave is imposed on the surface, the stress wave front becomes stiffer as it propagates [61], because the wave speed of highly compressed part is faster than that of less compressed part of the material. Ideally, the

stiffening of the wave front becomes infinitely thin, which may result in numerical instability during simulations. The concept of adding "artificial viscosity" is proposed by von Neumann and Richtmyer [62], to assign a finite width of stress rise at the shock front. Introducing a finite width at the shock front provides not only numerical stability but also an accurate representation of the propagating shock front [63].

Modeling of material behavior under high pressure requires an accurate equation of state (EOS), which provides a relation between state variables of the material such as pressure, specific volume, and temperature. Some of the widely used EOS models in modelling shocked material are Mie-Grüneisen EOS [64] and Birch–Murnaghan EOS [65]. Measurement of pressure-volume relation called shock Hugoniot curve provides useful information for parameter fittings of other EOS models. Hugoniot $P-V$ relation is also a simple type of EOS, and it can be transformed to other types of Hugoniot relations with different variables such as particle speed or shock speed using the jump conditions [66]. The Hugoniot relations commonly used are: $P-V$ (pressure-volume), $P-U_P$ (pressure-particle speed), and U_S-U_P (shock speed-particle speed). Using Chapman-Jouguet (CJ) theory [67], we can determine the condition of discontinuity at steady 1-D detonation front, assuming the detonation reaction zone is infinitesimally thin. The CJ point lies on the intersection of Hugoniot $P-V$ curve (Rankine-Hugoniot relation) of reacted material and Rayleigh line. A theory of Zel'dovich-von Neumann-Doring (ZND) condition is an extension of CJ theory with a consideration of finite reaction zone at the detonation front [68].

1.2.3 Chemistry and Reactive Burn Models

One of the most common HEs is Octahydro-1,3,5,7-tetranitro-1,3,5,7-tetrazocine (HMX), and is the primary HE studied in the following chapters. Due to this, the chemistry discussed here will be limited in scope to HMX in particular.

Many models have been proposed [69] for the development of hotspots. The effects of chemical reactions are often represented by Arrhenius-type kinetics models [70] which are calibrated using experimental data [71, 72], DFT/chemical kinetics calculations [73, 74], and results of molecular dynamics simulations [22]. For example, Mader [75] modeled detonation initiation and propagation of homogeneous HEs along surfaces. Once the hotspot temperature exceeds the activation energy, the granular HMX in PBX begin to decompose. The most common, stable form of HMX is its β-phase, a monoclinic structure [76]. Under high pressures and temperature, the β-phase HMX thermally decomposes into a stable hexagonal structure state, δ-phase. This transition occurs at pressures above 0.2 GPa. Karpowicz and Brill [77] found the conversion between β-phase and δ-phase is dependent on β-HMX particle size, with β-HMX being more stable at smaller particle sizes. Both α and γ phases of HMX exist, but are less stable then either β-HMX or δ-HMX at ambient and high pressures and temperatures [78].

Several different chemical reaction sequences involving the transformation of HMX and RDX into their product gases have been proposed [79-81]. McGuire and Tarver [82] proposed a 3-step chemical kinetics model based on the slowest reaction rates in the system. The first major step involves the breaking of the carbon and nitrogen bonds, which leads to molecular reorganization and the creation of NO_2 radicals. Finally the major

exothermic part of the reaction comes from the decomposition of HMX into its final gas products: H_2O, CO_2, CO, and N_2. Henson et al. [52] developed a first order chemical kinetics model which fits the decomposition of β-HMX to δ-HMX and then to its initial intermediaries: NO_2, CH_2O, and HCO. In his model, these initial reactions account for the majority of HMX exothermic chemical heat generation.

Modeling chemical reaction using simulation is a non-trivial task. Since the time rates of changes of physical quantities in a detonation are extremely high and the RDDs for different materials are on the order of millimeters, very short times steps and large sample sizes are required to capture the full shock loading, development of hotspots, reaction initiation, formation of detonation, and the ultimate SDT, making simulations very computationally expensive. For heterogeneous materials, the challenge is even more formidable because very fine meshes are required to resolve material microstructure and defects such as voids. It is because of these reasons, fully resolved mesoscale simulations of SDT at overall sample sizes on the order millimeters have been rare.

To partly circumvent this computational issue, phenomenological models have been used. One such model is the Ignition and Growth model of Lee and Tarver [83, 84]. This approach relates the chemical reaction rate to the local pressure and reaction progress variables. Other common models include the Forest Fire [10, 85] and JTF [11] models. These reactive burn models have become a common tool for simulating detonation at reasonable computational cost, as they do not account for microstructure morphology. The History Variable Reactive Burn (HVRB) model expresses the chemical reaction rate as a function of a time integral of the local pressure in the material [86, 87]. These models are

just a few examples of the many ways [35, 52, 88-93] to account for the effects of chemical reactions on hotspot ignition and growth, formation of detonation waves, and the SDT. There is a common tradeoff between accuracy and simulation time or simulation scale. For this reason, many attempts to accurately model the ignition of HMX and subsequent chemical reaction are generally performed on nanoscale size samples. The Lawrence Livermore Nation Lab code ALE3D excels at handling both the mechanical deformation due to phase change, as well as the chemical kinetics itself using the program CHEETAH [94]. Larger scale simulations have a tendency to trade numerical accuracy for calculation size, as trying to implement both becomes computationally unfeasible with modern capabilities.

1.3 Computational modeling of PBXs

With the ever increasing prominence of high performance computing (HPC) and the development of material models, increasingly sophisticated simulations are able to capture local material behavior that remain difficult to study experimentally. Some recent approaches to mesoscale modeling include work by Jackson et al. [21], which utilizes a density-based kinetics model, and a power deposition term in the energy equation to phenomenologically represent discrete hot spots. Comparison studies are also given to show the relative importance of the number density of hot spots, the microstructure of the crystalline pack, and other numerical parameters. In addition, Wood et al. [22] examined the role that the constitutive model plays in a mesoscale calculation by using the atomistic code, LAMMPS, to train a strain rate-dependent Steinberg-Guinan-Lund (SGL) viscoplastic strength model. Two mesoscale simulations were then run with and without

the SGL model turned on (i.e., hydrodynamic only), where it was found that an increase in the shocked temperature distribution occurs at lower impact velocities (less than ~1 km/s) if the SGL model is in use. Hence, strong shock initiation (i.e., several GPa of pressure) is most likely a purely hydrodynamic process. Finally, Yarrington et al. [23] have shown the full SDT process for a pressed porous explosive with nanoscale features in two dimensions. These large Eulerian calculations make use of a representative microstructure and a tuned Arrhenius-type burn model to match experimental results. Although the full computational domain was never shown in the paper, the run-to-detonation simulations employed a two-dimensional, 10 μm by 200 μm rectangular mesh with a total aspect ratio of 20:1 (which is among the highest aspect ratios ever published). These simulations also consisted of 80 million finite volume elements. Such large computational domain sizes appear to be more accessible in a pure Eulerian hydrocode, rather than one that is Lagrangian or arbitrary Lagrangian-Eulerian (ALE). Yet, there are still advantages and disadvantages to all three types of numerical methods.

Mesoscale models, to various degrees, resolve material heterogeneities, defects, and hotspot development under conditions of various mechanical, thermal, or electromagnetic excitations [19, 95-100]. The energetics community has been developing new ways to characterize microstructure and microstructure effects on the ignition and detonation of HEs. A few are mentioned here as examples. Wei et al. [101] studied the effects of material defects in the forms of interfacial debonding and grain cracks using a cohesive finite-element based Lagrangian approach. Rai et al. [102] analyzed the collapse of a void under shock loading using an Eulerian framework. Austin [16, 32] used an arbitrary Lagrangian-Eulerian approach (ALE3D) to study melt lines and shear banding following pore collapse.

Yarrington et al. [23] studied the SDT in HNS, accounting for a large population of randomly distributed nano pores whose statistical attributes track those of an experimentally scanned sample. The predicted threshold velocity required to cause detonation matches experimental measurement. The success can be partly attributed to the resolution of the mesoscale void structure and the calibration of the chemistry model to MD data [22]. These models are either 2D or at the overall sample scale of microns or tens of microns.

Baer et al. [103] are the first to carry out such 3D simulations using CTH, the Sandia National Labs solid mechanics code. The analysis concerned in the compaction of granular HMX in a cubic millimeter volume consisting of approximately 1900 grains under a loading piston speed of 1000 m/s. The local pressure based HVRB was used. Due to computational cost, the calculations at lower load intensities could not be continued long enough to reach SDT. Reaugh et al. [104] used ALE3D to analyze the response of a 300 μm × 300 μm ×300 μm block of PBX and found that a pressure-dependent deflagration chemistry model yielded better results than an Arrhenius-type hotspot growth model. Recently, Rai and Udaykumar [105] modeled the local effects of pore collapse in a homogeneous 3D HMX block 1.3 μm × 4 μm × 12 μm in size and found higher sensitivity in 3D than in 2D. Jackson et al. [21] used a phenomological model with energy deposition representing the effect of voids to study the effects of shock pressure on initiation times in a PBX setting. A reactive burn model instead was used. Due to computational cost, much of the work in the energetics community so far uses two-dimensional frameworks, are at micron/sub-millimeter scales, or involve various degrees of homogenization or phenomenological treatment. To more realistically capture the 3D nature of material

microstructure and heterogeneity configurations, to resolve the length scale of physical events such as the SDT of HE under shock loading, and to directly bridge the mesoscale and the macroscale, there is a strong need for fully 3D models that explicitly resolve mesoscale material structures (microstructures or material heterogeneities and voids) as well as relevant thermo-mechano-chemical processes. Ultimately, such 3D models can also shed light on if and how 2D and 3D models differ possible inadequacies of 2D models.

1.4 Modeling Ignition Thresholds

Broadly speaking, the modeling of shock ignition at the mesoscale level is typically carried out as a part of modeling shock-to-detonation transition (SDT). There are two approaches, depending on whether hotspots are explicitly treated or not. In the literature, the phrase “shock initiation” is often used to emphasize the transition to detonation [69]. The first approach involves treating hotspots explicitly based on a chosen mechanism of energy localization [14] (e.g., predominantly plastic pore collapse). The second approach does not involve treating hotspots explicitly, instead ignition is treated via a numerical switch to a burn model (rate law) in large-scale engineering calculations [83]. Both approaches have two basic features. The first is an assumption on the internal energy function (equation of state). The most common is a mass-weighted sum of constituent internal energies which contains the fraction of reacted explosive mass (called progress variable) and heat release from chemical reaction. The second is the rate law that controls the evolution of “burn” via the progress variable. This second approach does not describe the mechanisms of ignition or hotspot evolution. However, it is known that these burn models can be calibrated to match 50% threshold sensitivity of high explosives [106].

To summarize some of the recent MMEI efforts aimed at shock initiation, Handley et al. [17] published a review article that encapsulates the mesoscale modeling approach; the review also includes many of the advances made through 2017. Yet, in attempting to translate all of the lessons learned from mesoscale modeling to the next higher scale (i.e., continuum burn models), several gaps were identified that remain unsolved to this day. Note that continuum reactive burn models do not currently treat the mechanisms of ignition or hot spot evolution directly. Elsewhere, Rai and Udaykumar [18] have demonstrated the feasibility of an image to computation approach for mesoscale simulations of HMX, using detailed material models and chemistry based on the Henson-Smilowitz multi-step kinetic mechanism. Their mesoscale simulations show that hot spots may or may not lead to initiation, based on whether the HMX is class 3 or 5. However, this ignition behavior is sub-detonative, and it does not yet represent the full SDT process. Browning and Scammon [35] established an ignition model based on inter-granular frictional dissipation, chemical kinetics, and heat transfer, and obtained the time to ignition and velocities required for reaction. Nichols and Tarver [90, 107] have attempted to model the detonation of HMX using a statistical approach, rather than explicit modeling of microstructure. While they were able to match experimental detonation velocity results, their continuum approach makes it difficult to quantify the exact effects of microstructure on the detonation process.

Due to the fact that material heterogeneity is one of the most important sources of stochasticity in material behavior, the quantification of the statistical variations of material attributes at the microstructural level, such as grain shape and size distributions, is essential in the discussion of reliability-based design of energetic materials and in the determination of the ignition probability under given stimuli that lead to violent reactions. In spite of this,

the stochasticity of ignition thresholds, especially the influence of microstructural variations of material attributes, such as grain size distributions and defects, has not been systematically studied [106, 108]. In this study, this issue is addressed in a manner that is consistent with experimental quantification of uncertainty via the generation and use of multiple statistically similar samples of each material design setting.

1.5 Objectives of this Study and Thesis Outline

This research presented in this thesis aims at understanding the effects of microstructure morphology and constituents on sensitivity of PBX under a wide range of loading intensity $\left(P = 3-11\text{GPa}\right)$, and establishing the correlation between microstructure characteristics and the initiation of the material. Additionally, the transition from thermo-mechanical heat generation to chemical initiation and subsequent detonation is modeled and analyzed. The main objectives of this work are as follows:

(a) Analyze the ignition probability for granular HMX as a function of experimental loading conditions.

(b) Thoroughly quantify the physical mechanisms governing the desensitization of PBX by the inclusion of aluminum particulates.

(c) Develop a capability to model detonation of HMX under shock loading in both 2D and 3D.

(d) Analyze how microstructural features, including grain anisotropy and porosity affect the run-to-detonation distance (RDD) under various shock pressures.

This research consists of four main parts, divided into seven chapter. Chapter 1 provides a background on the topic of shock initiation of energetic materials research, including a literature review of important contributions and current work in the field. Chapter 2 discusses both the Lagrangian and Eulerian computational frameworks that will be employed in Chapters 3-4 and Chapters 5-6 respectively to study ignition.

In Chapter 3, fully packed HMX samples are simulated under shock loading, and a rigorous statistical methodology for quantifying the probability of ignition is developed. The response of stochastically similar sets of 2D microstructures will be simulated under impact loading with piston velocities ranging from 500 m/s to 1200 m/s and pulse durations of 30-280 μs. The local evolution of hotspots are monitored and the relative heat generation due to both plastic work and frictional work is analyzed. An ignition probability map is generated over the design space of initial loading conditions and the results of microstructural alterations are compared. This includes testing samples with large and small grain size distributions (220 μm and 70 μm respectively). Results are then compared with experimental data in the literature. This chapter allows for baseline verification of the HMX material model and constitutive properties, as well as new insights into the relative effects of plastic work vs frictional work. In addition, the probabilistic analysis developed here will serve as a useful tool for to the community at large, offering insight into the sensitivity of HEs as a function of experimental loading conditions.

Chapter 4 involves simulating PBX with the addition of aluminum particulates. Aluminum often serves as a metallic fuel in PBXs, and experiments have reported their inclusion decreases the sensitivity of PBX to ignition. The reason behind this phenomena is still not well understood. This chapter explores the thermo-mechanical effect that aluminum has on the HMX grains and Estane binder, as it relates to the overall probability of ignition. Similar to Chapter 3, ignition probability maps are generated for samples containing various volume fractions of aluminum, ranging from 0% to 18%. Additionally, the effect of aluminum particle size is examined. The generation of hotspots in samples both with and without aluminum is compared, and reasons behind any discrepancies are addressed. The aluminum used in these simulations is the aluminum alloy Al 7570.

Chapter 5 involves a probabilistic study of the shock-to-detonation behavior of pressed HMX. The current capabilities of the Lagrangian CFEM framework utilized in Chapters 3 and 4 is incapable of directly modeling the full ignition and evolution of chemistry, which is critical for further modeling of the SDT. In order to effectively study the SDT behavior, an Eulerian framework is applied to the problem using the Sandia National Laboratories solid mechanics code CTH. Using CTH, four 2D microstructure cases are examined: homogeneous (H), microstructured (M), homogeneous with voids (V), and microstructured with voids (M+V). By simulating the formation of a detonation wave in each of these cases, the run distance to detonation (RDD) may be measured as a function of shock pressure to generate a Pop plot. The effect each of these microstructure heterogeneities have on the Pop plot is rank-ordered, and a new probabilistic model is proposed to predict the likelihood of observing the SDT at any input shock pressure and RDD. The results of these simulations are then compared to experimental data in the literature.

Chapter 6 further builds on the work presented in Chapter 5 by expanding the microstructure and void simulations into 3D. 3×3×15 mm samples with realistic grain morphology and 50 μm diameter voids are considered. The discrepancies between 2D and 3D simulations are quantified, and the probabilistic analysis first introduced in Chapter 5 is further refined to illustrate a pressure dependence in relative sample SDT sensitivity.

Lastly, Chapter 7 summaries the methodology and results presented in Chapters 2-6 and provides recommendations for future work.

CHAPTER 2. COMPUTATIONAL FRAMEWORK

This chapter discusses the computational frameworks used to model ignition and detonation in Chapters 3-6 of this dissertation. Section 2.1 describes the microstructural generation procedure used to create both 2D samples (used in Chapters 3-5) and 3D samples (used in Chapter 6). Section 2.2 lays out the framework used for the Lagrangian cohesive finite-element code (CODEX), including constitutive relations, contact and frictional algorithms, and the critical hotspot ignition criterion. Section 2.3 describes the Sandia National Laboratories Eulerian-based solid mechanics code CTH, including the relevant constitutive models and chemistry models used.

2.1 Microstructure Generation

2.1.1 2D Microstructure Generation

The grains used in the 2D samples are generated by Voronoi tessellation and have random, multifaceted surfaces interlocking with each other. After inserting a numbers of "seeds" into a defined area, increasingly larger circles are drawn around each point. The radii of these circles increases until they encounter a boundary from another circle generated by another seed. Once this occurs, this connected point stops expanding while the rest of the boundary continues. After the entire perimeter of a single seed has encountered a perimeter from another nearby seed, the grain geometry stops evolving. This method of generation creates randomly faceted granular geometries which serve as good representations of a pressed microstructure. Wu et al. [109] showed that simulations of Brazilian compression of PBX using microstructures generated with this approach match

experiments reasonably well. Since frictional dissipation along crack faces under compression is an important mechanism for hotspot generation, the Voronoi tessellation method for generating microstructures is preferred to ensure well-defined intergranular interfaces. This method also allows for the generation of large numbers of microstructures with random variations in morphology and a high-degree of statistical similitude in microstructure attributes, such as grain shape and grain size distributions. A sample Voronoi output is shown in Figure 1.

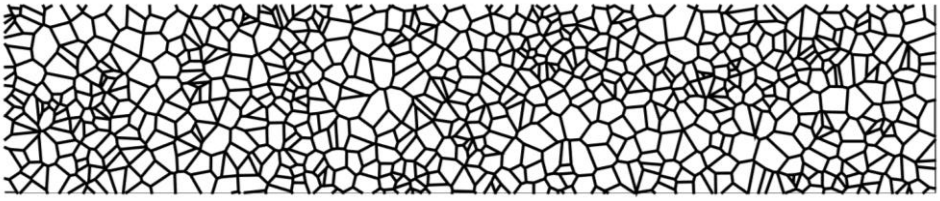

Figure 1 - Sample Voronoi tessellation output resulting in granular geometries.

2.1.1.1 CODEX Meshing Scheme

After the granular microstructure has been generated, a Matlab preprocessor is used to identify and pixelate the individual grain shapes, using the binary black and white Voronoi diagram. In the case of the CODEX framework, the sample is then meshed according to a fixed element scheme. Each grain is subdivided into a number of two-dimensional constant strain triangular elements arranged in a fixed pattern displayed in Figure 2. Between each set of elements, a cohesive element with zero area is inserted. This element allows the user to define cohesive strengths for each material-material connection and serves as the basis for handling fracture in the microstructure. More information on this cohesive finite element framework can be found in Section 2.2.3.

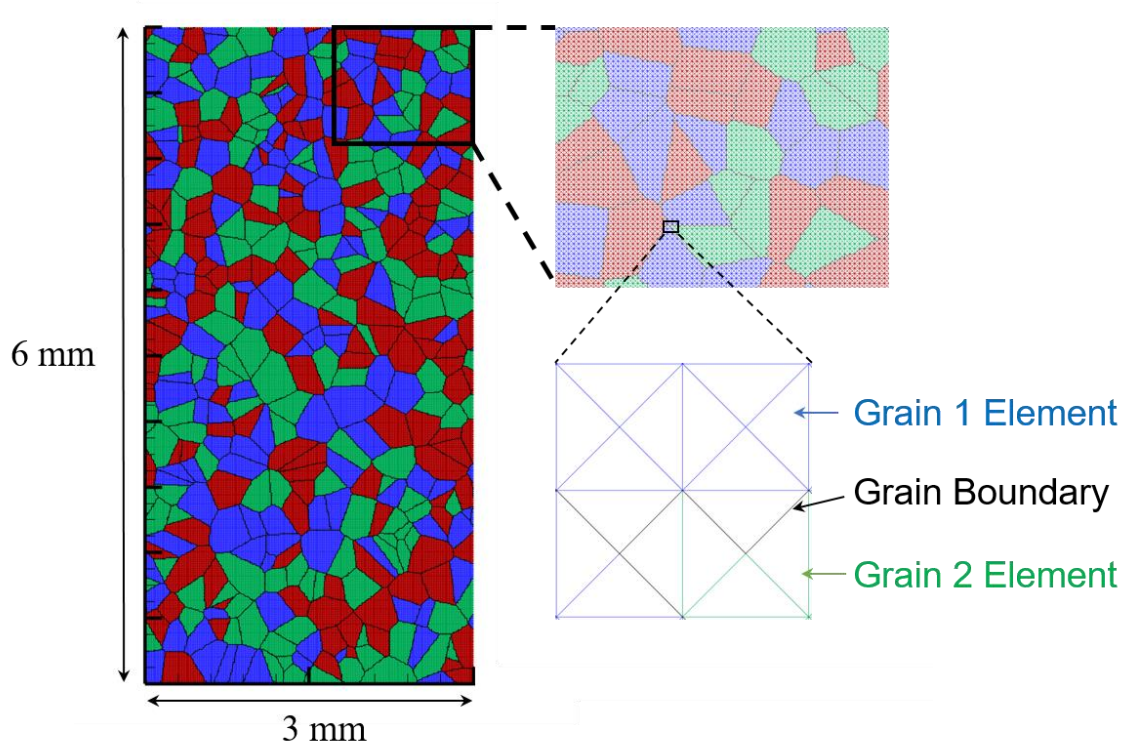

Figure 2 - Sample meshing of a randomly generated 3mm x 6mm fully dense microstructure.

2.1.1.2 Aluminized PBX 2D Microstructure Generation

While the methodology of using a Voronoi tessellation scheme alone is sufficient for generating fully-packed microstructures, when samples have multiple different constituents (as is the case with PBX), a more elaborate generation method is required. In order to generate the aluminized PBX samples discussed in Chapter 4, the procedure described here is used to generate these complicated microstructures. First, the HMX grain distribution is still generated using Voronoi tessellation. Two monomodal distributions of grains are generated: one large (200-400 μm diameter) and one small (50-200 μm diameter). Appropriately sized grains from each distribution are saved to a library, and randomly redistributed into microstructures until the appropriate volume fraction of HMX

is met to create a microstructure of desired attributes. In particular, the grains from the two monomodal distributions are combined to create microstructures with bimodal distributions of grains of different volume fractions. Following this, 50 μm diameter aluminum particles (Al 7075 alloy) are randomly inserted into the empty space not already occupied by HMX, until a total volume fraction of 81% has been achieved. Any remaining empty space is assigned to binder. This method of microstructure generation results in realistic, randomized, and stochastically similar microstructures, which allow for statistically similar testing - necessary for studying initiation probability. Figure 3 shows a sample APBX microstructure.

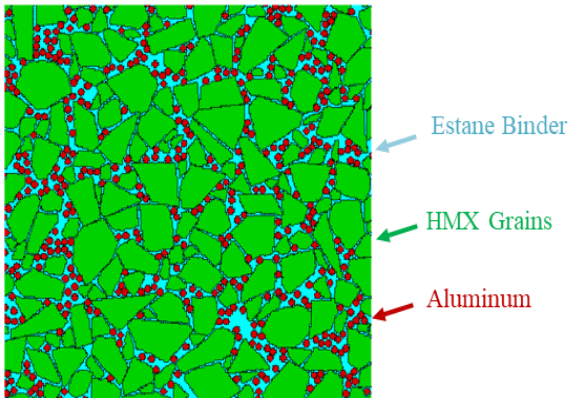

Figure 3 - Sample PBX Microstructure with HMX grains, Estane binder, and Al 7075 particulate.

2.1.2 3D Microstructure Generation

The three-dimensional microstructures used in Chapter 6 consist of four material cases: homogeneous (H), microstructured (M), homogeneous with voids (V), and microstructured with voids (M+V). The granular distribution used in the M and M+V cases is generated using a similar Voronoi tessellation procedure as 2D (discussed in Section

2.1.1), but expanded into 3D space. For the homogenous or microstructured samples with voids, the individual voids are inserted randomly until a total desired void volume fraction has been reached. No two voids overlap, ensuring a constant void size and random void distribution. A sample microstructure and void layout is shown in Figure 4. For visual clarity, a void volume fraction of 0.5% is shown in Figure 4 (b). In CTH, the microstructure geometry is input using the DIATOM subsection, which inserts all the grains first, and then replaces the void location material with air (thereby replacing the HE). More information about the DIATOM subsection is outlined in Section 2.3.1.

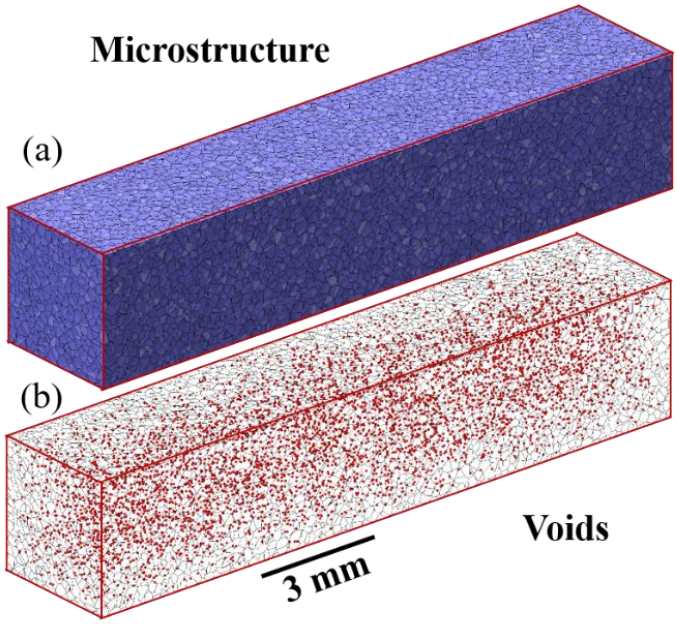

Figure 4 -(a) A sample 3D Voronoi tessellation microstructure. (b) A sample void distribution consisting of 50 μm diameter voids. The void volume fraction is 0.5%.

2.2 Lagrangian Framework

The computational analysis in Chapters 3 and 4 are performed using CODEX (Cohesive Dynamics for Explosives), a recently developed Lagrangian cohesive finite element code. The overall CFEM framework, including constitutive models, are discussed in this section.

2.2.1 CODEX Overview

The CODEX framework allows for quantification of the effects of microstructure and thermal-mechanical processes, including bulk deformation, interfacial debonding, fracture of grains, and subsequent frictional heating [39, 95, 96, 110]. The constitutive relations for the grains and aluminum are those of a hydrostatic stress-dependent elasto-viscoplastic material. Specifically, the deviatoric part of the stress tensor carried by the material follows an elasto-viscoplastic constitutive law and the hydrostatic part of the stress tensor carried by the material follows either a Birch-Murnaghan equation of state (B-M EOS) or a Mie-Grüneisen EOS, depending on the user preference. Additionally, an artificial viscosity model is used in association with the EOS to ensure numerical stability. The behavior of the binder in the PBX simulations follows the generalized Maxwell model for viscoelastic binders. A bi-linear traction-separation model is used for the cohesive elements to account for normal and tangential separations and fracture in grains. Details of the cohesive models and the parameters for transgranular separations are discussed further in Section 2.2.3. The cohesive strength at the grain-grain interfaces is set to zero. A contact detection algorithm and a subsequent contact force model are used for surfaces after fracture. The Coulomb friction damping model is used for surface elements that are in

contact. The coefficient of friction is 0.5 at the contact points between initially debonded surfaces as well as surfaces newly generated as a result of transgranular fracture. Fourier's heat conduction model is coupled with mechanical deformation and failure models to account for thermal conduction in the material. Details of the algorithm and models can be found in Ref. [95]. An outline of the constitutive and interfacial relations is given in the following section.

2.2.2 Constitutive Relations

2.2.2.1 HMX and Aluminum Deviatoric Stress-Strain Model

The deviatoric part of the constitutive behavior of both the HMX grains and Al particles is described by an elasto-viscoplastic model. The specific form of the constitutive relation used is

$$\hat{\boldsymbol{\tau}}' = \mathbf{L} : \left(\mathbf{D}' - \mathbf{D}'_p \right), \tag{1}$$

where $\mathbf{L}$ is the tensor of elastic moduli and $\hat{\boldsymbol{\tau}}'$ is the deviatoric part of the Jaumann rate of the Kirchhoff stress. For isotropic elastic response,

$$\mathbf{L} = 2\mu\tilde{\mathbf{I}} + \lambda \mathbf{I} \otimes \mathbf{I}. \tag{2}$$

Here, $\tilde{\mathbf{I}}$ is the fourth order identity tensor, λ and μ are Lamé's first and second constants. $\mathbf{D}'$ in Eq. (1) is the deviatoric part of the rate of deformation, which can be decomposed into an elastic part and a viscoplastic part as

$$\mathbf{D}' = \mathbf{D}'_e + \mathbf{D}'_p, \tag{3}$$

where $\mathbf{D}'_p$ is the viscoplastic part of $\mathbf{D}'$ in the form of

$$\mathbf{D}'_p = \frac{3\dot{\bar{\varepsilon}}}{2\bar{\sigma}}\boldsymbol{\tau}', \text{ with } \bar{\sigma}^2 = \frac{3}{2}\boldsymbol{\tau}' : \boldsymbol{\tau}'. \tag{4}$$

Here, $\bar{\sigma}$ is the Mises equivalent stress, $\boldsymbol{\tau}'$ is the deviatoric part of the Kirchoff stress, and $\dot{\bar{\varepsilon}}$ is the equivalent plastic strain rate which has the form of

$$\left.\begin{aligned} \dot{\bar{\varepsilon}} &= \frac{\dot{\bar{\varepsilon}}_1 \dot{\bar{\varepsilon}}_2}{\dot{\bar{\varepsilon}}_1 + \dot{\bar{\varepsilon}}_2}, \\ \dot{\bar{\varepsilon}}_1 &= \dot{\bar{\varepsilon}}_0 \left[\frac{\bar{\sigma}}{g(\bar{\varepsilon}, \mathrm{T})}\right]^{\mathrm{m}}, \\ \dot{\bar{\varepsilon}}_2 &= \dot{\bar{\varepsilon}}_m \exp\left[-a\, g(\bar{\varepsilon}, \mathrm{T})\right], \\ g(\bar{\varepsilon}, \mathrm{T}) &= \sigma_0 \left(1 + \frac{\bar{\varepsilon}}{\varepsilon_0}\right)^{\mathrm{N}} \left\{1 - \beta\left[\left(\frac{\mathrm{T}}{\mathrm{T}_0}\right)^{\kappa} - 1\right]\right\}, \end{aligned}\right\} \tag{5}$$

where $\bar{\varepsilon} = \int_0^t \dot{\bar{\varepsilon}} dt$ is the equivalent plastic strain, $\dot{\bar{\varepsilon}}_0$ and $\dot{\bar{\varepsilon}}_m$ are reference strain rates, *m* and *a* are rate sensitivity parameters for strain rates below $10^3\ \mathrm{s}^{-1}$ and above $5\times10^4\ \mathrm{s}^{-1}$, respectively, σ_0 is the quasi-static yield stress, ε_0 is a reference strain, *N* is the strain hardening exponent, T_0 is a reference temperature, and β and κ are thermal softening parameters. The function $g(\bar{\varepsilon}, T)$ represents the quasi-static stress-strain response at ambient temperature. The above relations consider strain hardening and strain-rate dependence of plasticity. The details of the above constitutive relations and descriptions of the parameters can be found in Ref. [111]. The material constants used in Eq. (5) for HMX are listed in Table 1 and the constants used for Al 7075 are listed in Table 2 [112].

Table 1. HMX material parameters for viscoplastic constitutive behavior

σ_0 (MPa)	ε_0	N	T_0 (K)	β
260	5.88×10^{-4}	0.0	293	0.0
$\dot{\bar{\varepsilon}}_0$ (s^{-1})	m	$\dot{\bar{\varepsilon}}_m$ (s^{-1})	a ($1/MPa$)	κ
1×10^{-4}	100.0	8.0×10^{12}	22.5	0.0

Table 2. Al 7075 material parameters for viscoplastic constitutive behavior

σ_0 (MPa)	ε_0	N	T_0 (K)	β
415	6×10^{-3}	0.07	293	0.035
$\dot{\bar{\varepsilon}}_0$ (s^{-1})	m	$\dot{\bar{\varepsilon}}_m$ (s^{-1})	a ($1/MPa$)	κ
1×10^{-4}	50.0	8.0×10^{8}	5	3.0

2.2.2.2 Equation of State (EOS)

The volumetric part of the response is described by the Birch-Murnaghan equation of state (B-M EOS). The specific form of the equation is

$$\tau_h = \frac{3}{2}K_0\left(\frac{dV}{dV_0}\right)\left\{\left(\frac{dV}{dV_0}\right)^{-\frac{7}{3}}-\left(\frac{dV}{dV_0}\right)^{-\frac{5}{3}}\right\}\left[1+\frac{3}{4}\left(K_0'-4\right)\left\{\left(\frac{dV}{dV_0}\right)^{-\frac{2}{3}}-1\right\}\right], \qquad (6)$$

where $\tau_h = \tau_{ii} = \tau_{11}+\tau_{22}+\tau_{33}$ is the hydrostatic part of the Kirchoff stress which is the product of the Jacobian and the negative of the hydrostatic pressure. K_0 is the bulk modulus,

and $K_0' = (\partial K_0/\partial P)_{P=0}$. dV/dV_0 is the volume ratio of an initial volume element (dV_0) and the current volume element (dV), which is equal to the Jacobian ($J = \det(\boldsymbol{F})$ with $\boldsymbol{F}$ being the deformation gradient). For the implementation of the B-M EOS, a time incremental form is used. The time rate of change of the Jacobian is

$$\frac{\partial}{\partial t}\left(\frac{dV}{dV_0}\right) = \left(\frac{dV}{dV_0}\right)\mathrm{tr}(\boldsymbol{D}), \tag{7}$$

and the rate of change of the hydrostatic Kirchhoff stress is a function of the Jacobian and rate of deformation, i.e.,

$$\frac{\partial \tau_h}{\partial t} = f\left(\frac{dV}{dV_0}, \mathrm{tr}(\boldsymbol{D})\right). \tag{8}$$

Previous studies [113-115] show discrepancies in the parameters of B-M EOS for HMX. Landerville et al. [115] reported that the parameters vary to a large degree among experiments due to inherent noise of experiments and inconsistencies in fitting ranges and schemes. The parameter values used for HMX are $K_0 = 16.71\ GPa$ and $K_0' = 7.79$ as reported in Ref. [115] which lie in between the values of Gump et al. [113] and Yoo et al. [114]. The B-M EOS is also used to model the aluminum particles, with values of are $K_0 = 72.7\ GPa$ and $K_0' = 5.262$, as reported in Ref. [116]. Figure 7 shows the pressure – volume relations from HMX models with and without the B-M EOS.

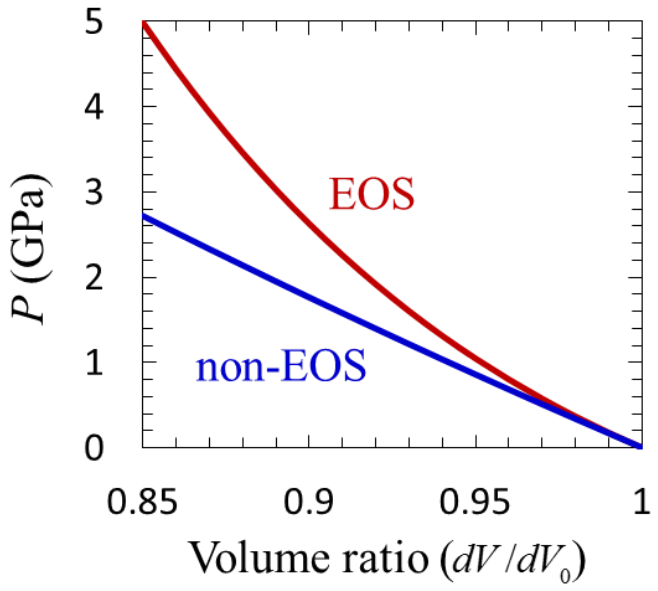

Figure 5 - Pressure - volume relations with the Birch-Murnaghan EOS and without the EOS.

2.2.2.3 Estane Viscoelastic Model

The Estane binder is modeled following the generalized Maxwell model (GMM) [117] for viscoelastic binders, shown below in Eq. (9).

$$\sigma(t) = \int_0^t 2G(\tau - \tau') \frac{\partial \varepsilon^D}{\partial \tau'} d\tau' + \int_0^t K(\tau - \tau') \frac{\partial \varepsilon^H}{\partial \tau'} d\tau', \tag{9}$$

Here, σ represents the Cauchy stress, ε^D and ε^H refer to the deviatoric and hydrostatic portions of the Eulerian strain tensor, and t and τ refer to the physical and reduced times, respectively. The shear modulus G is assumed to vary with the reduced or relaxation time τ according to a Prony series formulation [117] of the form

$$G(\tau) = G_\infty + \sum_{i=1}^{N_p} G_i e^{-\frac{\tau}{\tau_i^p}} = G_0 \left(g_\infty + \sum_{i=1}^{N_p} g_i e^{-\frac{\tau}{\tau_i^p}} \right), \tag{10}$$

where $G_0 = G_\infty + \sum_{i=1}^{N_p} G_i$ and represents the instantaneous shear modulus at reference temperature T_0, G_∞ represents the steady-state shear modulus, $g_i = G_i / G_0$ is the relative modulus of the i th term, N_p represents the number of terms in the Prony series and τ_i^p are the relaxation times. Further details regarding the binder constitutive model, including the parameters and calibration techniques used in this simulation, can be found in reference [95]

2.2.3 Cohesive Finite Element Framework

The fracture of the microstructure under high-impact loading is modeled using a cohesive finite element framework. The cohesive elements are inserted between every bulk element and are initially assigned zero area (Figure 6(a)). In this way, cohesive strength may be assigned to each bulk material, or combination thereof, without modifying the microstructure geometry itself. These cohesive elements allow for arbitrary crack initiation and propagation, while also giving CODEX the ability to explicitly model initial debonding between the grains, commonly observed in experimental samples.

The fracture follows a bilinear traction separation law described by Zhai et al [118] (Figure 6(b)). Until the displacement (δ) between two bulk elements reaches a critical distance (δ_0), the cohesive elements are considered elastic. Once this critical displacement is exceeded, the cohesive element will begin to lose energy, and a resulting reduction in element stiffness occurs. If the element passes a second critical displacement (δ_c), the total energy lost equals the critical energy release rate and the interface between its two connecting bulk elements is considered fractured. Once this point is reached, the strength parameters of the cohesive element connecting the two bulk elements are set to zero. The

cohesive parameter values for each pair of possible bulk element connections are listed in Table 3. Further details on this cohesive model can be found in reference [95].

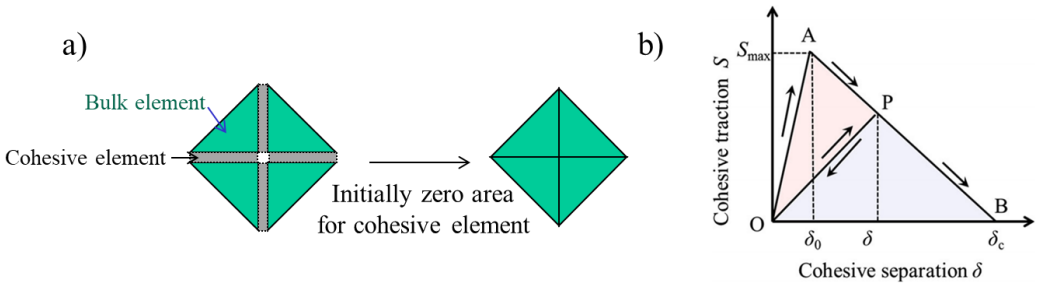

Figure 6 - (a) Illustration of the connectivity between cohesive elements and bulk elements. (b) Bilinear traction separation law.

Table 3. Cohesive Parameters for each bulk element combination

Element Type	δ_c (μm)	δ_0(μm)	S_{max} (MPa)
Estane-Estane	10	0.1	557
HMX-HMX	5.0	0.005	101
Al-Al	15.4	0.0154	345
HMX-Al	4.66	0.00466	70
Al-Estane	4.71	0.00471	70
HMX-Estane	4.62	0.00924	35

2.2.4 Contact, repulsion, and friction algorithm

Detection of contact is a computationally expensive procedure, as described by Burago [119]. This CFEM framework utilizes a Lagrangian penalty-based repulsion algorithm. If a cohesive element is failed, the adjacent bulk elements are added to a list. The contact detection is performed for bulk elements in this list at each computational time step. The calculation time of this algorithm is proportional to second power of the number

of failed elements. To reduce the computational time, a coarse grid is placed on a fine mesh, and the contact search algorithm only considers elements that lie within the same cell of the grid. Initially, each cell expands its size to have overlaps with neighbor cells, so that searching process does not miss the contact of elements at the grid boundary. A penalty force is applied to each node of failed surfaces to strongly discourage interpenetration and maintain proper contact of the surfaces. The direction of the repulsion force is normal to the contact surface, and the magnitude is determined based on relative acceleration, velocity and penetration depth of two elements that are in contact. Detailed descriptions of the multi-step contact algorithm and the penalty forces are given in Ref. [120]. Frictional heating due to sliding along surfaces in contact is assessed using the Coulomb friction law. The stick-slip state is determined by the normal force between contact surface pairs.

2.2.5 Ignition Criterion

In order to determine whether a sample reaches ignition, a simplified critical hotspot theory is employed. The focus of this Lagrangian framework is not to explicitly model the entire onset of chemistry, but rather identify the initiation of hotspots. This hotspot criticality condition is based on the assumption that once the rate of heat generation due to chemical decomposition overtakes the rate at which heat can be conducted away to the surrounding, cooler material, then the hotspot has become critical. As the temperature of the hotspot rises, the rate of heat generation due to chemistry also increases. This criticality condition is listed below.

$$\dot{Q}_{chem} > \dot{Q}_{loss} \tag{11}$$

To determine whether or not a hotspot has gone critical in CODEX, a temperature analysis is performed. The temperature field of a sample from the CFEM calculation is scanned for localized temperature rises above a given temperature threshold (T_{thres}). Areas of a temperature field with temperatures above the threshold are analyzed for hotspots. Successively varying T_{thres} values allow the characteristics of a temperature field to be fully analyzed.

After all hotspots in a sample are quantified in terms of size and temperature, a recently developed criterion for ignition [96] is used to determine the onset of irreversible chemical decomposition of the HMX phase in the samples. This criterion provides a relationship between the size and the temperature states of critical hotspots. Specifically,

$$d(T) \geq d_{\mathrm{c}}(T), \tag{12}$$

where d is the diameter of a hotspot resulting from a loading event whose interior temperatures are at or above temperature T. d_c is the minimal diameter of a hotspot required for thermal runaway at temperature T. The quantitative information regarding the right-hand side of Eq. (12) is taken from the work of Tarver et al. [28] who performed chemical kinetics calculations to analyze the criticality issue for HMX and TATB explosives. The calculations consider multistep reaction mechanisms and the pressure and temperature dependence of reactants and products. More details about the ignition criterion can be found in Ref. [96].

The left-hand side of Eq. (12) is obtained by analyzing the temperature fields in the microstructures from CFEM calculations. To account for the variations of temperature within a hotspot (note that temperatures at different spatial locations within a hotspot are different and the temperature threshold is the lowest temperature at the periphery), the hotspot threshold of Tarver et al. is treated as a band of ± 10% about the mean value, as in Ref. [96]. A hotspot is considered to be critical when it crosses the lower threshold limit (90% of the average value). The initiation of the material is regarded as being reached if the critical hotspot density is equal to or greater than $0.22\,mm^{-2}$ which corresponds to two critical hotspots in a 3 mm square domain. The specific choice of the current critical hotspot density (0.22 mm^{-2}) is based on the observation of Barua et al. [96] who observed a negligible difference on the criticality results by changing the critical hotspot density between 0.11 mm^{-2} (single hotspot in the whole sample) to 0.44 mm^{-2} (4 hotspots in the whole sample). This consistency is primarily because many hotspots develop simultaneously and reach the threshold within very short time intervals from each other. It has been contemplated that interactions among subcritical hotspots in close proximity of each other might lead to one critical hotspot or sample criticality. If a critical hotspot is to emerge from the interactions of multiple hotspot, it would be detected by the approach used here and accounted for by the ignition criterion.

2.3 Eulerian Framework

2.3.1 CTH Overview

While the Lagrangian framework of CODEX is a useful tool for predicting the ignition threshold due to its explicit ability to track frictional heat generation at low impact

velocities, a new framework is needed to explicitly model the shock-to-detonation transition (SDT). In Chapters 5 and 6, the shock physics hydrocode from Sandia National Laboratories, CTH, is used to model the detonation behavior of pressed HMX. This section will only discuss a few of the key elements and constitutive relations chosen for these simulations. For further information regarding CTH, see References [86, 87, 121].

In CTH, a Lagrangian step with zero mass flux into or out of the element is used to initially track the deformation followed by a subsequent Eulerian remap step to return the mesh to its original position. During the Lagrangian step, mass, momentum, and energy are all conserved. Once the material has deformed as far as it can (as constrained by the time step), a second order accurate advection scheme is implemented to calculate the new material state properties in each of the reformed elements. During the remap step, CTH is unable to conserve both kinetic energy and momentum. Due to this, momentum is chosen to be conserved, while the internal energy is convected. Any kinetic energy discrepancy is discarded, meaning that the total energy in the system is not technically conserved. This may lead to potentially erroneous temperature measurements in areas with particularly strong deformation.

CTH is able to run in parallel on multiple processors, making large scale simulations feasible. The primary inputs for CTH include defining the material geometry, an EOS model, a strength model for each material, and a chemistry model if the material is reactive. The specifics of these models used for the HMX SDT modeling in this thesis are provided in Sections 2.3.2-2.3.4. Further details on CTH can be found in references [86, 87, 121, 122]

2.3.2 Material Geometry Input

Generated 2D and 3D microstructures (as described in Section 2.1) are defined in CTH using the DIATOM subroutine. Geometries defined as the microstructure are inserted in the same order they are listed in the input deck. If two geometries overlap (e.g. two grains), the DIATOM subsection will insert whichever one was listed first, and then attempt to insert the second one. Any volume of the second geometry which overlaps with the first is ignored. In order to generate the voids used in Chapters 5 and 6, the DIATOM subsection features a "replace" command, which allows one to redefine the material in a previously defined material volume. Using these insertion and replacement commands, in addition to the STL files defining each grain in the Voronoi generated microstructure, complicated and realistic looking microstructures may be accurately modelled in CTH. Figure 7 depicts a cartoon illustrating how CTH generates different geometries depending on their order in the CTH input deck.

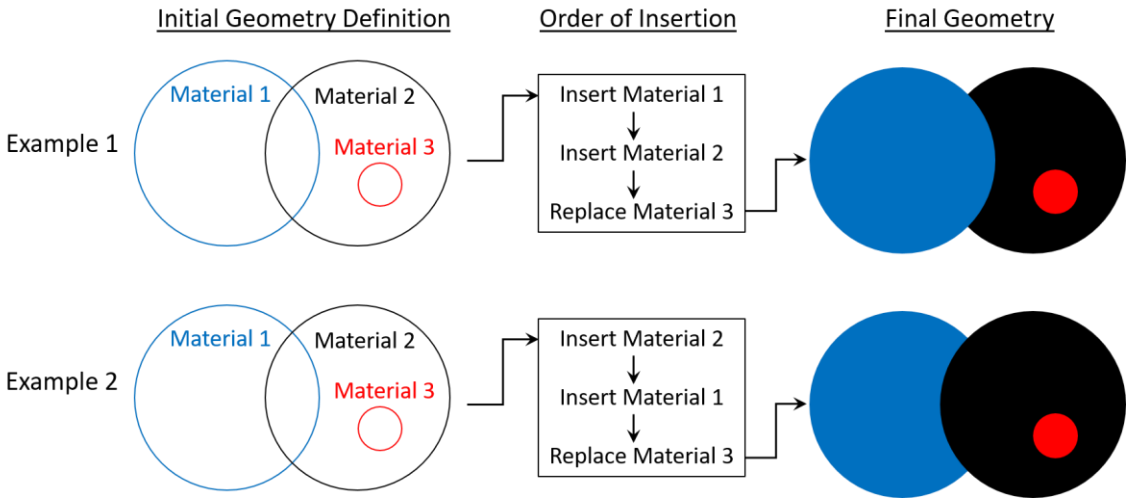

Figure 7 – Cartoon illustrating the importance of DIATOM ordering when defining geometries in CTH.

2.3.3 Constitutive Relations

A simplified Steinberg-Guinan-Lund strain-dependent flow stress model (SGL) is used to account for the viscoplastic behavior of HMX. This strain-rate dependent model is well-suited for high strain-rate deformation and accounts for the effects of thermal softening. The material yield stress is calculated via

$$\sigma_Y\left(\dot{\varepsilon}_P, T\right) = \left[\sigma_A + \sigma_T\left(\dot{\varepsilon}_P, T\right)\right], \text{ with} \tag{13}$$

$$\dot{\varepsilon}_P = \left\{\frac{1}{C_1}\exp\left[\frac{2U_K}{T}\left(1-\frac{\sigma_T}{\sigma_P}\right)^2\right] + \frac{C_2}{\sigma_T}\right\}^{-1}. \tag{14}$$

In the above relations, σ_A is the athermal component of the flow stress, σ_T is the thermally activated component of the flow stress, and C_1, C_2, U_K, and σ_P are material parameters. The model has been calibrated to match the elasto-viscoplastic model used for HMX as

described in Section 2.2.2.1, which in turn was based on available experimental data. The values of the material parameters in the model are listed below in Table 4.

Table 4. HMX material parameters for the SGL flow stress model

C_1	C_2	U_K	σ_P
3.79×10^{11} s^{-1}	1.45 Pa·s	3000 K	650 MPa

The bulk response to hydrostatic pressure is modeled using the first order Mie–Grüneisen EOS

$$p = \frac{\rho_0 C_0^2 \left(1-\frac{\rho_0}{\rho}\right)\left[1-\frac{\Gamma_0}{2}\left(1-\frac{\rho_0}{\rho}\right)\right]}{\left[1-s\left(1-\frac{\rho_0}{\rho}\right)\right]^2} + \Gamma_0 E, \tag{15}$$

where p is the pressure, ρ_0 is the initial density of HMX, ρ is the current density of HMX, Γ_0 is the Grüneisen parameter, C_0 is the bulk sound speed, and s is the slope of the Hugoniot. E is the internal energy which is found by integrating the specific heat with respect to temperature at constant volume, i.e.,

$$E = \frac{1}{V_0}\int_0^T c_v dT. \tag{16}$$

Table 5. HMX material parameters for the Mie–Grüneisen EOS model

ρ_0	C_0	s	Γ_0
1.33 g/cm^3 or 1.90 g/cm^3 or 2.47 g/cm^3	2900 m/s	2.0	1.0

2.3.4 Chemistry Model

The process of chemical reaction initiation and progression follows the history variable reactive burn model (HVRB) in the form of

$$\lambda = 1 - \left(1 - \frac{\phi^M}{X}\right)^X, \text{ where} \tag{17}$$

$$\phi = \tau_0^{-1} \int_0^t \left[\frac{(p - p_i)}{p_R}\right]^Z dt. \tag{18}$$

In the above relations, λ is the extent of reaction, τ_0 is a scaling constant, p is the current pressure, p_i is the threshold pressure for reaction, and p_R, X, M, and Z are reaction rate parameters. Reactive burn models have been widely used to simulate the ignition and detonation of HEMs [14, 83, 84]. These empirical models are often calibrated to Pop plot data. As a result, the localized extent of reaction behind the shock front may not be perfectly resolved (which is a known limitation for the HVRB model). However, with available data and models, this is a reasonable trade-off in order to reach the macroscale from the mesoscale, since the focus here is on analyzing macroscale material

behavior. The HVRB model provides a straightforward method of accounting for chemical reaction at larger size scales which would otherwise prove more computationally intensive if an Arrhenius-based chemical reaction rate model is used. Still, it is worthwhile to note that if and when a more useful chemistry model is made available, it can be easily used in the current framework – there is no fundamental impediment to the use of other, especially more mechanisms-based, reaction models. The calibration parameters shown in Table 6 have been fit to the average state data of HMX and are found in the CTH material properties library. Once the chemical extent of reaction for the solid HMX reaches 100%, the material behaviors following an internal equation of state reference table, also known as a SEASAME table.

Table 6. HMX material parameters for the HVRB chemistry model

τ_0	p_i	p_R	X	M	Z
1×10^{-6} s	500 MPa	6 GPa	1	1.5	2.36

CHAPTER 3. COMPUTATIONAL PREDICTION OF PROBABILISTIC IGNITION THRESHOLD OF PRESSED GRANULAR HMX UNDER SHOCK LOADING

This chapter is based on the work published in Ref. [19] in collaboration with Seokpum Kim.

3.1 Introduction

The subject of ignition (go or no-go) occupies a central place in consideration of explosives' safety and performance. As a result, there exists a large body of literature covering a wide range of scenarios, from loading and environment, spatial and time scales, to material composition and microstructure. In particular, the establishment of precise conditions for the ignition of real energetic materials is especially important. The threshold conditions are commonly expressed by simple analytic functions. Solov'ev [123] reviewed several such thresholds, each of which focuses on a different initiation mechanism. One of the newer and most commonly used thresholds is the James relation [54]. This threshold is chosen for use in this Chapter not only because it accurately describes experimental data, but also because it considers two macroscopic state variables, one is the rate at which energy is imparted to a sample (energy flux) and the other is the total energy imparted to a sample (energy fluence). So far, the establishment of ignition thresholds has been exclusively an experimental endeavor. In this Chapter, a methodology is developed for predicting the James type ignition thresholds through microstructural level simulations of real explosive systems. The method is an extension of a novel computational capability

based on the Lagrangian cohesive finite element method (CFEM) and represents a pathway toward building predictive tools for evaluating and comparing solid explosives at the grain scale and for establishing relations between macroscopic safety/performance and microscopic structures of the materials. The method and the relations it yields are such that they can be used in the design of new explosives via heuristic improvement of performance through microstructural, constituent and compositional engineering. In the pursuit of this objective, emphasis is placed on (1) quantification of conditions of ignition under well-understood planar shock wave stimuli typically applied in experiments, (2) capture of essential material attributes and physical processes that control ignition, (3) recognition of the probabilistic nature of the ignition phenomenon, and (4) comparison with independent experimental measurements.

This chapter consists of three parts. The first part describes the computational framework used to study shock ignition and includes discussion on microstructure representation, loading configuration, and constitutive relations. The second part discusses simulation results with focus on shock ignition thresholds in terms of the modified James function and a probabilistic quantification of the thresholds. Normalized hotspot temperature as a measure for the ignition risk of individual hotspots is then introduced [referred to as the hotspot ignition risk determinant (HIRD) or R]. The third part focuses on the major findings, which include predicted James type ignition thresholds for pressed HMX powders, the effect of particle size on the James ignition thresholds, comparison with experimental measurements, and the probability distribution of the thresholds as a function of the James number (J) as introduced by Gresshoff and Hrousis [106].

3.2 Framework of Analysis

3.2.1 Material

The material considered here is pressed granular HMX (Octahydro-1,3,5,7-tetranitro-1,3,5,7-tetrazocine) with microstructures consisting of HMX grains without binder. In the experiments, materials with different grain sizes are referred to as different "classes". Of particular interest are Class 3, which has an average grain size of d_{avg} = 358 μm, and Class 5, which has an average grain size of d_{avg} = 6.7 μm initially. These HMX grains are then pressed, causing the grain sizes to become somewhat smaller than their original sizes (see Figure 4 in Ref. [124]) due to fracture. Both classes have a density that is 94% the theoretical maximum density (TMD). Figure 8 shows scanning electron microscope (SEM) images of the microstructures of these two classes of HMX. A small number of abnormally large grains (referred to as "boulders") are present in the Class 5 material. Samples prepared for shocked experiments are cylindrical pellets with a diameter of 0.5 inches and a height of 0.5 inches.

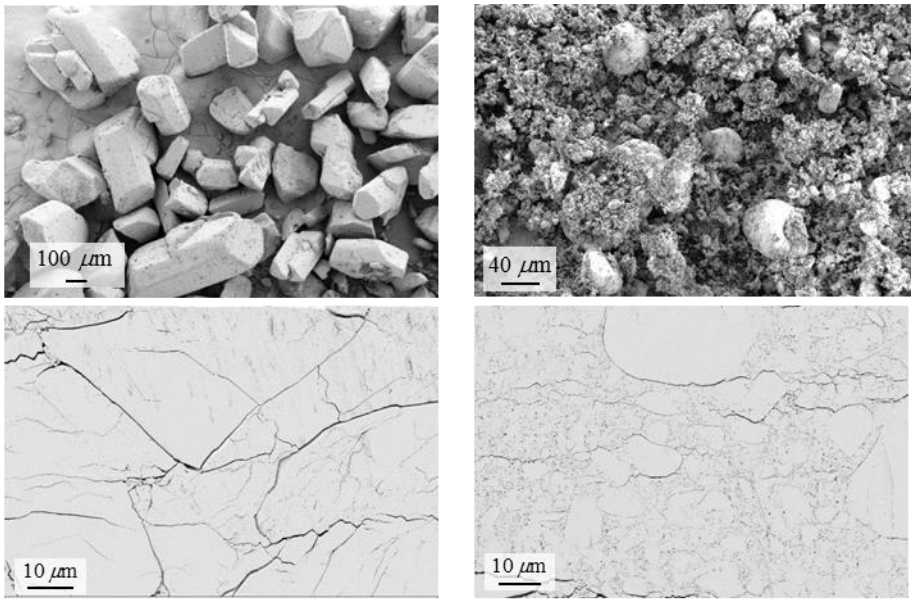

Figure 8 – SEM images of materials used in experiments, (a) Class 3 HMX and (b) Class 5 HMX. Images in the upper row show HMX crystals and images in the lower row show the microstructures made out of the corresponding HMX Classes after pressing. The images are provided courtesy of R. R. Wixom at Sandia National Laboratories.

The materials and the experimental procedure of Welle et al. [13] serve as a basis and starting point for the computational analysis. In the experiments, multiple samples for each material class and load condition are tested to quantify the ignition threshold distribution. Similarly, for systematic computational quantification of the probabilistic ignition behavior, statistically similar sample sets with multiple (5) samples are computationally generated and tested under identical loading conditions. The computationally generated microstructures mimic the attributes of the experimental microstructures. The generation uses 2D Voronoi tessellation [110]. The computationally generated samples are designed to achieve two objectives: (1) maintain statistical consistency among samples for each material setting (e.g., consistency in grain size

distributions, grain volume fraction, and grain shapes for a given average grain size) and (2) focus on trends in key microstructure attribute (grain size) among the different classes of materials. To this end, each sample set follows a mono-modal grain size distribution with a specific average grain size that lies between the average grain sizes of Class 3 and Class 5. This approach allows primary trends in material behavior-microstructure relations to be identified and quantified while a significant degree of similitude is maintained between the experiments and simulations for relative comparison. Further information regarding the generation of these microstructures in found in Section 2.1.1.

The differences between the experimental samples and computationally generated samples are as follows. First, the large "boulders" in the Class 5 experimental samples are not considered in the computationally generated microstructures, as their percentage is small (<10%) and accounting for such large grains would require much larger representative volumes which are computationally prohibitive for the large number of statistical calculations pursued here. The second difference between the experimental samples and computationally generated samples is that the experimental samples have a density that is 94% of the TMD and, more importantly, the voids are too small ([125]) to be resolved explicitly via finite element meshing at the overall size scale of samples analyzed. Therefore, a phenomenological approach for accounting for the effects of voids is taken in the simulations. Specifically, the effects of the voids are considered through variations in the bulk properties of the grains based on the fact that small-scale voids weaken the stiffness and strength of materials. This treatment applies to heterogeneous characteristics including micro and nano scale voids, microcracks, variations in material properties of the HMX grains, and directionality of constituent behavior due to crystalline

anisotropy. Here, these heterogeneities are phenomenologically accounted for in a unified manner via random variations in the elastic modulus of the grains. Researchers have analyzed the variations of the elastic moduli due to various factors including defects through experiments and computation. Yang et al. [126] performed a MD simulation of a copper plate with a void and found that the elastic modulus decreases as the volume fraction of the void increases. Hudson et al. [127, 128] quantified the voids in RDX crystals and assigned a defect score to each grain. By using nano-indentation, they measured the elastic modulus and found grains with more defects (high defect scores) have a lower elastic modulus. These findings provide justification and serve as a guide for the use of varying elastic modulus values of HMX to phenomenologically account for heterogeneities in the microstructures analyzed here. Three levels of elastic modulus (E = 30.3, 20.0, and 12.9 GPa) are randomly assigned to the HMX grains. These levels are determined based on a study of the anisotropy of the elastic behavior of HMX and data in the literature on how voids affect elastic moduli. Specifically, the maximum and minimum values of the Young's modulus of HMX are determined from the stiffness tensor provided by Sewell at al. [129]. The intermediate value is taken to be the Voigt Ruess Hill (VRH) average of the stiffness tensor. A similar case has been studied by Dimas et al. [130] who randomly distribute the Young's modulus in the microstructure. The random variations in their study follow a lognormal distribution, with the mean value representing the effective modulus of the simplified homogeneous material. Similarly, in our study, the effective modulus corresponds to the VRH average (E = 20.0 GPa) of the stiffness tensor. The grains with the high level of Young's modulus (E = 30.3 GPa) are assumed to lie in orientations that have the highest stiffness. The high level of bulk modulus of these grains represents ideal

crystals without voids or defects. The grains with the low level of Young's modulus (E = 12.9 GPa) are assumed to lie in an orientation that have a lower stiffness. The low level of bulk modulus of these grains represents the crystals with significant amounts of voids or defects. A parametric study is carried out with further variations from these values. It is found that the changes do not have a significant influence on the ignition behavior of the materials. Part of the reason lies in the fact that heating is primarily an outcome of fracture and inelasticity (see Figure 28 in Ref.[120]). Isotropic constitutive relations are implemented in our framework. Anisotropy in the Young's modulus provides a guideline for choosing maximum and minimum values for the isotropic model. Specifically, the maximum and minimum bulk modulus and shear modulus values used differ by the same ratio as the maximum and minimum values of Young's modulus described above. Although the computationally generated microstructures are not "exact" representations or reproductions of the experimental samples, major attributes are captured, allowing trends in the effects of grain size on ignition behavior to be delineated. It is worth pointing out that what is pursued here is not meant to be an "all-inclusive" effort that explicitly accounts for all possible effects of microstructure on the ignition of the materials. Rather, it is meant to be a novel effort aimed at the computational prediction of ignition thresholds, explicitly accounting for major dissipation mechanisms other than heating due to voids. The effect of voids on ignition and detonation behavior is examined in Chapters 5 and 6 in 2D and 3D space respectively.

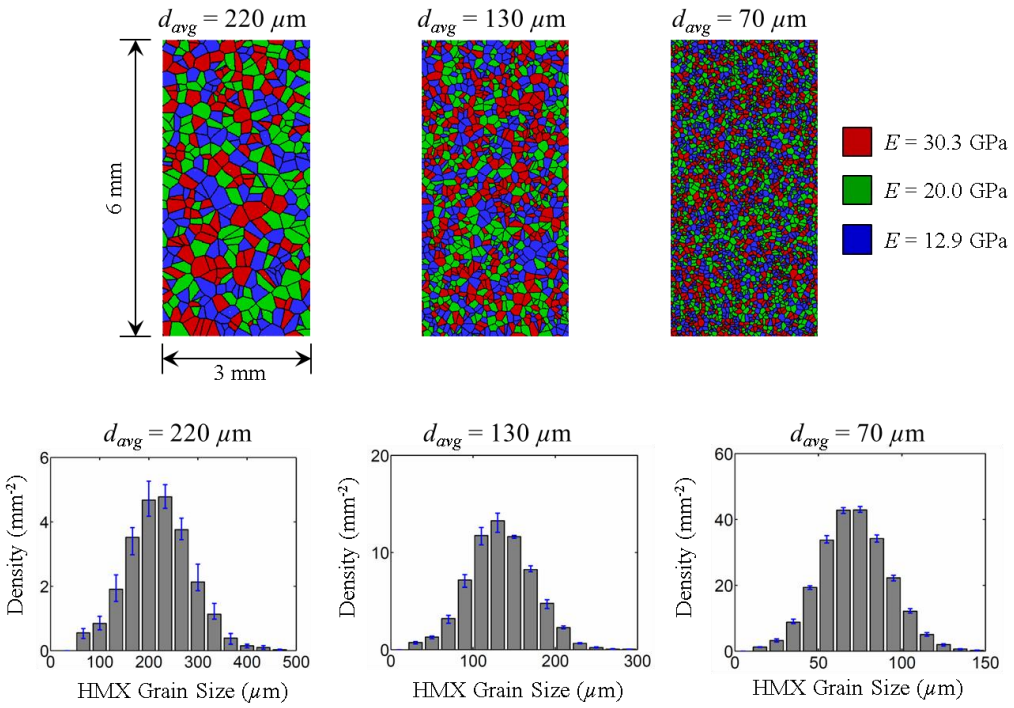

Figure 9 - Computationally generated microstructures and the size distributions of HMX grains in the microstructures for d_{avg} = 70, 130, and 220 µm. Each microstructure image shown represents one sample in a set of five statistically similar samples which are random instantiations of the same microstructure conditions.

The average grain size of the experimental samples for Class 3 (d_{avg} = 358 μm) is around 50 times larger than the average grain size of Class 5 (d_{avg} = 6.7 μm). Since larger grains require a proportionally larger sample size or representative volume element (RVE), to resolve the large Class 3 grain size with the same fine mesh resolution as required for the small Class 5 grain size, computational models with an extremely large number of degrees of freedom (DoF) would be needed. To keep the overall DoF at a reasonable level for the large number of statistical runs, a parametric approach is taken, focusing on the trend in the size effect rather than the absolute size itself. Specifically, we consider the average grain sizes range of d_{avg} = 70 – 220 μm, which lie between the sizes of the Class 3

and Class 5 HMX. The resulting microstructural domain of each sample is $3 \times 6\,\mathrm{mm}$. Although the computationally generated samples have much smaller domain size than the size of experimental samples, the size of 3 mm of the computational samples is at least one order of magnitude larger than the length scale of the largest average grain size (d_{avg} = 220 μm) considered, giving sufficient volumetric representation of the microstructures. Liu [131] reported the minimum size of the RVE to be 1.5 mm for a sample with an average grain size of 125 μm. His finding supports the choice of sample size here for the range of grain sizes considered. Indeed, we have shown that the stress-strain behavior predicted with the current choice of domain size (3 mm) matches the experimental measurements, as seen in Figure 10 of Ref. [95]. In addition, as it will be clarified in Section 3.3.1., the height of 6 mm is long enough so that the stress attenuates significantly when it reaches the bottom of the domain, such that the ignition is determined by material events near the impact face and materials and boundaries far away from the impact face have no influence on the ignition outcome under the conditions considered here.

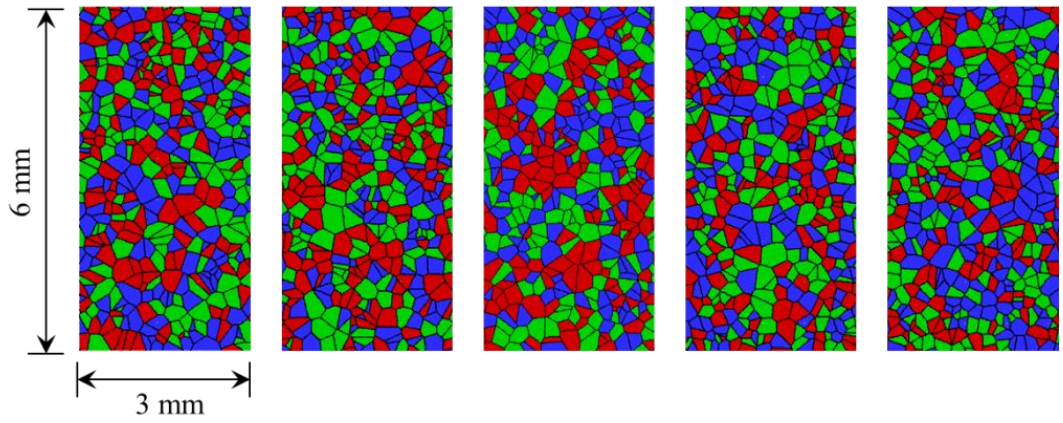

Figure 10 - Multiple samples of computationally generated, statistically similar microstructures with the average grain size of d_{avg} = 220 µm.

Three sets of microstructures are generated with average grain sizes of d_{avg} = 70, 130, and 220 μm, respectively. Each set consists of five samples which have statistically the same attributes in terms of grain size distribution and specific grain boundary surface area. In total, 15 samples (3 sizes x 5 samples for each size) are generated and used. The microstructure sets and corresponding grain size distributions are shown in Figure 9. To illustrate the random variations in microstructure morphology within a particular microstructure set, Figure 10 shows the five samples having the same average grain size of d_{avg} = 220 μm.

The HMX grains of the samples in the experiments are simply pressed mechanically, leading to very weak or no bonding along the grain boundaries. In the simulations, the bonding strength along the grain boundaries is assumed to be zero.

3.2.2 Loading Configuration

The shock experiments carried out use an Electric Gun to launch thin flyers, generating a planar shockwave in the HMX samples [13]. Each sample is placed in a steel cup that only allows one face to be exposed to receive the flyer impact. The samples are subjected to shock loading with various combinations of pulse intensities and durations (as determined by the velocity and thickness of the flyer, respectively). Four different flyer thicknesses ranging from 23 μm to 183 μm are used. For each flyer thickness (corresponding to a specific pulse duration), different shots with different flyer velocities are conducted on the same material. The ignition response of a sample is recorded as "go" if the sample explodes and as "no go" if the sample does not explode. The results of the experiments are plotted in Figure 11(a-b).

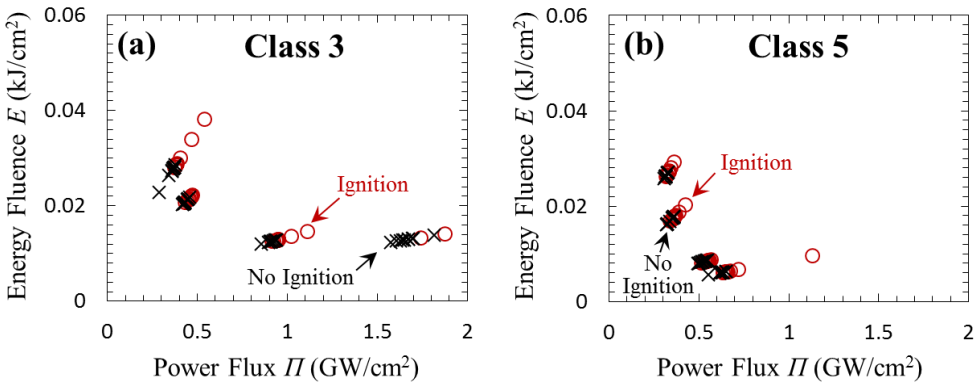

Figure 11 - Ignition threshold determination from experiments using multiple samples of a material with different flyer velocities at each flyer thickness (or pulse duration), (a) Class 3, and (b) Class 5.

The simulations emulate the experiments directly. The computationally generated specimens are initially stress-free and at rest. Impact loading is effected by applying a prescribed boundary velocity at the impact face (top boundary of the sample), as shown in

Figure 12(a). The left and right boundaries are constrained such that lateral expansion does not occur. This confinement mimics the effect of the steel cup holding the experimental sample. This is a 2D model and the conditions of plane-strain prevail. This configuration approximates the shock pulse loading of a sample driven by a thin flyer under conditions of approximate macroscopic uniaxial strain. The pulse intensity and duration are chosen to correspond to the loading characteristics in the experiments. The experiment conditions and relevant parameters are given in Table 7.

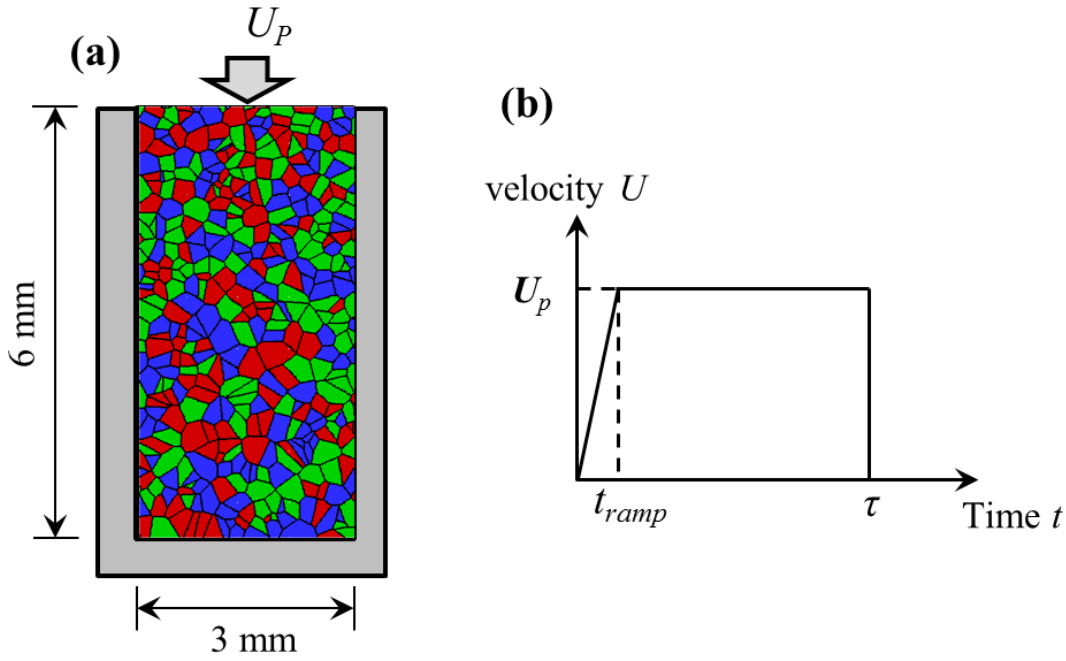

Figure 12 - (a) Configuration of computational model of shock experiments, loading, and boundary conditions considered, and (b) load history imposed on the top boundary of the domain.

Table 7. Material properties of flyer and specimen and conditions of experiments

	Parameters	Flyer 1	Flyer 2	Specimen
Material properties		Parylene-C [132]	Kapton [132]	HMX
	Longitudinal wave Speed c (m/s)	2,228	2,741	3,750
	Density ρ (kg/m^3)	1,286	1.414	1,910
Experimental condition	Flyer velocity v_{fly}	2 – 4.2 km/s	1.5 – 2 km/s	Stationary
	Thickness H	23 – 37 μm	111 – 183 μm	12.7 mm

The imposed velocity at the top boundary (U_p) of the sample is determined by the ratio between the longitudinal wave impedances (ρc) of the flyer and the HMX sample as

$$U_p = \frac{\rho_{fly} c_{fly}}{\rho_{fly} c_{fly} + \rho_{HMX} c_{HMX}} V_{fly}, \tag{19}$$

where ρ_{fly} is density of the flyer, c_{fly} is wave speed in the flyer, ρ_{HMX} is density of HMX, c_{HMX} is wave speed of HMX, and V_{fly} is the launching velocity of the flyer. The range of loading analyzed in the experiment corresponds to the imposed particle velocity range of $U_P = 500 - 1200\,\text{m/s}$ (approximate flyer velocity range of 1.5 - 4 km/s) and the range of pulse duration of $\tau = 20 - 130\,\text{ns}$. The specific particle velocity levels considered in the computational analysis are $U_P = 500$, 700, 900, and 1200 m/s and the range of pulse duration analyzed is $\tau = 10 - 280\,\text{ns}$. The pulse duration increment between successive durations depends on load intensity and varies between $\Delta\tau = 1 - 12\,\text{ns}$, as listed in Table 8. The pulse duration is the time it takes the longitudinal wave to traverse a round trip in the

flyer. For each velocity and sample, 10 different pulse durations are considered, yielding 600 microstructure-loading combinations (4 velocities × 10 pulse durations × 3 grain sizes × 5 microstructures). The profile of the imposed shock pulse at the boundary is shown in Figure 12(b). The velocity rapidly increases from zero to the particle velocity of U_P during the ramp time of t_{ramp} = 10 ns. This velocity is kept constant until the pulse time τ is reached. After the pulse time ($t \geq \tau$), the top boundary is released and no external loading is applied, while the boundaries on the left, right, and the bottom remain constrained in their normal directions. The computational prediction of the "go" and "no go" threshold in this chapter follows the same procedure as used in experiments of Figure 11(a-b). As an example of the results, the "go" and "no go" thresholds from each microstructure of grain sizes of 70 – 220 μm are plotted in Figure 13(a-c). The symbols represent either "go" or "no-go" for each combination of flyer velocity and pulse duration. The data points are along vertical lines in Figure 13 because the simulations are performed for different pulse durations at each flyer velocity, which determines the energy flux. On the other hand, experiments are performed at different flyer velocities for each flyer thickness which determines pulse duration, resulting in the data points to line up along diagonal lines in the energy fluence-power flux space. This slight difference in how the computational and experimental data points populate the domain of analysis does not affect comparison of the two data sets in any way. A total of five microstructures for each grain size are used for the computational analysis, and Figure 13(a-c) show the results from only one microstructure of each grain size.

Table 8. Load conditions and load increments analyzed

U_p (m/s)	500	700	900	1200
$P \cdot U_p$ (GW/cm^2)	0.173	0.366	0.65	1.273
Range of E (kJ/cm^2)	0.0169 - 0.0507	0.0132 - 0.0416	0.0094 - 0.042	0.0045 - 0.0429
Range of pulse duration τ (ns)	100 - 280	40 - 112	20 - 65	10 - 34
minimum τ interval (ns)	12	6	3	1

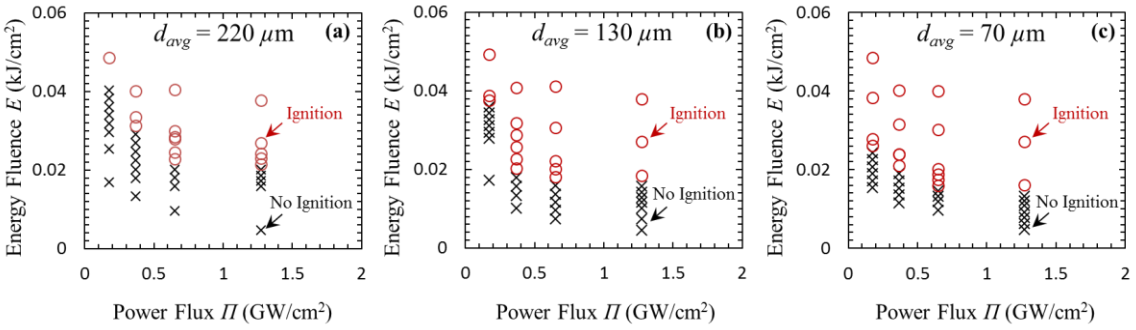

Figure 13 - Ignition threshold determination from computation using one microstructure of each grain size, (a) d_{avg} = 220 µm, (b) d_{avg} = 130 µm, and (c) d_{avg} = 70 µm. Multiple pulse durations are used for each load intensity.

3.2.3 Constitutive Relations

The simulations are performed using a recently developed Lagrangian cohesive finite element framework [39, 95, 96, 110]. This framework allows quantification of the effects of microstructure and thermal-mechanical processes, including bulk deformation, interfacial debonding, fracture of grains, and subsequent frictional heating. The constitutive relations for the grains are those of a hydrostatic stress-dependent elasto-viscoplastic material. Specifically, the deviatoric part of the stress tensor carried by the

material follows an elasto-viscoplastic constitutive law and the hydrostatic part of the stress tensor carried by the material follows the Birch-Murnaghan equation of state (B-M EOS). The term “pressure” and the variable “*P*” refer to the hydrostatic part of the stress in the following discussion. Additionally, an artificial viscosity model for numerical stability is used in association with the EOS. A bi-linear traction-separation model is used for the cohesive elements to account for normal and tangential separations and fracture in grains. Details of the cohesive models and the parameters for transgranular separations are given in Ref. [95]. The cohesive strength at the grain-grain interfaces is set to zero. A contact detection algorithm and a subsequent contact force model are used for surfaces after fracture. The Coulomb friction damping model is used for surface elements that are in contact. The coefficient of friction is 0.5 at the contact points between initially debonded surfaces as well as surfaces newly generated as a result of transgranular fracture. Although the coefficient of sliding friction is usually lower than the coefficient of static friction, the same value of 0.5 is used for both, for the lack of measured data. The value chosen is based on the work of Green et al. [133] who reported the range of 0.3-0.7 for PBX 9404. Dickson et al. [134] reported that the frictional coefficient for PBX 9501 is between 0.4 and 0.5. Chidester et al. [33] used a value of 0.5 for LX-10 based on the experiments of Green et al. [133]. Details of the friction model and the coefficients are provided in Ref. [135]. Fourier’s heat conduction model is coupled with mechanical deformation and failure models to account for thermal conduction in the material. Details of the algorithm and models can be found in Ref. [95]. A more complete summary of the constitutive models used in CODEX, including all relevant equations, is provided in Chapter 2.

An artificial viscosity scheme is implemented to obtain stable shock response under high-intensity loading. The artificial viscosity is a commonly used practical approach to solve issues associated with overshoot of stress at shock wave fronts and spurious oscillations behind the front. von Neuman and Richtmyer [136] first introduced the artificial viscosity method with a quadratic term of velocity gradient for 1-D wave propagations. Later, Landshoff [137] proposed a linear term for the velocity gradient. Campbell et al. [138] explained the effect of each term. The specific form used in this study is

$$q = \begin{cases} \rho c_L l a \left\{ \mathrm{tr}(\boldsymbol{D}) \right\} - \rho c_Q l^2 \left\{ \mathrm{tr}(\boldsymbol{D}) \right\}^2, & \text{if } \mathrm{tr}(\boldsymbol{D}) < 0; \\ 0, & \text{if } \mathrm{tr}(\boldsymbol{D}) \geq 0. \end{cases} \tag{20}$$

In the above relations, q is a pressure correction associated the artificial viscosity, ρ is mass density of the material, l is a characteristic grid length taken as the square root of the element area ($\sqrt{A}$), and $\mathrm{tr}(\boldsymbol{D}) = D_{11} + D_{22} + D_{33}$ is the trace of the rate of deformation tensor. c_L and c_Q are viscous parameters for the linear term and the quadratic term, respectively. The values are $c_L = 0.06$ and $c_Q = 1.5$, as reported in Ref. [139]. A material with behavior described by the elasto-viscoplastic model under shock loading shows less significant overshoot and oscillations of stress compared with a material with elastic behavior due to energy dissipation associated with plastic deformation. Stability analyses are carried out not only for conditions of viscoplasticity, but also for the conditions of the more challenging elasticity. Figure 14 shows a comparison between the pressure profiles of a shock wave with artificial viscosity and without artificial viscosity for an elastic model of HMX under loading with $U_P = 400\,\mathrm{m/s}$. The algorithm with the artificial viscosity allows

stable shock profiles without stress overshoot and spurious oscillations to be obtained. The introduction of an artificial viscosity may lower the shock velocity. Therefore, the parameters need to be calibrated such that the effect of the artificial viscosity on the shock velocity is negligible. To verify the implementation of the B-M EOS along with the artificial viscosity, the calculated Hugoniot or relation between shock velocity and particle velocity ($U_S - U_P$) is compared to that from experiments [140], as shown in Figure 15. The black dotted line is from the analytical solution of B-M EOS, and the red dots are from CFEM calculations with the B-M EOS and the artificial viscosity. A slight decrease in shock velocity from the CFEM calculations (red dots) is seen as compared to the analytically obtained shock velocity from the B-M EOS (black line), but the difference is negligible. The numerical result agrees with the experimental data (blue marks).

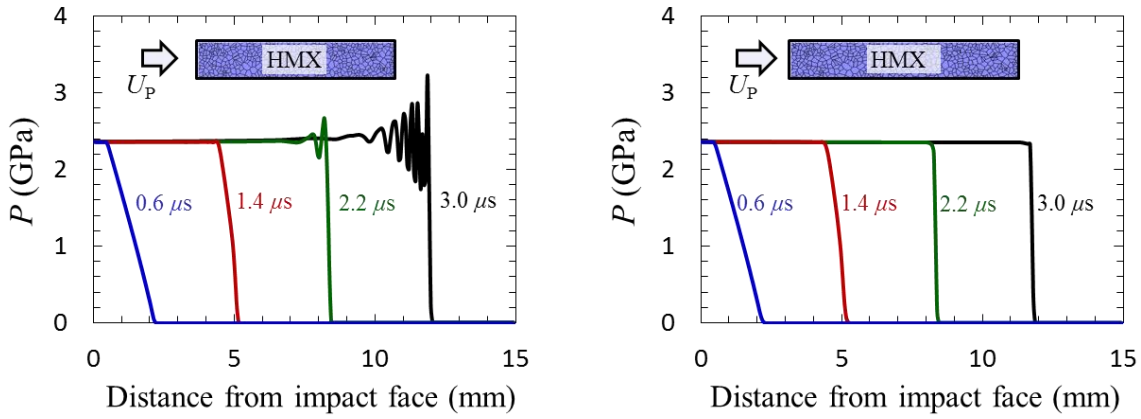

Figure 14 - Comparison between the pressure profiles of a shock wave, (a) without artificial viscosity and (b) with artificial viscosity for an elastic model of HMX under a shock intensity of U_P = 400m/s.

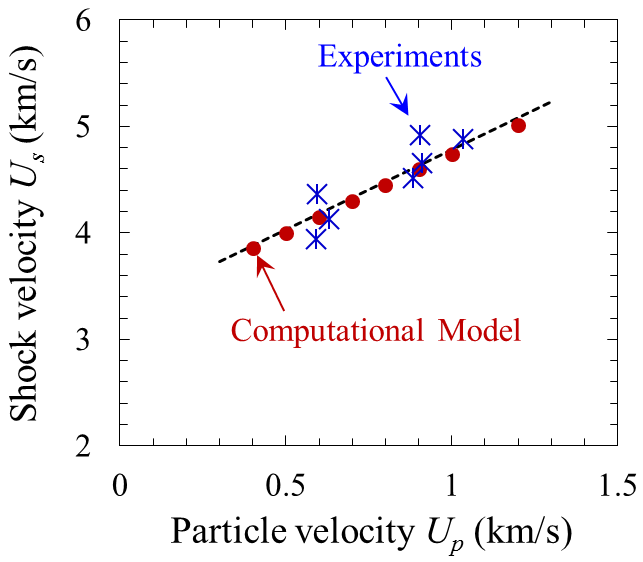

Figure 15 - Comparison of calculated Hugoniot ($U_S - U_P$ relation) and experimental data (Ref. [49]) of HMX.

Interfacial debonding and arbitrary fracture patterns are explicitly captured by the use of cohesive elements embedded throughout the finite element model. The cohesive elements follow a bilinear traction separation law described by Zhai et al [118]. The cohesive relation embodies an initial reversible separation processes with a certain separation limit, followed by irreversible damage and separation beyond the limit. A cohesive surface pair is considered as failed and, therefore, has no further tensile strength if the separation reaches a critical distance. A verification of the cohesive element framework is provided in Ref. [95].

The formation of a crack (inside a gain or along a grain boundary) results in the creation of two surfaces. At each computational time step, the entire domain is scanned and such surfaces are identified. The corresponding nodal coordinates of all possible pairs of surfaces are compared to detect surface contact and overlap. Penalty forces are applied

to strongly discourage interpenetration and maintain proper contact of the surfaces. Detailed descriptions of the multi-step contact algorithm and the penalty forces are given in Ref. [120]. Frictional heating due to sliding along surfaces in contact is assessed using the Coulomb friction law. The stick-slip state is determined by the normal force between contact surface pairs.

Temperature in the material under dynamic loading rises locally due to inelastic bulk dissipation and frictional dissipation along interfaces. Heat conduction is considered. The specific form of the heat equation is

$$\rho c_v \frac{\partial T}{\partial t} = k\nabla^2 T + \eta \dot{W}^p + \dot{W}^{fric}, \tag{21}$$

where c_v is specific heat, T is temperature, t is time, k is thermal conductivity, η is the fraction of plastic work that is converted into heat, $\dot{W}^p$ is the rate of plastic work, and $\dot{W}^{fric}$ is the rate of frictional dissipation.

3.2.4 Initiation vs. Growth of Reaction

This chapter focuses on the establishment of an ignition threshold associated with the development of critical hotspots. The analysis does not attempt to address the issue of growth to detonation transition that critical hotspots undergo. The model considers the attenuation of the shock wave as it travels through the sample, without considering the detonation waves from critical hotspots behind the shock front. This approach is quite reasonable as the process leading up to the formation of critical hotspots does not involve detonation, which occurs later. Since of the relevant and dominant mechanisms of heat

generation during this stage are mechanical irreversibilities (plastic deformation and fracture/friction), the only mechanism of heat loss from hotspots is thermal conduction which is accounted for in this model.

The criticality condition for thermal explosion is identified as the ignition thresholds (boundaries between go and no-go). The justification for this assumption is based on the careful analysis of in-material gauge records of HMX and TATB based explosives by James and Lambourn [141]. They showed that the reaction (behind the shock wave front) is a function of shock strength and time along the particle path, and is independent of local flow variables behind the shock such as pressure and temperature. In other words, "the growth in the pressure or temperature fields does not feed back to the reaction rate". This observation is fundamental to the present study because it implies that the criticality of hotspots in the sense of thermal explosion [142] directly correlates to the initiation of detonation. It also implies that the collective behavior of hotspots may influence the time to detonation, but may not affect the minimum shock threshold condition for initiating detonation, at least to first order. However, the role of distributed hotspots on the go-no-go criticality is not yet well understood [143]. Based on the observations above, we assume that there is a one-to-one correlation between the existence of critical hotspots which lead to local thermal runaway and the occurrence of eventual detonation.

3.3 Results and Discussion

A systematic quantification of the ignition of the HMX samples is carried out, focusing on the shock intensity, shock pulse duration, and the average grain size of the microstructure. The overall procedure is illustrated in Figure 16. The analysis is performed

in the following steps. First, three sets of microstructures with three average grain sizes are generated, with samples in each set having similar statistical attributes (e.g., average grain size and grain size distribution), as shown in Figure 9 and Figure 10. Second, CFEM calculations are carried out using the samples under the loading conditions as discussed in Section 3.2.2 and shown in Figure 16(a). Temperature fields are obtained from the simulations as illustrated in Figure 16(b). To ascertain the validity of the results relative to experiments, the attenuation of the stress waves as it traverses the samples is analyzed. Third, temperature fields and the size-temperature state of each hotspot is determined, as illustrated in Figure 16(c). The ignition criterion described in Chapter 2.2.5 is used to identify critical hotspots that have reached the size-temperature threshold. The ignition of the sample is determined by the existence of sufficient critical hotspots. Fourth, the ignition (go) or no ignition (no-go) condition in terms of the power flux and the energy fluence (measures for loading) for each sample is recorded, as illustrated in Figure 16(d). The overall probability of ignition for each material set is determined using the aggregate data set of go-no go states of all samples in the power flux - energy fluence $\left(\Pi - E\right)$ space. Detailed discussions on the probability of ignition will be given in Section 3.3.3.

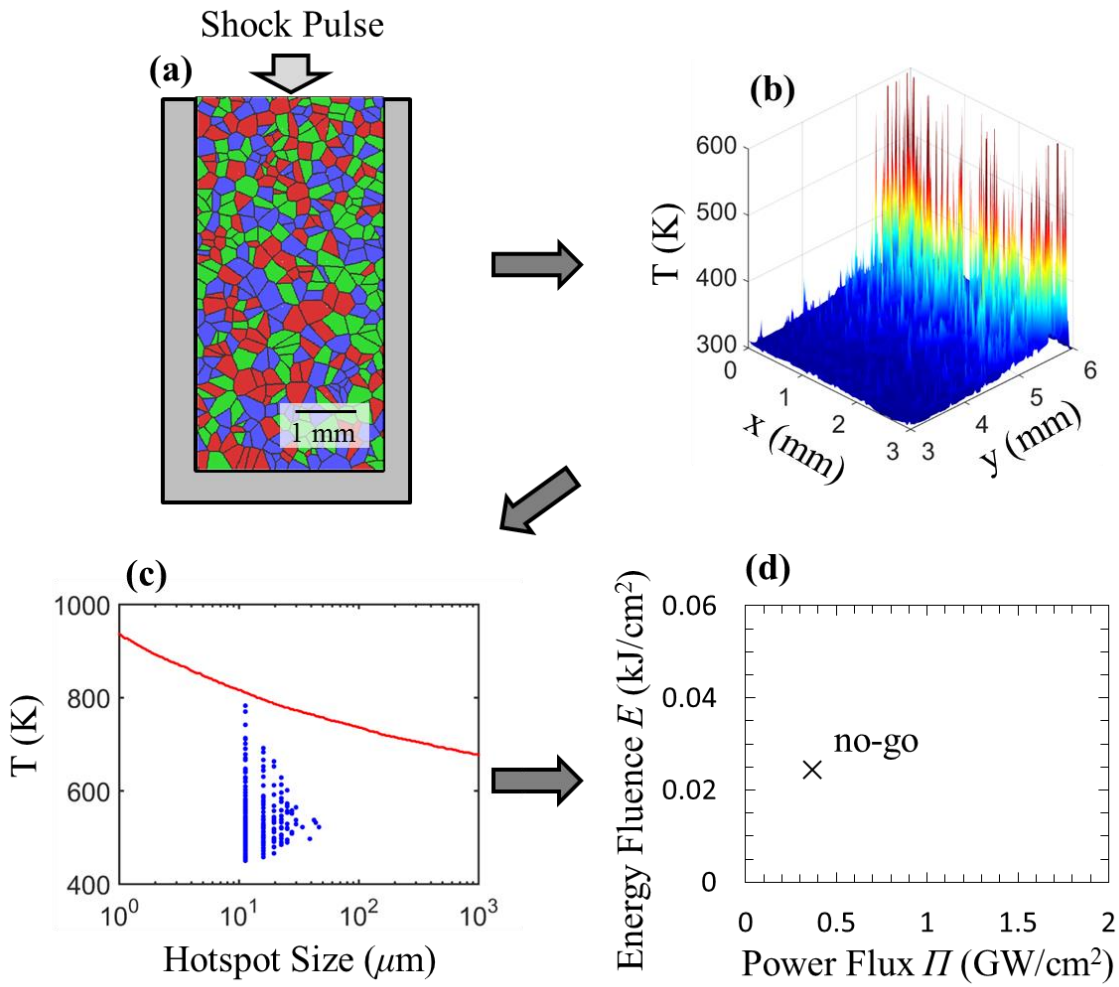

Figure 16 - Illustration of the hotspot-based approach for ignition threshold prediction. (a) Microstructure generation and CFEM simulation, (b) Temperature field, (c) Hotspot characterization from the temperature field and determination of the criticality of the sample via hotspot size-temperature states, and (d) determination of the "go" or "no-go" condition for each sample in the *E* –*Π* space.

3.3.1 Analysis of Stress and Temperature

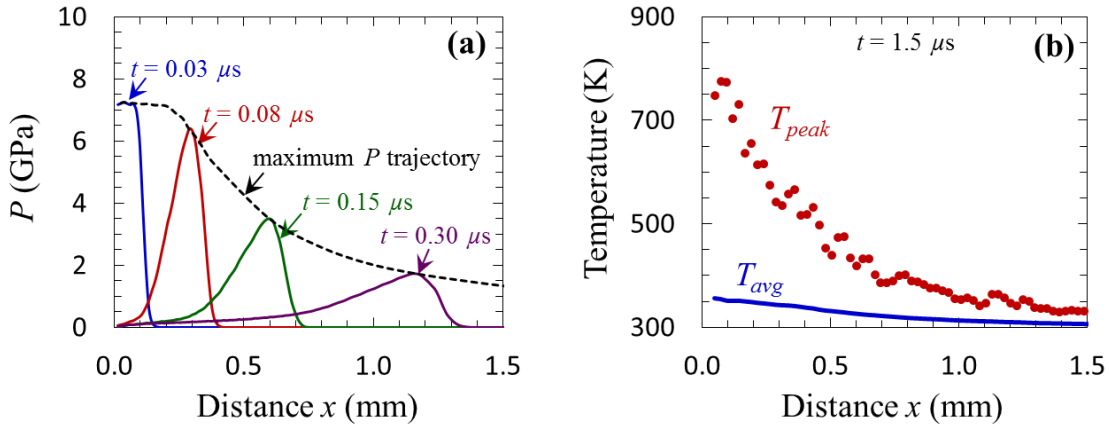

Figure 17 - (a) The calculated trajectory of peak pressure and (b) corresponding temperature profile under shock pulse loading with for a sample of d_{avg} = 220 μm.

The temperature of the material increases due to energy dissipation from material inelasticity and friction along crack faces under high stress. The dissipation also causes the shock wave to attenuate as it propagates. The peak pressure trajectory from the calculations and the corresponding temperature profile under loading with $U_p = 900\,\text{m/s}$ and $\tau = 38\,\text{ns}$ are shown in Figure 17. Note that the peak pressure as well as the average and peak temperatures decrease spatially as the shock wave propagates into the material.

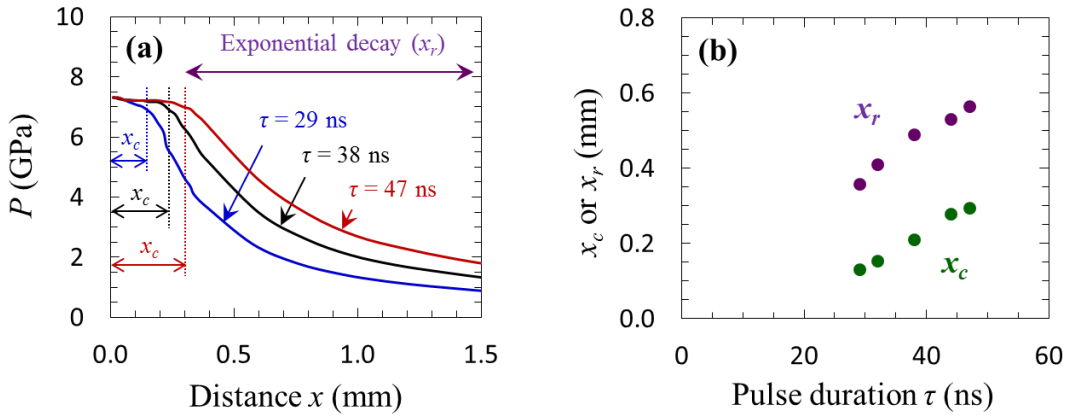

Figure 18 - Effect of pulse duration on stress attenuation under shock pulse loading with for a sample of d_{avg} = 220 µm, (a) profiles of pressure for the durations of τ = 29, 38, and 47 ns and (b) corresponding rarefaction point (x_c) and decay distance scaling parameter (x_r).

Impact by a thin flyer creates a short duration pulse, which attenuates as the shock wave propagates through the material, as described in Ref. [144]. Initially, the peak pressure remains constant from the impact face to the rarefaction point (x_c), after which release waves from the impact face overtake the shock wave, causing attenuation of the peak pressure. The distance (x_c) and the degree of attenuation vary depending on the material and initial pulse duration (which depends on flyer thickness), as described in Ref. [145]. The attenuation of pressure is often quantified with an exponential form in terms of distance from the impact face, as discussed in Ref. [146]. The exponential form has been shown to model the dependence of particle velocity (U_p) on the shock velocity (U_S) [147]. The trajectories of peak pressure for different pulse durations between $\tau = 29 - 47\,ns$ are shown in Figure 18(a). The trend can be described by

$$P_{peak} = P_1 \exp\left(-\frac{x - x_c}{x_r}\right) + P_2, \text{ for } x > x_c, \tag{22}$$

where the rarefaction point is at $x = x_c$ at which the peak pressure begins to attenuate. x_r is a scaling parameter that defines the slope of the attenuation. P_2 is the asymptotic pressure at far distances and $(P_1 + P_2)$ is the peak plateau pressure on *the* interval $0 \le x \le x_c$. The trajectories of the peak pressure as shown in Figure 18(a) are fitted to Eq. (22) for the range of $x \le 3\text{mm}$. Figure 12(b) shows the dependence of x_r and x_c on pulse duration τ. As the pulse duration (τ) increases, the rarefaction distance (x_c) increases, indicating that the peak pressure plateaus for a longer distance before it starts to attenuate. Likewise, as the pulse duration (τ) increases, the distance scaling parameter (x_r) decreases, indicating that the pressure attenuates more slowly as it propagates through the material. Figure 19 shows the relationship between the pulse duration and the distance parameters (x_r and x_c) over the range of $U_P = 700 - 1200\,\text{m/s}$. The relationships between the pulse duration and distance parameters, x_r and x_c, are linear. The distance parameters for all shock intensities considered fall along the same lines, indicating that they are highly dependent on pulse duration but are not strong functions of the load intensity. The effect of shock intensity on attenuation is captured by P_1 and P_2. The values of the parameters for the linear relationships between pulse duration τ and the distance parameters, x_r and x_c, are listed in Table 9. The threshold time (t_0^c) for x_c in Figure 19 and Table 9 is 10 ns which is equal to the ramp time of the applied boundary loading (Figure 12(b)). This coincidence indicates that if the pulse duration is as short as the ramp time, the shock wave begins to attenuate instantly without staying at plateau

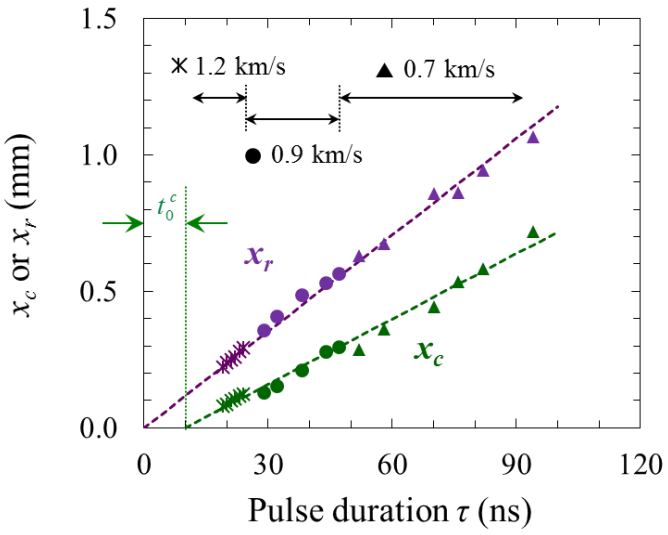

Figure 19 - Relationship between pulse duration and distance parameters (x_r and x_c) over the loading range of U_P = 700-1200 m/s.

Table 9. Coefficients of the linear relations between x_r and t_{pulse} and between x_c and t_{pulse}

$x_r = a_r \cdot (\tau - t_0^r)$	$a_r = 0.0118\,\text{mm/ns}$	$t_0^r = 0\,\text{ns}$
$x_c = a_c \cdot (\tau - t_0^c)$	$a_c = 0.0080\,\text{mm/ns}$	$t_0^c = 10\,\text{ns}$

3.3.2 Ignition Threshold

The samples in the experiments are 12.7 mm in length, which is a sufficient distance to see the stress attenuate to very low levels as the loading pulse reaches the bottom of the samples. The attenuation is so pronounced, that only a small portion of the samples close to the impact face experience severe enough loading over the duration of the experiments

to yield hotspots having the potential to cause ignition. Indeed, the computational results show that most hotspots are generated within a distance of $0 < x < 1\text{-}2 \text{ times } x_c$ from impact face and no hotspots are seen for any distance $x > 4\text{-}5 \text{ times of } x_c$. Therefore, the shock pressure significantly diminishes as the wave reaches x = 6 mm. Specifically at this distance, the pressure of a sample subjected to loading with $U_p = 700\,\text{m/s}$ and $U_p = 900\,\text{m/s}$ decreases to 10% and 5% of the initial shock pressure, respectively. Welle et al. [148] investigated the effect of sample height and found no significant variations in the ignition threshold for a height range of 6 -19 mm. Because of this, we stop our calculations when the stress wave reaches the bottom of the samples and analyze the temperature field for hotspots, knowing that further propagation and reflection of the wave from the bottom have negligible effects on hotspot formation. This approach is essentially equivalent to using an infinitely long sample in which the stress wave does not reflect.

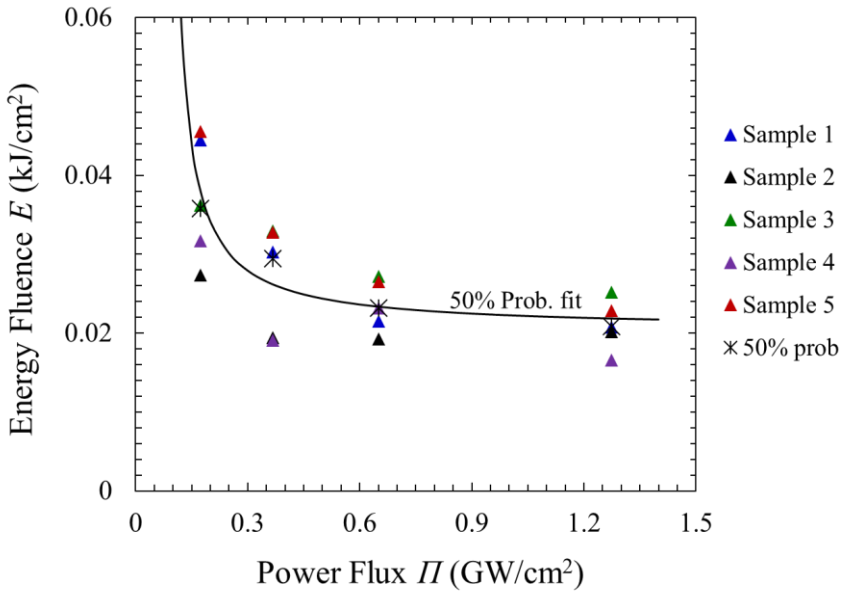

Figure 20 - Minimum energy required for ignition from five samples and 50% probability. The samples used here have statistically similar microstructures with the average grain size of d_{avg} = 220 µm as shown in Figure 10.

The critical energy threshold for ignition is analyzed using the hotspot ignition criterion discussed in Chapter 2.2.5. Figure 20 shows the minimum energy input E required for ignition (or energy fluence). Five statistically equivalent samples are computationally analyzed at each energy input rate (or energy flux). The different samples, just like different samples of the same material in experiments, require slightly different levels of energy fluence (as reflected in slightly different pulse durations they require for reaching ignition) under the same load intensity or energy flux (energy input rate). Here, the shock intensity is expressed in a power flux form (i.e., $\Pi = PU_p$). Although the individual samples have the same overall statistical microstructural attributes therefore mimicking multiple samples of the same material batch in experiments, the random grain shapes and grain distributions cause the samples to have local fields that fluctuate, thereby giving rise to slightly different

behaviors and slightly different energy fluence values even under the same overall loading condition. The asterisk in the figure demarcates the threshold for 50% probability of ignition as determined by all samples over the entire load regime analyzed. To determine this 50% threshold, the following James-type relation is used to provide an overall fit.

$$1 = \frac{E_c}{E} + \frac{\Pi_c}{\Pi}, \tag{23}$$

where the cutoff energy fluence E_c and the cutoff power flux Π_c are fitting parameters which represent asymptotic thresholds for the critical energy fluence and the critical power flux, respectively. This relation is based on the James relation [54] and is obtained by replacing the specific kinetic energy ($\Sigma = 0.5 U_P^{\,2}$) in the James relation by the power flux ($\Pi = P U_P$), see Welle et al. [13]. The data points above the 50% threshold curve correspond to ignition probabilities higher than 50%, and the points below the 50% threshold curve represent correspond to ignition probabilities lower than 50%.

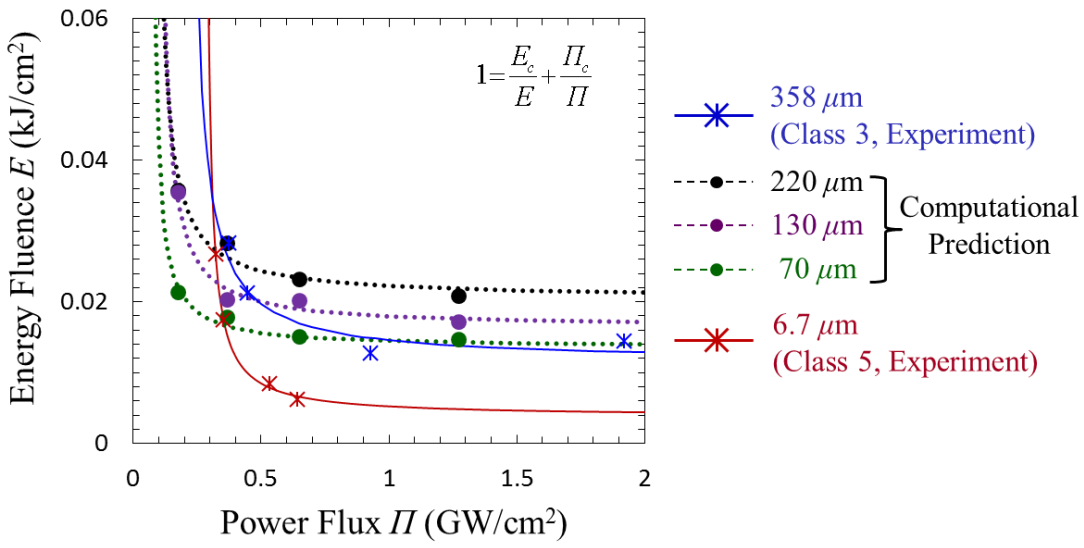

Figure 21 - Computationally predicted 50% ignition thresholds from all grain sizes analyzed (d_{avg} = 70, 130, and 220 µm) and experimentally measured thresholds for Class 3 and Class 5 HMX.

Table 10. Parameters in the modified James relation for materials with different grains sizes

	d_{avg} (μm)	E_c (kJ/cm^2)	Π_c (GW/cm^2)
Experiments	358 (Class 3)	0.01157	0.2072
	6.7 (Class 5)	0.00377	0.2776
Computations	220	0.0205	0.0798
	130	0.0163	0.0919
	70	0.0135	0.0683

The 50% ignition thresholds for the three materials with the average grain sizes of $d_{avg} = 70, 130, \text{and } 220\,\mu\text{m}$ are shown in Figure 21. The corresponding parameters for the

modified James relation (Eq. (23)) for these three cases are listed in Table 10. In general, a higher loading rate (power flux) results in a lower energy required for ignition (lower energy fluence) as indicated by Eq. (23). For a given loading rate (power flux), smaller grain sizes lead to lower ignition thresholds. This effect is more pronounced under strong shock loading (power flux greater than 0.5 GW/cm^2). Khasainov et al. [149] mentioned that heterogeneous explosives with high surface area (corresponding to smaller grains) are more sensitive than those with less surface area (corresponding to larger grains). They observed this trend only at high intensity regime ($P/P_c >> 1$). As shown in Figure 21, the discrepancy in the sensitivity levels of different grain sizes increases as the power flux increases, whereas the sensitivity level discrepancy converge as the power flux decreases until its critical value is reached. The trends observed in the computational predictions are in good agreement with those observed in experimental data, as overlaid in Figure 21. Moreover, the computationally predicted thresholds for grain sizes of $d_{avg} = 70, 130, \text{and } 220\,\mu\text{m}$ lie in the same range as the thresholds obtained by experiments for Class 3 ($d_{avg} = 360\,\mu\text{m}$) and Class 5 ($d_{avg} = 6.7\,\mu\text{m}$) samples with a marginal degree of deviation. Overall, the experimentally measured thresholds are lower than the computational predictions. The difference between the experimental observations and computational predictions may be attributed to the following factors. First, the average grain sizes for Class 3 and Class 5 HMX in the experiments become smaller during the pressing process. So, the actual grain sizes are somewhat smaller than the nominal values stated here. Molek et al. [124] reported that the grain sizes of Class 3 and fluid-energy-milled HMX ($d_{avg} = 4\,\mu\text{m}$) decrease by roughly one or two orders of magnitude after sample preparation. Similar results can also be found in Ref. [43]. Therefore, the ignition

thresholds of Class 3 and Class 5 HMX shown in Figure 21 are actually for grains sizes smaller than nominal values stated in the figure. Second, the computational model is based on a relative density of 100% (fully packed HMX) and provides only a phenomenological account of voids and other defects in the material, whereas the experimental samples have a relative density of less than 100% (94% TMD). Christensen et al. [150] observed that LX-17 PBX samples with higher relative densities are less sensitive (having higher ignition thresholds) than samples with lower relative densities. Third, large "boulders" in the experimental samples are not considered in the simulations, as pointed out earlier. What is important to note is that the overall trends are consistent, with smaller grain yielding lower ignition thresholds. Note that this sensitivity analysis does not account for subcritical hotspots. More information illustrating the effect of subcritical hotspots is presented in Section 3.3.4.

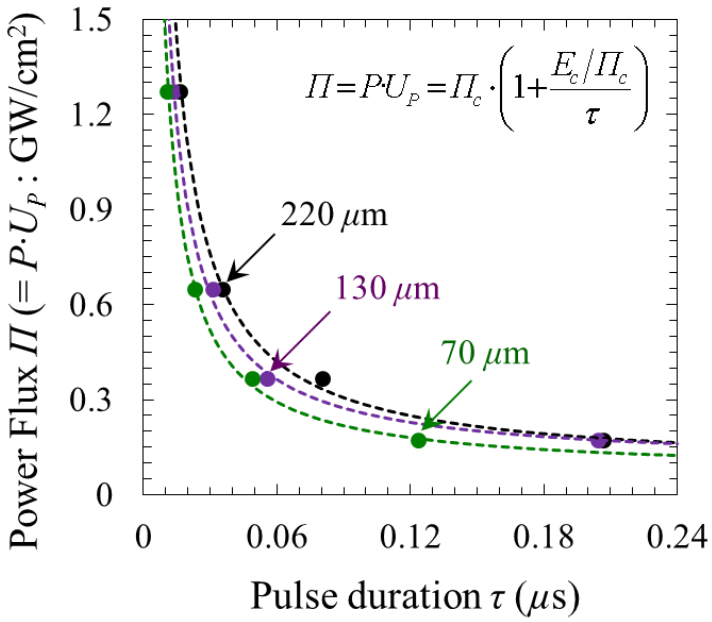

Figure 22 - Fifty percent (50%) ignition probability thresholds in the Π - τ space and the equivalent James relation.

In the modified James relation (Eq. (23)), the power flux ($\Pi = PU_P$) is related to the shock intensity, similar to the specific kinetic energy ($\sum = 0.5U_P^2$). It also represents the rate of energy imparted to the material ($\Pi = dE/dt$) per unit area of material surface. The ignition threshold between input energy E and power flux Π in the E - Π space can also be represented in the Π - τ space. Specifically, the modified James relation as expressed in the Π - τ space is

$$\Pi = P \cdot U_P = \Pi_c \cdot \left(1 + \frac{E_c / \Pi_c}{\tau}\right), \tag{24}$$

where E_c and Π_c are the same parameters as in Eq. (23). This equation in the Π - τ space is an equivalent form of the modified James relation (Eq. (23)). The details of the derivation of the modified James relation and the equivalent modified James relation are given in Appendix A. Figure 22 shows the 50% ignition thresholds (data points denoted by the symbols) for the three grain sizes in the Π - τ space and the corresponding equivalent James relations obtained via curve fitting. To study the application of the equivalent James relation to experimental data, we examine the shock initiation threshold of TATB obtained by Honodel et al. [151]. Figure 23 shows a comparison of the fits with the equivalent James relation (Eq. (24)) and the Walker-Wasley relation $(P^n\tau = C)$ [53]. Both the Walker-Wasley relation and the equivalent James relation have two fitting parameters. The equivalent James relation follows more closely the data points over the entire range, while the Walker-Wasley relation deviates from the experiments in the longer pulse (lower load intensity) regime. The closeness of the fit in the Π - τ space using the equivalent James relation (Eq. (24)) is the same as the closeness of the fit in the E - Π space using the modified James

relation (Eq. (23)), because Eq. (23) and Eq. (24) are algebraically equivalent. The difference is that the Π - τ space directly relates to the physical conditions of the experiments (thickness of the flyer required for ignition at given flyer velocity implied by the energy flux), whereas the E - Π space emphasizes the amount of energy required for ignition at given energy input rate into the material.

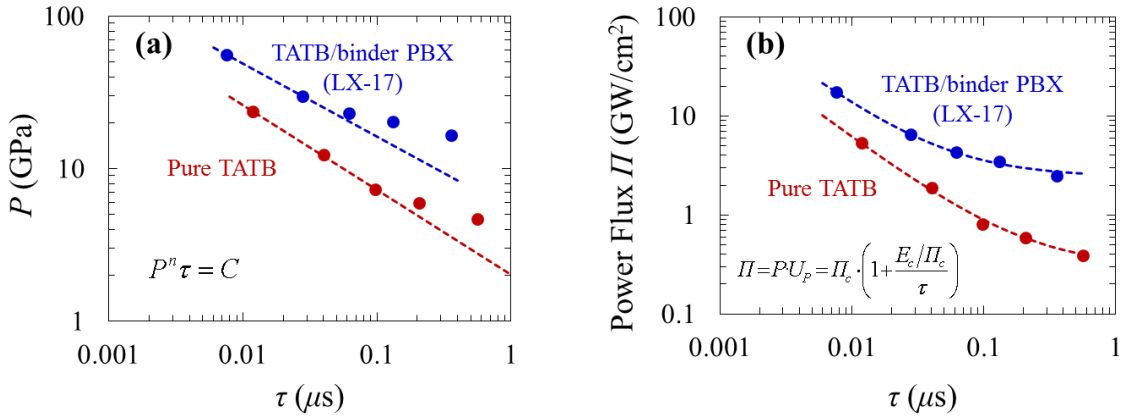

Figure 23 - Comparison of the ignition threshold characterizations using (a) the Walker-Wasley relation and (b) the equivalent James relation. The ignition data of LX-17 and TATB is from Ref. [60].

3.3.3 Probabilistic Quantification: Ignition Threshold for any given Probability of Ignition

The ignition threshold represented by Eq. (23) indicates the shock loading conditions for 50% probability of ignition. To incorporate the energy and power flux conditions required for greater than or less than 50% ignition probability, Gresshoff and Hrousis [106] expanded on the modified James relation by introducing a James number, J. The specific form of the equation is

$$\frac{1}{J} = \frac{E_c}{E} + \frac{\Pi_c}{\Pi}, \tag{25}$$

where $J = 1$ is the modified James relation, $J > 1$ corresponds to shock loading conditions resulting in greater than 50% ignition probability, and $J < 1$ corresponds to shock loading conditions resulting in less than 50% ignition probability. As an example of the application of Eq. (25), Figure 24 shows the modified James relation with $J = 0.75, 1.0, \text{ and } 1.25$ using the data for microstructures with $d_{avg} = 220\,\mu\text{m}$. Each J number accounts for all combinations of loading conditions (i.e., energy fluence and power flux) which results in a certain probability of ignition. The three lines in Figure 24 for $J = 0.75, 1.0, \text{ and } 1.25$ correspond to the three probability fits of 10%, 50%, and 90%, respectively.

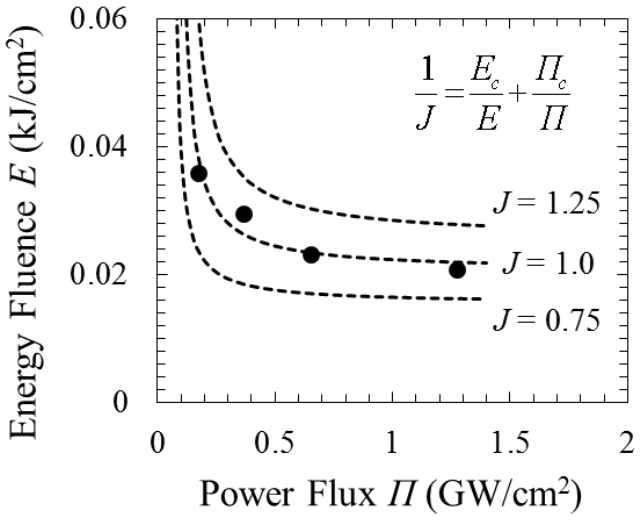

Figure 24 - Modified James relation with $J = 0.75, 1.0, \text{ and } 1.25$ for the material with $d_{avg} = 220\,\mu\text{m}$.

Figure 25 shows the relationship between J (James number) and the ignition probability from the experiment and the computational prediction for all samples. The

truncated normal probability distribution function ($\mathscr{P}(J)$) is used to fit the ignition probability around a mean value of $J=1$. The specific form of the function is

$$\mathscr{P}(J)=\frac{\Phi(J)-\Phi(0)}{\Phi(\infty)-\Phi(0)}, \tag{26}$$

where $\Phi(J)$ is cumulative normal probability distribution [106] in the form of

$$\Phi(J)=\frac{1}{\sigma\sqrt{2\pi}}\int_{-\infty}^{J}\exp\left[\frac{-(x-\mu)^2}{2\sigma^2}\right]dx=\frac{1}{2}\left[1+\mathrm{erf}\left(\frac{J-\mu}{\sqrt{2}\sigma}\right)\right], \tag{27}$$

where μ is the mean value, σ is the standard deviation. Note that $\Phi(\infty)=1$. The parameters used to represent the ignition probability of the samples are listed in Table 11. By combining Eqs. (25), (26) and (27), we can obtain a direct relation between the ignition probability $\mathscr{P}$ and the shock loading condition parameters E and Π in the form of

$$\mathscr{P}(E,\Pi)=\frac{1}{1-\mathrm{erf}\left(-\mu/\sqrt{2}\sigma\right)}\left[\mathrm{erf}\left(\frac{E\Pi}{\sqrt{2}\sigma\left(\Pi E_c+E\Pi_c\right)}-\frac{\mu}{\sqrt{2}\sigma}\right)-\mathrm{erf}\left(\frac{-\mu}{\sqrt{2}\sigma}\right)\right], \tag{28}$$

where $\mathrm{erf}(\cdot)$ is the Gauss error function. Under the conditions of the current analysis, $\Phi(0)\approx 2\times10^{-5}$, therefore, for the range of $0\le J\le\infty$, the difference between $\Phi(J)$ and $\mathscr{P}(J)$ is on the order of 2×10^{-5}, which is negligible. As a result, with $J=\mu=1$ representing an ignition probability of 50%, Eq. (28) simplifies to

$$\mathscr{P}(E,\Pi)=\frac{1}{2}+\frac{1}{2}\mathrm{erf}\left[\frac{1}{\sqrt{2}\sigma}\left(\frac{E\Pi}{\Pi E_c+E\Pi_c}-1\right)\right]. \tag{29}$$

In the above relation, the standard deviation σ, cutoff energy fluence E_c and cutoff power flux Π_c are material constants whose values are determined by experiments or computations reported here (see Table 10 and Table 11). Once these parameters are determined for a material, the probability of ignition $\mathscr{P}$ under any loading condition as measured by E and Π can be calculated directly from Eqs. (28) or (29). The probability $\mathscr{P}$ as a function of E and Π can also be represented as a function of the pulse duration τ and either power flux Π or input energy E. In the previous section, we have shown that the ignition threshold between input energy E and power flux Π in the E - Π space can be represented in the Π - τ space (see Figure 21 and Figure 22). Similarly, the ignition probability $\mathscr{P}$ in Eq. (29) can be recast in the Π - τ space and in the E - τ space as, respectively,

$$\mathscr{P}(\Pi,\tau)=\frac{1}{2}+\frac{1}{2}\mathrm{erf}\left[\frac{1}{\sqrt{2}\sigma}\left(\frac{\Pi/\Pi_c}{1+\tau_c/\tau}-1\right)\right], \text{ and} \tag{30}$$

$$\mathscr{P}(E,\tau)=\frac{1}{2}+\frac{1}{2}\mathrm{erf}\left[\frac{1}{\sqrt{2}\sigma}\left(\frac{E/E_c}{1+\tau/\tau_c}-1\right)\right], \tag{31}$$

where the $\tau_c=E_c/\Pi_c$ is a material-dependent time-scale constant. The values of τ_c from experiments and computations are listed in Table 12. Note that although τ_c can be used as a reference time, is not a measure related to the pulse duration required for ignition in any sense. For high-intensity loading, the pulse duration required for ignition τ can be smaller than τ_c. Likewise, for low-intensity loading, τ can be larger than τ_c.

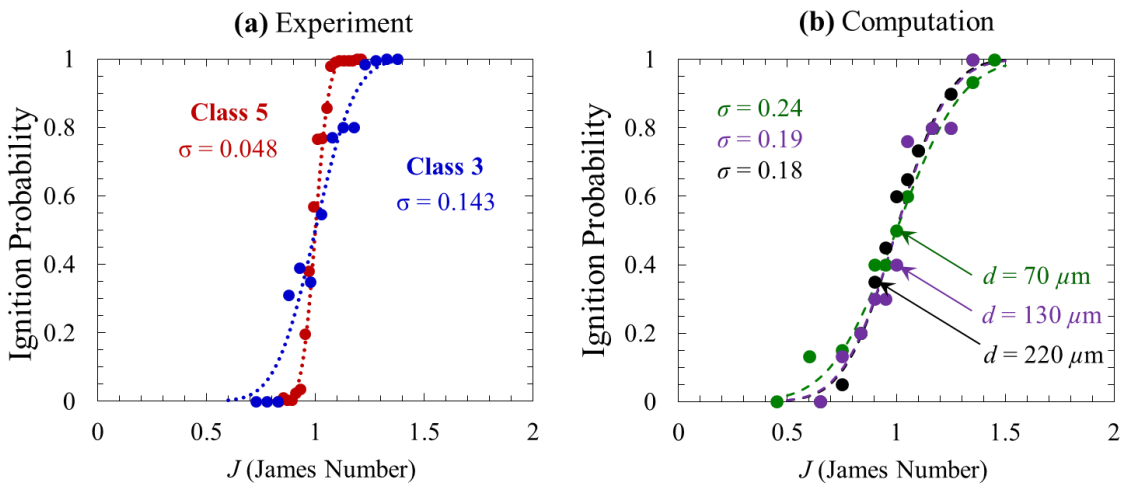

Figure 25 - Relationship between *J* and the ignition probability from (a) experimental results of Class 3 and Class 5 HMX and (b) computational results of grains sizes of d_{avg} = 70, 130, and 220 μm.

Table 11. Mean value and standard deviation for the ignition probability distributions

	d_{avg} (μm)	μ	σ
Experiments	358 (Class 3)	1.0	0.143
	6.7 (Class 5)	1.0	0.048
Computations	220	1.0	0.18
	130	1.0	0.19
	70	1.0	0.24

Table 12. Time scale parameter τ_c obtained from experiments and computations

	d_{avg} (μm)	τ_c (ns)
Experiments	358 (Class 3)	55.8
	6.7 (Class 5)	13.6
Computations	220	257
	130	177
	70	198

The *J*-probability distribution for Class 3 samples from the experiments has a wider spread than that for the Class 5 samples, as shown in Figure 25(a). This trend is consistent with what is reported by with Schwarz [108, 152] who found that samples with lower specific interface areas (SIA) demonstrate a wider spread of ignition probability. The computational predictions for the three average grain sizes $\left(d_{avg} = 70, 130 \text{ and } 220\,\mu\text{m}\right)$ in Figure 25(b) have similar *J*-probability distributions. The difference between the experimental and computational results may be attributed to the following factors. First, the grain size distribution of the experimental Class 5 samples is much wider than that of the Class 3 samples (see Table 1 in Ref. [148]). On the other hand, the grain size distributions of the computational microstructures have the same spread (see Figure 9). Second, the experimental samples have a much larger average grain size difference while the differences between the average grain sizes of the computational microstructure sets are much smaller. The difference between Class 3 and Class 5 is 53 times, whereas the differences among the computational sets are at most 3 times. The similarity in the distributions of ignition probability among the three computational sets does not mean that

average grain size does not significantly affect ignition. On the contrary, the average grain size significantly affects the ignition thresholds for all ignition probability levels (as seen in Section 3.3.2). For example, the thresholds for $J = 1$ (or 50% ignition probability) for the different grain sizes are significantly different, as shown in Figure 21 and by the parameters E_c and Π_c in Table 10.

The distributions of ignition probability from the experiments have standard deviations of $\sigma = 0.048 - 0.14$ and the calculated distributions have standard deviations of $\sigma = 0.18 - 0.24$. As mentioned earlier, samples with larger specific interface areas (SIA) result in narrower distributions of ignition probability. The experimental samples have much larger SIAs than the computational samples. Specifically, the SIAs of the computationally-generated microstructures are $0.03 – 0.09\ m^2/g \pm 0.0014\ m^2/g$, one order of magnitude smaller than the SIAs of the samples used in the experiments $(0.866 – 1.62\ m^2/g)$ [13]. One reason for this difference is that the computational samples do not explicitly resolve very small voids and defects inside the grains as well as the surface roughness of the grains. For example, the same order of magnitude of SIA with minimal roughness on surfaces of Al particles is attainable for average particle sizes of a few hundred nanometers (see Table 1 and the SEM images in Yarrington et al. [153]). It is possible to explicitly consider these features in the model in the future, but such an analysis is beyond the scope of the current work in this chapter, which focuses on a new method for predicting ignition thresholds. The differences in experimentally measured and theoretically calculated SIA are discussed by Sánchez et al. [154] who compared measured SIA values and theoretically obtained SIA values based on particle size distributions. They

reported that measured SIA values are an order of magnitude higher than theoretical SIA values due to particle morphology (roughness) and internal micro porosity.

Overall, the similarity in the distribution curves in Figure 25 shows is that (1) J serves as an effective normalizing parameter for the examination of the probability of ignition distribution around a given reference probability level (which is taken as $J = 1$ or 50% of ignition probability here) for samples with different microstructural attributes, and (2) the ignition probability spread or the distribution around a given reference probability level depends on the microstructure heterogeneity fluctuations in the samples of a given sample set – or, simply put, how "similar to" or "different from" each other the multiple samples in a set are statistically. Specifically, the material-dependent 50% ignition threshold can be analyzed in the $E - \Pi$ space as seen in Figure 21, and the ignition probability around this 50% threshold can be analyzed through the relation between J and the probability $\mathscr{P}$ given in Figure 25. By combining these two relations, we can obtain the material-dependent ignition probability map as shown in Figure 26. This process is equivalent to obtaining Eq. (29) by combining Eq. (25) and Eq. (27). As Figure 26 shows, the ignition probability level in the $E - \Pi$ space is highly dependent on microstructure.

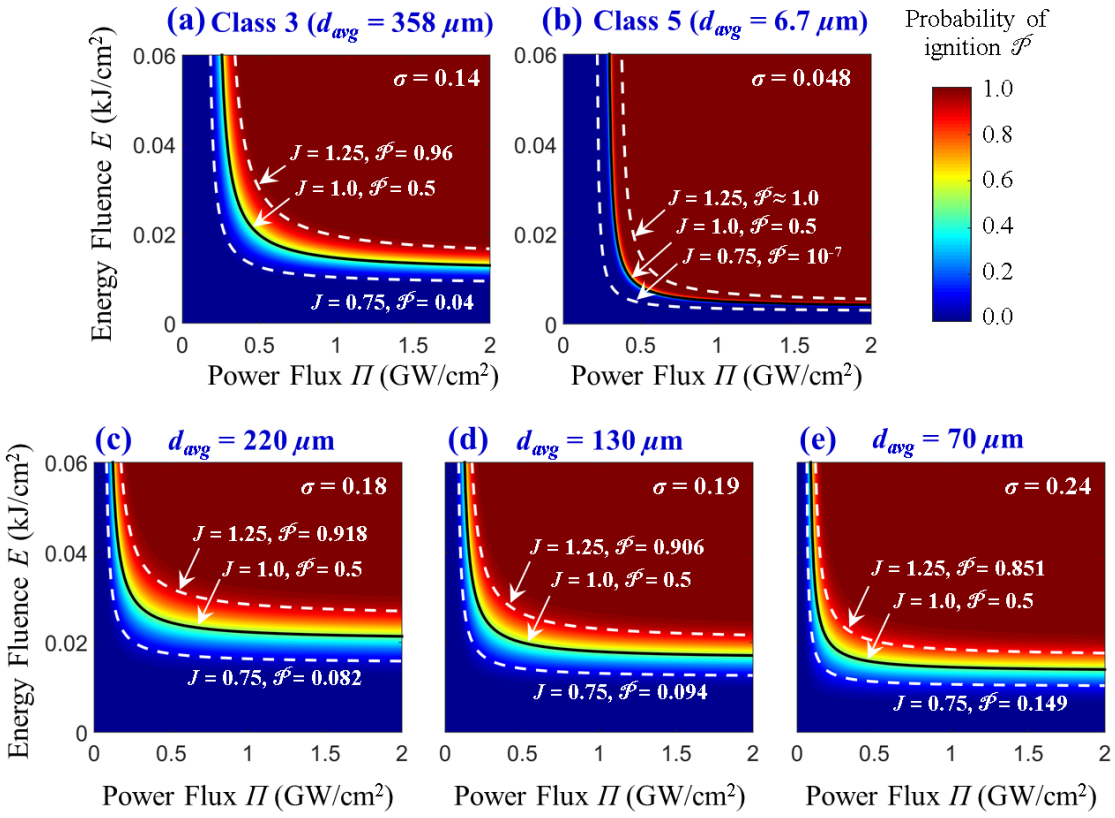

Figure 26 - Ignition probability distribution maps, (a-b) obtained from experiments for (a) Class 3 and (b) Class 5 pressed HMX, and (c-e) predicted from simulations for samples with (c) $d_{avg} = 220\,\mu m$, (d) $d_{avg} = 130\,\mu m$, and (e) $d_{avg} = 70\,\mu m$. The vertical axes of all figures have the same scale and unit as shown in the left most plot in the top and bottom rows.

3.3.4 Macroscopic and Microscopic Ignition Risk Factors

While J allows overall, macroscopic, material level ignition risk to be quantified, it is also possible and desirable to assess the ignition risk at the microscopic, individual sample level by studying its unique hotspot evolution. In the end, a relationship between the ignition of individual samples and the ignition risk of a material can emerge from such an analysis. To this end, this section focuses on the state of individual hotspots in a sample

and introduces a quantitative measure to assess the risk for ignition of each individual hotspot, with the understanding that the most dominant hotspots with the highest risk factors determine the ignition risk of a sample. The specific risk factor we define here is the *R*-value, or "risk" value for an individual hotspot. It can also be referred to as the hotspot ignition risk determinant (HIRD) and depends on the proximity of a hotspot's size-temperature state to the criticality condition embodied in Eq. (12). *R* is a measure for the proximity of a hotspot to the ignition threshold defined as

$$R = \frac{(T - T_i)}{(T_c - T_i)}, \tag{32}$$

where T is the temperature of a hotspot of diameter d, T_c is the critical threshold temperature for ignition for a hotspot of diameter d, and T_i is an initial reference temperature (chosen here as 300 K). Since the temperature and size combination of a hotspot depends on the area chosen to be analyzed (smaller cores of a hotspot have higher temperatures), the hotspot core size and *R*-value are calculated for different temperature levels (see Figure 27 – "Step 1"). The maximum value of *R* for each hotspot is taken as the *R*-value for that particular hotspot (Figure 27 – "Step 2"). This definition of *R* is a direct measure of how close a hotspot is to the ignition threshold. If $R = 0$, the hotspot is at the initial temperature ($T = T_i$) of the material at the beginning of loading. If $R = 1$, the hotspot is deemed critical ($T = T_c$) or has reached criticality (as defined in Section 2.2.5). Subcritical hotspots have $0 < R < 1$. The *R* value of a hotspot is the maximum value of *R* calculated using different cutoff temperatures in the analysis of the size-temperature state of that hotspot. The *R*-value allows hotspots to be grouped and analyzed via an *R*-curve,

based on a histogram of all the *R* values for a sample. Figure 27 illustrates the number and states of critical and subcritical hotspots in a sample (see "Step 3"). It is important to note that $R > 1$ indicates hotspot states that are above the ignition threshold. Since the focus of the analysis here is only on the attainment of the threshold, such values are rounded down to 1 in the analysis carried out here. This treatment simply means that $R \geq 1$ indicates ignition, and since the ignition threshold is the sole concern here, no post ignition analysis is carried out.

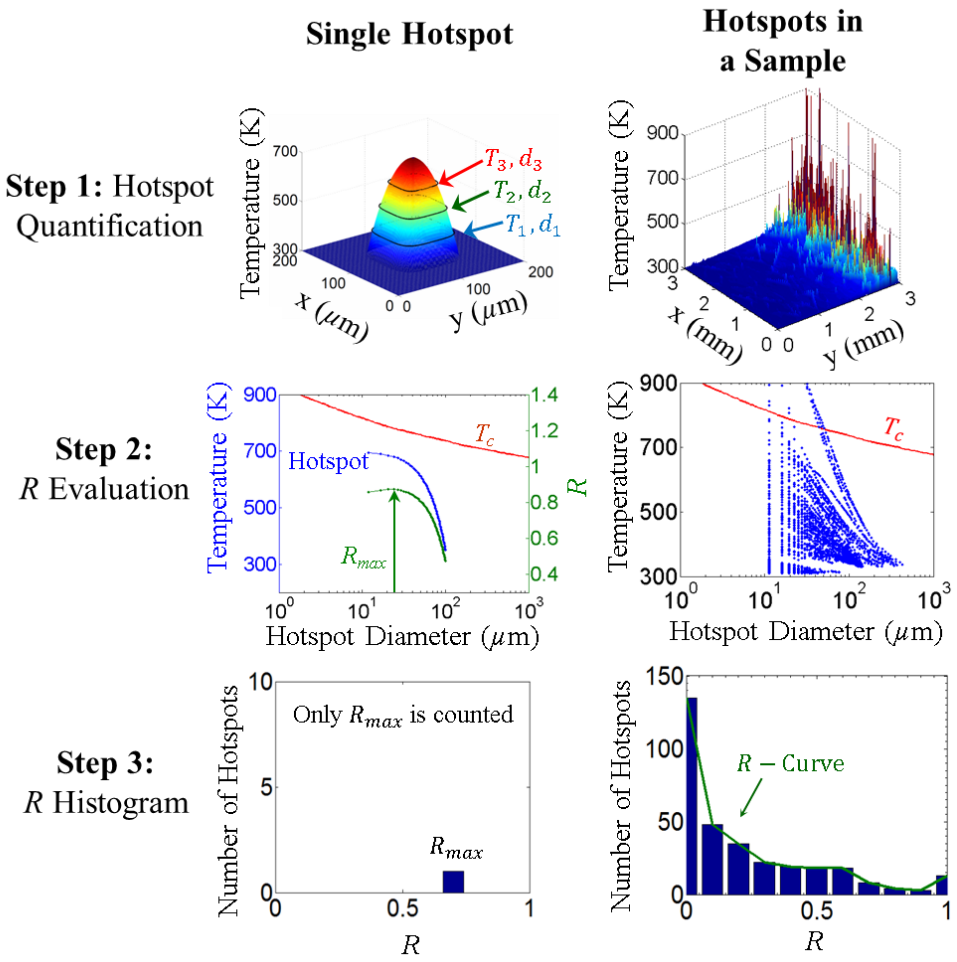

Figure 27 - The evaluation of *R*-value from a single hotspot and the *R*-Curve from a temperature field.

Characterizing each sample with an *R*-curve makes it possible to compare the relative states of multiple samples in a holistic manner, accounting for the influence of all dominant hotspots. Figure 28 shows the average *R*-curves for the samples with the average grain sizes of $d_{avg} = 70, 130, \text{ and } 220\,\mu\text{m}$ under identical loading conditions (U_p = 900 m/s and τ = 35 ns). Each *R*-curve shows the average hotspot count of the five statistically similar samples in the set. The error bars show the extent of variations among the five samples. When compared to the experimental results for varying grain sizes, these *R*-curves demonstrate the correlation of hotspot quantity to overall sample sensitivity, which has been demonstrated to be related to the average grain size in Section 3.3.2. Samples with increased sensitivity to ignition are found to have a higher number of subcritical hotspots. In other words, for any given *R* value, the samples with lower average grain sizes have, on average, greater than or equal to the number of hotspots as samples with larger average grain sizes.

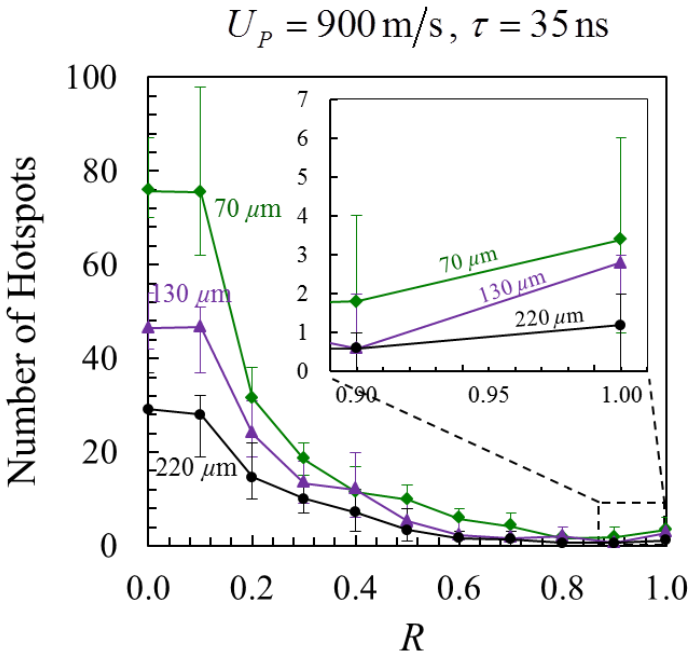

Figure 28 - Comparison of *R*-curves between sample sets with average grain sizes of $d_{avg} = 70, 130,$ and $220\,\mu\mathrm{m}$. The error bars indicate degree of variations among multiple samples in each material set.

As a practical matter in the analysis reported here, in order to obtain a single *R*-value for each loading condition and sample, the average of the top two *R*-values in the sample is used. Two hotspots in the RVE correspond to a hotspot density of $0.22\,\mathrm{mm}^{-2}$. Ten *R*-values are used for each loading condition: five samples and the highest two *R*-values per sample. Since $T_i = 300\,\mathrm{K}$, $R = 0$ corresponds to $J = 0$. This makes intuitive sense because the only way for *J* to remain zero is if the sample has not been subjected to loading and no temperature increase is observed.

The *R*-value and *R*-curve focus on the local conditions of individual hotspots in a particular sample. Both the *R*-value and the *J*-value (discussed in Section 3.3.3) measure the likelihood of ignition. Note that for a given *J* value, some samples in a material set have

ignited (with $R \geq J$) while other samples have not ignited (with $R < J$). For example, for $J = 1$ or an ignition probability of 0.5, 50% of all samples in a material set have reached criticality by definition (with $R \geq 1$) and 50% of the samples have not reached criticality (with $R < 1$). Therefore, R is inherently related to J with some statistical deviation due to microstructure stochasticity, reflecting the fact that J measures the aggregate statistical behavior of a material sample set and R measures the behavior of individual samples in the set. A practical difference between R and J is that R can be calculated from the outcome of a single simulation after analyzing the hotspot map of the sample, while J requires analyzing the results from multiple samples (experimentally or computationally). R can be used to predict and relate to the ignition probability of a material under given loading conditions. While J quantifies the result of this analysis and does not have the predictive power or usage – its ability to "tell" or measure the ignition probability of a material only exists after the outcomes of a set of experiments or simulations have been analyzed and tabulated. Figure 29 shows the correlation between R and J and the 95% probability envelop for the three grain sizes. The standard deviation of the data points about $J = R$ in Figure 29 is σ = 0.17, 0.12, and 0.14 for the three cases, respectively. By studying the relationship between J and R, the inherent connection between loading conditions and hotspot development may be further understood. Since there is a strong correlation between R and J, it is possible to calculate the probability of ignition from a smaller number of samples without having to run a large number of tests or calculations to determine where the ignition threshold for J =1 lies.

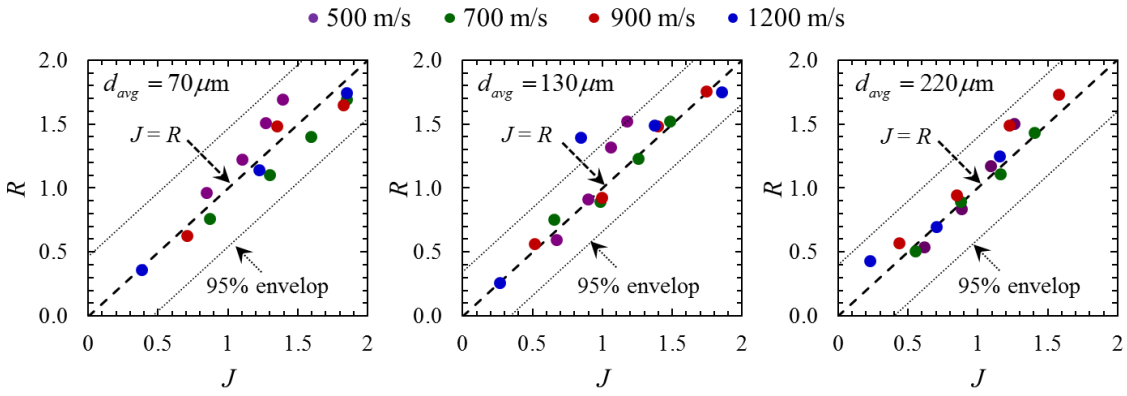

Figure 29 - Correlation between J and R for average grain sizes of $d_{avg} = 70, 130,$ and $220\,\mu$m.

3.4 Conclusion

The ignition thresholds of energetic materials have so far been exclusively determined through experiments. In this chapter, a computational approach for predicating the James-type ignition thresholds via multiphysics simulations is presented. The prediction does not involve calibration or curve fitting with respect to the predicted behavior (ignition threshold), nor does it require prior information about the predicted behavior. Rather, the prediction is based on material microstructural attributes and fundamental constituent as well as interfacial properties. The ignition thresholds are determined via an explicit analysis of the size and temperature states of hotspots in the materials and a hotspot based ignition criterion. The simulations consider the configuration and conditions of actual experiments. Specifically, the simulations account for the controlled loading of thin-flyer shock experiments with flyer velocities between 1.5 and 4.0 km/s on pressed granular HMX explosives with average grains sizes between 70 μm and 220 μm. The choice reflects the interest in comparing the computational predictions

with experimental results. James-type relations between the energy flux and energy fluence for different probabilities of ignition are predicted. To this end, statistically similar microstructure sample sets are computationally generated based on features of micrographs of materials used in actual experiments.

The results show that the grain size significantly affects the ignition sensitivity of the materials at higher energy fluxes, with smaller sizes leading to lower energy thresholds required for ignition. Specifically, the 50% ignition threshold of the material with an average grain size of 220 μm is approximately 1.4-1.6 times that of the material with an average grain size of 70 μm in terms of energy fluence. The predicted thresholds are in general agreement with measurements from shock experiments in terms of trends. The statistical analysis on the ignition threshold lead to a probability-ignition map with respect to loading intensity and energy input. Once the material dependent parameters are determined, the probability of ignition under any loading condition can be calculated. This approach for the probability of ignition leads to the definition of a macroscopic ignition parameter J based on the loading conditions of the sample. A microscopic ignition risk parameter R is proposed based on the evolution of individual hotspots within the sample. The ignition risk parameter R represents the likelihood of ignition of individual hotspots at the microstructural-level, whereas the ignition parameter J concerns the loading intensities and energy input at the macroscopic level. The relationship between the two parameters is obtained. Specifically, it is found that R and J are strongly correlated ($J = R$) with some statistical deviation, reflecting the fact that J measures the aggregate statistical behavior of a material sample set and R measures the behavior of individual samples in the set. This chapter has focused on pressed HMX only. However, the approach, relations, and

capabilities developed here are useful for the analysis and design of heterogeneous energetic materials such as polymer-bonded explosives (PBX) and granular explosives in general.

CHAPTER 4. IGNITION THRESHOLDS OF ALUMINIZED HMX-BASED POLYMER-BONDED EXPLOSIVES

This chapter is based on the work published in Ref. [155].

4.1 Introduction

A common practice in designing high-performance insensitive energetic materials is to incorporate initially inert constituents, which serve as fuel following detonation, but does not directly participate in the detonation process. Aluminum is one such constituent and is commonly combined with a mixture of energetic grains and some form of polymer binder to form an aluminized polymer-bonded explosive (APBX) [60, 156]. Aluminum was first patented to increase explosive performance by Roth in 1900 [55], and over time experiments have optimized the volume fraction of aluminum required to maximize explosive power [56] at around 20%. Experiments show that the addition of aluminum particles decreases detonation velocity while increasing the chemical reaction time [60]. The heat of explosion also increases as aluminum is introduced, which allows the explosive to maintain its total output power while still being less sensitive to ignition [58]. The localized mechanical effects of aluminum particles in PBX during shock loading have yet to be thoroughly analyzed. Since hotspots are localized phenomena, understanding the effects of aluminum and how it interacts with energetic granules on a microscale is critical to the development of insensitive energetic materials. So far, there is a lack of systematic and quantitative study on the effects of aluminum on the ignition and detonation behaviors of polymer-bonded explosives (PBXs).

In this chapter, we quantify the effects of aluminization by simulating the thermomechanical processes in the microstructures of PBXs under shock loading from impact by thin flyers using a recently developed Lagrangian cohesive finite element method (CFEM) [95, 96, 110, 157]. The focus is on the ignition behavior. The PBXs studied are a combination of Octahydro-1,3,5,7-tetranitro-1,3,5,7-tetrazocine (HMX) grains, Estane binder, and Al 7075 alloy particles. The CFEM model accounts for constituent elasto-vicoplasticity, viscoelasticity, bulk compressibility, fracture, interfacial debonding, internal contact, bulk and frictional heating, and heat conduction. This framework allows for explicit tracking of frictional heating, which is an often overlooked source of heat generation in many models and codes and can significantly affect the generation of hotspots in fully packed HMX (as shown in Chapter 3) [19] and PBXs [38, 40, 157]. The formation of hotspots is extremely microstructure-dependent. In this chapter, multiple samples are analyzed in order to represent the natural stochasticity present in real experimental microstructures. The sample sets have aluminum concentrations of 0%, 6%, 10%, and 18% by volume. The volume fraction of the polymer binder is 19% in all cases, and the remaining volume of the microstructures are occupied by a bimodal distribution of randomly distributed HMX grains. This bimodal size distribution of HMX grains include both large and small grains similar to those commonly seen in PBXs in experiments. At different stages of shock loading, analyses are carried out to identify critical hotspots using an ignition criterion (see Chapter 2.2.5) that factors in hotspot size and temperature distribution and accounts for thermal and chemical effects [96]. If a specified critical hotspot density threshold is exceeded, the sample is assumed to reach criticality.

As far as what can be found in the open literature, the first reported attempt to quantitatively characterize the desensitization effect of aluminum on the ignition of aluminized PBX [112] focused on delineating the relative importance of each heating mechanism by directly correlating the loading conditions with time to criticality after onset of loading. While the analysis is insightful, the use of the time to criticality as the measure for material behavior represents only an indirect approach as this quantity is not directly measurable in experiments and is not normally used in application. Here, we adopt a more direct approach by using a probabilistic ignition criterion in the forms of the modified James criterion proposed by Gresshoff and Hrousis [106] and Welle et al. [13] and the Walker-Wasley criterion [53]. Since the criteria use macroscopically measurable quantities that are routinely used in engineering and material analyses, the work presented in this chapter can be regarded as one of the first successful attempts at linking the microstructural attributes of APBXs to practically useful engineering performance measures. Furthermore, quantitative analytical expressions for the probability of ignition as functions of loading are explicitly established. Conversely, these relations also yield the macroscopic ignition thresholds in the James space and Walker-Wasley space for any given level of ignition probability. It is important to note that this analysis only examines the hotspot heating up until the point of criticality; the focus here is not to analyze the subsequent effects of chemistry following hotspot criticality and the resulting thermal explosion. By definition, once a hotspot reaches criticality, the heat generation due to chemistry occurs more rapidly than heat loss due to conduction (Eq. (11)) which implies the sample will eventually reach ignition. Studying the governing physics leading to hotspot criticality is sufficient for the sensitivity analysis presented in this work. Future work studying the effects of hotspots

post criticality, including the entire shock to detonation (SDT) is presented in Chapters 5 and 6.

4.2 Framework of Analysis

In this analysis, we focus on the ignition behavior of aluminized HMX-based PBX under shock pulse loading. The microstructure generation, physical models, and initiation prediction models are outlined in this section.

4.2.1 Microstructure

The microstructures used in these simulations consist of HMX grains and aluminum particulates distributed in an Estane matrix. The volume fraction of the Estane binder remains a constant 19% volume fraction of an entire microstructure. The aluminum and HMX combined constitute the remaining 81% of the volume fraction in the following four concentrations: 1) 0% Al, 81% HMX; 2) 6% Al, 75% HMX; 3) 10% Al, 71% HMX; and 4) 18% Al, 63% HMX. Samples of these microstructures are on display in Figure 30. A statistical analysis of the stochasticity among the generated samples is presented in Figure 31. For more information regarding how these microstructures were generated, see Chapter 2.1.1.2.

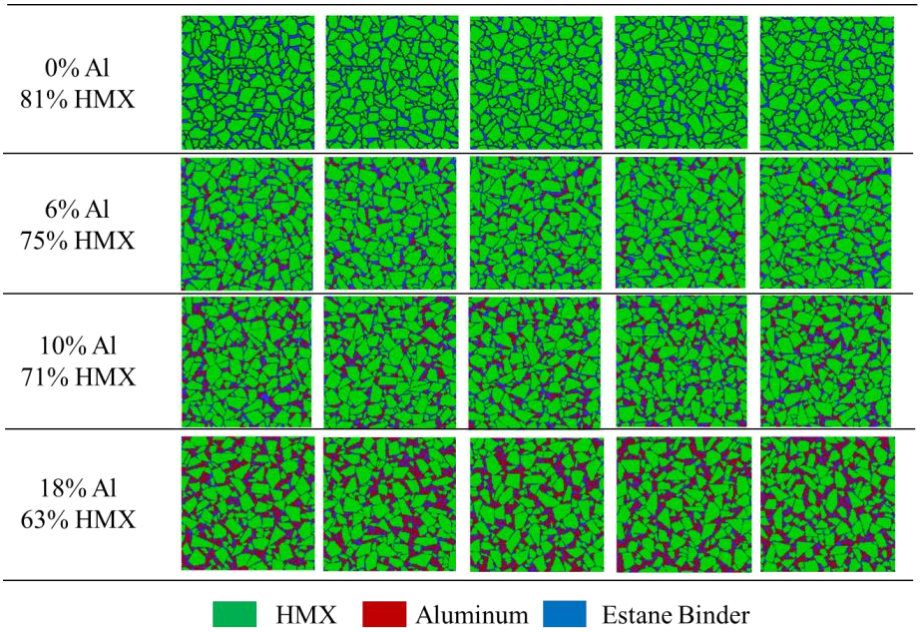

Figure 30 - Samples of computationally generated, statistically similar microstructures for four levels of aluminization: 0 % Al, 6 % Al, 10% Al, and 18% Al. Estane binder has a constant volume fraction of 19%.

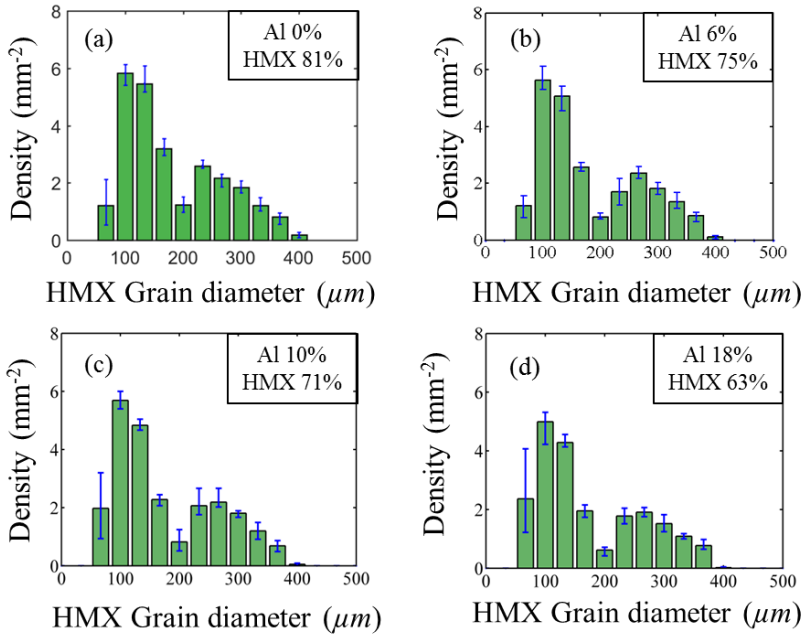

Figure 31 - Bimodal HMX grain distributions for the samples shown in Figure 30. The error bars indicate the maximum and minimum values among the samples in each set; (a) 0% Al; (b) 6% Al; (c) 10% Al; (d) 18% Al.

Experimental samples have inherently heterogeneous properties, including nano and micro scale voids, microcracks, and directionality of stiffness due to the anisotropic nature of the HMX crystal. The heterogeneities are phenomenologically accounted for by randomly varying the elastic modulus of the HMX grains. Both computational and experimental results have previously shown how microstructure heterogeneity and defects alter the effective elastic modulus of the grain. Yang et al. [126] performed MD simulations of a void in a copper plate, and demonstrated a negative correlation between the elastic modulus of the plate and the volume fraction of the void. Hudson et al. [128] found that grains with higher defects have a lower elastic modulus. Using the stiffness tensor provided by Sewell et al. [129], the minimum, maximum, and Voigt-Reuss-Hill average of the Young's modulus are calculated to be 12.9, 30.3, and 20.0 GPa respectively. Each HMX grain is randomly assigned one of these values. For simplicity, the aluminum particles are assumed to be homogeneous and isotropic. For the purposes of this study, no initial interfacial defects in the forms debonding between different constituents are considered.

4.2.2 Loading Configurations

The specimen is initially stress-free and at rest. Impact loading is effected by applying a short-duration velocity on the top boundary of the sample. The left and right boundaries are constrained such that lateral expansion does not occur. This is a 2D model and the conditions of plane-strain are applied. The pulse intensity (U_P) and duration (t_{pulse}) are chosen to represent the loading characteristics of given combinations of flyer velocity and thickness. For simplicity, a single imposed velocity is applied on the top of the sample for the specified pulse width (see Figure 32(a)). In real PBX microstructures, different

materials have varying impedances, which would lead to non-uniform velocities along the sample boundary from a single flyer. This discrepancy is assumed negligible when the flyer and the confinement materials are significantly harder than the PBX. The specific loading conditions used in the computational analysis are the particle velocities of $U_{\mathrm{p}} = 400, 500, 600, 800, 1000\,\mathrm{m/s}$ and the pulse duration of $t_{\mathrm{pulse}} = 40 - 640\,n\mathrm{s}$, as listed in Table 13. For each velocity, seven different pulse durations are applied to each sample, yielding 700 microstructure - loading combinations (5 velocities × 7 pulse durations × 4 aluminum concentrations × 5 samples). The shock pulse profile imparted onto the sample at the upper boundary is shown in Figure 32(b). The velocity increases from $0\,\mathrm{m/s}$ to U_{p} over the period of a 10 ns ramp time. This velocity is maintained until the downward ramp is reached at t_{ramp2}, after which the pulse velocity linearly decreases to zero over the course of 10 ns. After the final time, τ, the velocity constraint is removed. The side boundaries are constrained in the *x*-direction, while the bottom boundary is constrained in the *y*-direction. These three boundaries serve as frictionless walls during the simulation.

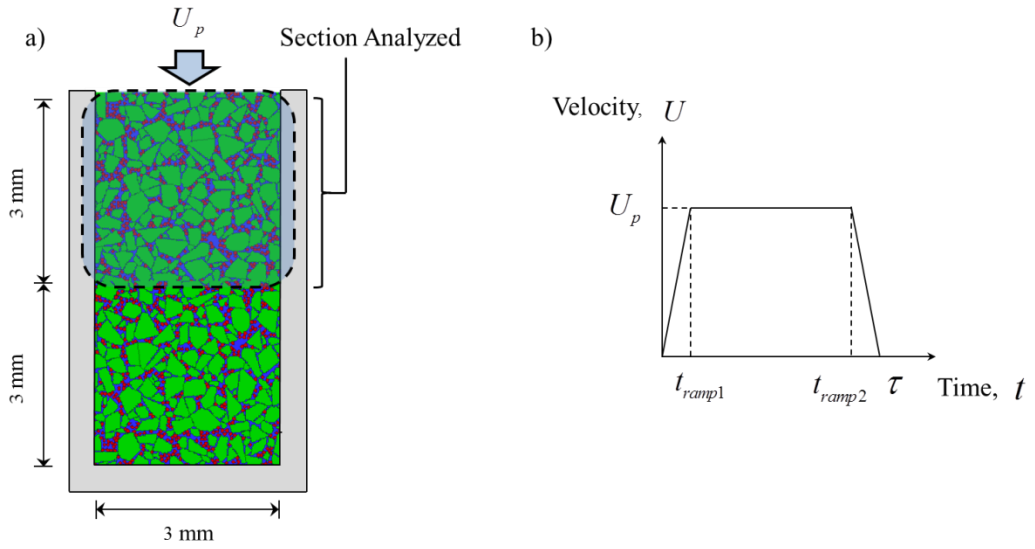

Figure 32 - (a) Loading configuration of an arbitrary microstructure sample with an imposed particle velocity of U_P at the upper end. Only the top half of the sample traversed by the downward stress wave is analyzed to avoid the effects of wave reflection. (b) Particle velocity profile imposed with a magnitude of U_P for a pulse duration of τ. In all cases, t_{ramp1} = 10 ns and t_{ramp2} = (τ -10 ns).

Table 13. APBX loading conditions

% Al / U_p	400 m/s	500 m/s	600 m/s	800 m/s	1000 m/s
0%, 6%, 10%, 18% Al	520 – 640 ns	220 - 340 ns	130 – 190 ns	50 – 110 ns	40 – 70 ns

4.2.3 Constitutive Relations

The computational analysis is performed using CODEX (Cohesive Dynamics for Explosives), a recently developed Lagrangian cohesive finite element code. This framework accounts for the dominant thermo-mechanical processes including constituent

elasto-vicoplasticity, viscoelasticity, bulk compressibility, fracture, interfacial debonding, internal contact, bulk and frictional heating, and heat conduction. The aluminum follows the same constitutive model as the HMX grains, and uses different material parameters. It is assumed HMX grains and the Al particles undergo elasto-viscoplastic deformations. A detailed description of the constitutive models used is in Ref. [19]. The viscoplastic relations take into account strain hardening as well as the strain rate dependence. Table 1 and Table 2 detail the material parameters used for the viscoplastic relation of HMX and aluminum respectively. The evolution of the hydrostatic part of the stress tensor is governed by a Birch-Murnaghan equation of state. The Estane binder follows a generalized Maxwell model with shear modulus varying based on relaxation as described by a Prony series formulation. Further details on the constitutive models used in this chapter, including the parameters and calibration techniques used in this simulation, can be found in Chapter 2.

4.2.4 Cohesive Element Framework

The fracture of the microstructure under high-impact loading is modeled using a cohesive finite element framework. The fracture follows a bilinear traction separation law illustrated in Figure 33. These cohesive elements allow for arbitrary crack initiation and propagation, while also giving CODEX the ability to explicitly model initial debonding between grains and binder, commonly observed in experimental samples. The effect of initial debonding on ignition sensitivity is outside the scope of this thesis and may serve as the subject of future work for aluminized PBX samples. Such studies were previously carried out for PBX without aluminum [20, 101]. Further details on this cohesive model

can be found Chapter 2.2.3 and the parameters for the cohesive model between each material combination (HMX-HMX, HMX-Al, HMX-Estane, Al-Estane, Al-Al, and Estane-Estane) are listed in Table 3 in Chapter 2. The determination of the cohesive parameters for the binder-HMX, aluminum-binder, and aluminum-HMX interfaces follow that in Ref. [112]. In particular, the cohesive parameters for the aluminum-binder interfaces are determined based on experimental data in Ref. [158]. It is understood that there is an oxidized layer with a thickness on the order of a few nanometers on the surface of the aluminum particles. The cohesive parameters used here account for the effects of this layer since the experimental samples themselves contained such a layer on the surface of the aluminum.

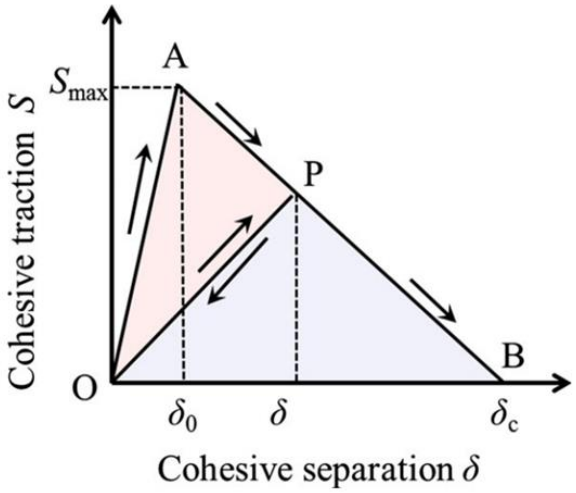

Figure 33 - Bilinear traction-separation law for potential cracks.

4.2.5 Hotspot Characterization

An ignition criterion developed by Barua et al. [96] is used in this study to provide a standard for determination of hotspot criticality. This model is described in full in Chapter 2.2.5, and only a brief summary will be given here.

The ignition criterion assumes that a hotspot reaches criticality if its rate of heat generation by means of chemical decomposition exceeds the rate of heat lost to its surrounds, primarily through conduction. For this to occur, a certain amount of thermal energy is required to overcome the activation energy of the chemical decomposition. When a hotspot reaches a certain temperature, there is a minimum diameter it must have in order to obtain the necessary energy. If any part of the hotspot exceed this critical diameter, d_c, during the simulation, the hotspot is treated as a critical hotspot. This condition is represented by Eq. (33).

$$d(T) \geq d_c(T), \tag{33}$$

If two or more hotspots in a 3 mm^2 domain reach criticality, the entire sample is assumed to proceed to ignition. This hotspot density threshold for ignition (0.22 mm^2) was chosen based on the work of Barua et al., and further information can be found in Ref. [96].

4.3 Results and Discussion

A systematic quantification of the ignition of aluminized PBX is carried out, focusing on the shock intensity and shock pulse duration. Five samples of each aluminum concentration are tested at various loading intensities and pulse durations in order to

determine the 50% ignition threshold. This threshold is modeled using a modified James relation in addition to a modified Walker-Wasley relation, and a probability spectrum is quantified by introducing the James number, *J*, first proposed by Gresshoff and Hrousis [106] and Walker Wasley number, *W*, first proposed by Kim et al [20]. The physical mechanisms responsible for the decreased sensitivity to ignition in samples with higher aluminum concentrations are delineated in section 4.3.3.

4.3.1 Ignition Sensitivity Threshold

The ignition threshold of PBX is fit using two models, the modified Hugh James relation (as first introduced in Chapter 3) and the modified Walker-Wasley relation. Each model provides a different way of understanding the ignition sensitivity of energetic materials using different loading parameters. It is possible to derive an equivalent James relation from the Walker-Wasley relation. This derivation can be found in the appendix A.

4.3.1.1 Hugh James Ignition Threshold

The critical energy threshold is analyzed using the hotspot ignition criterion described in Section 4.2.5. Figure 34 shows the minimum energy required for ignition from five samples subjected to various shock intensities. The shock intensities are represented in a power flux form, Π, which is calculated as

$$\Pi = PU_p, \tag{34}$$

where P is the average hydrostatic part of the stress tensor at the impact face, and U_p is the particle velocity at the impact face. The energy fluence, $E = \int_0^t \Pi \, dt$, represents the total energy transferred to the material by the shock loading per unit area of the impact face. For each loading velocity tested, the power flux is found to be nearly constant, while each successive test was carried out with an incrementally higher energy fluence, which is analogous to impacting the samples with increasingly thicker flyers at the same velocity. The red circles in Figure 34 represent samples that did not achieve criticality, and the black crosses represent samples that did reach criticality. The 50% ignition probability data points were calculated by averaging the energy fluences required for two and three samples to reach criticality for a given power flux.

Due to the stochastic nature of the random microstructures, each sample requires a different amount of minimum energy to ignite. A common way to model the probabilistic nature of the ignition behavior is to consider the 50% ignition threshold. Take the James relation [54], which is based on a minimum critical energy required for ignition, as example first here. Gresshoff and Hrousis [106] expanded on the James relation by introducing a James number, *J*, which allows for extrapolation of the ignition probability above and below the 50% threshold. The form of the modified James relation is

$$\frac{1}{J} = \frac{E_c}{E} + \frac{\Pi_c}{\Pi}, \tag{35}$$

where E_c and Π_c are fitting parameters which represent asymptotic thresholds for the critical energy and the critical power flux, respectively. This relation originates from the

James relation [54], but uses the power flux ($\Pi = PU_P$) introduced by Welle et al. [13] to replace the specific kinetic energy ($\sum = 0.5U_P^2$). By definition, the threshold where 50% of the samples ignite (i.e. 50% probability of ignition) occurs when $J = 1$. Any combination of power flux and energy fluence above the threshold ($J > 1$) would lead to a greater than 50% probability of ignition. Similarly, any combination of power flux and energy fluence below the threshold ($J < 1$) would lead to a probability ignition less than 50%. A similar probabilistic quantification can be carried out using the modified Walker-Wasley relation in the pressure-loading pulse duration (P-τ) space [53], as discussed later.

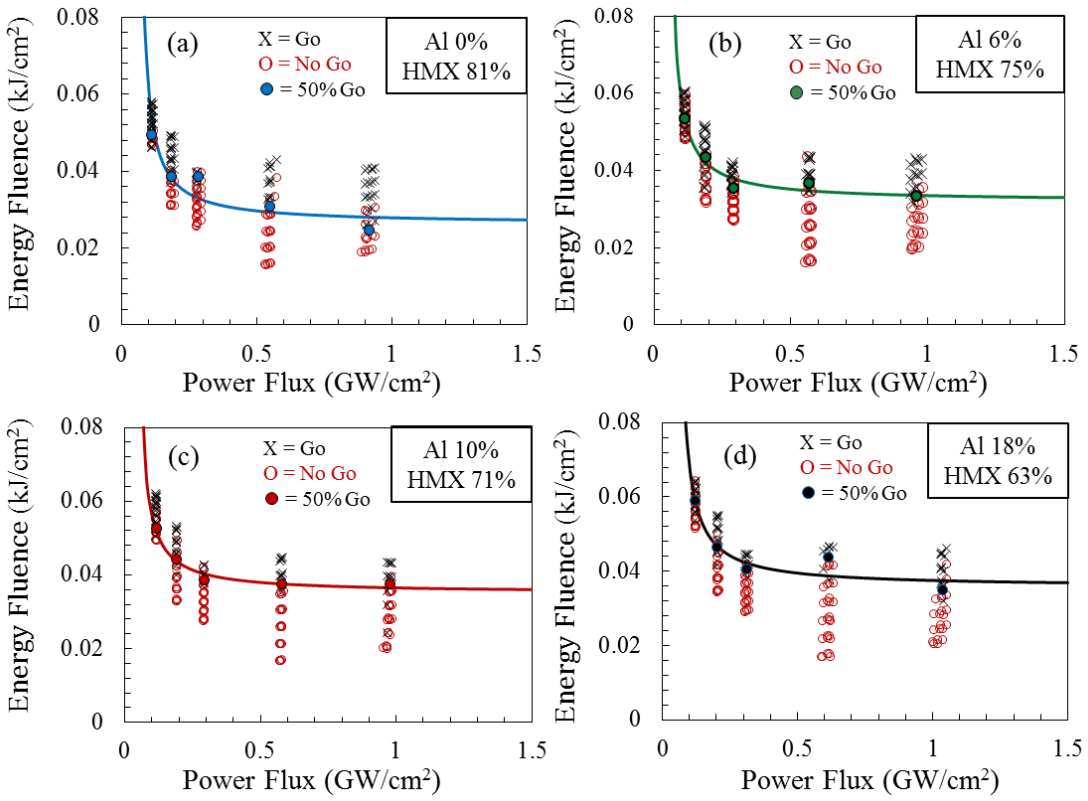

Figure 34 - Go/no go results of individual samples of APBX with different levels of aluminum: (a) 0% Al; (b) 6% Al; (c) 10% Al; (d) 18% Al.

The 50% ignition thresholds for all aluminum concentrations (0%, 6%, 10%, and 18% aluminum by volume) are shown in Figure 35, and the corresponding parameters for the modified James relation are listed in Table 14. For any given microstructure, a higher loading rate (power flux) corresponds to a lower energy fluence for ignition. As the aluminum concentration increases, the energy fluence required for 50% of the samples to reach criticality also increases, demonstrating that adding aluminum reduces the overall sensitivity of the PBX to ignition. This trend matches the experimental observations of the relative sensitivity of aluminized PBX as compared to non-aluminized PBX of Prakash et al., who measured the relative sensitivities using the standard fall hammer method [156]. Figure 35 presents a clear trend of increasing critical energy fluence as the volume fraction

of aluminum increases, however the trend in the power flux parameter is not monotonous. This is explained by the relatively fewer 50% ignition sensitivity data points available to fit the vertical asymptote at lower impact velocities, as calculations at a lower piston velocities require extremely long computation times.

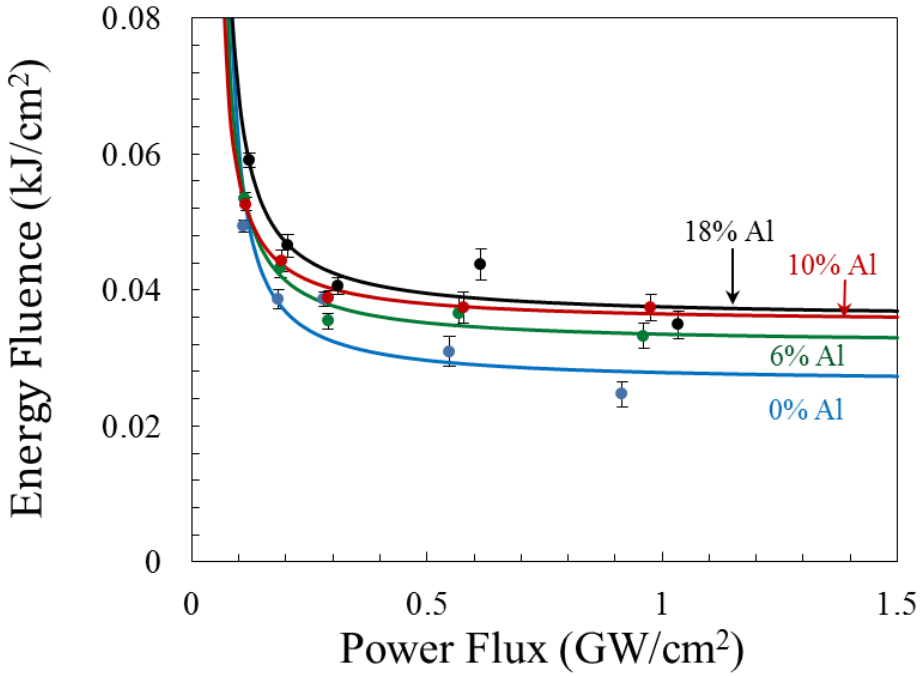

Figure 35 - 50% ignition thresholds of APBX with different levels (0%, 6%, 10%, 18%) of aluminization analyzed in the James space.

Table 14. Modified James Parameter values from Figure 35

Aluminum Volume Fraction	E_c (kJ/cm^2)	Π_c (GW/cm^2)
0% Al	0.0263	0.0570
6% Al	0.0320	0.0452
10% Al	0.0351	0.0376
18% Al	0.0357	0.0479

The ignition sensitivities are easily distinguished at high power fluxes, and relatively indistinguishable at lower power fluxes. As the aluminum concentration increases the variation in energy fluence required for ignition decreases, which may imply there is an optimal volume fraction of aluminum that corresponds to a minimized sensitivity for ignition while maximizing power output. Various experiments testing TNT/HMX/RDX based PBXs have suggested a 15-20% volume fraction of aluminum as an optimal amount to maximize explosive power due to Al increasing the heat of explosion while decreasing the volume of gaseous products [56].

4.3.1.2 Walker-Wasley Ignition Threshold

An alternative method of mapping the ignition threshold uses the Walker-Wasley relation [53]. First proposed in 1969, the Walker-Wasley relation uses a power law fitting to relate the average hydrostatic part of the input stress (P) and pulse duration (τ) required to reach ignition. A modified form of this relation is

$$\frac{P^n \tau}{C} = W, \tag{36}$$

where C is a material-dependent parameter and the exponential fitting parameter, n, is often set to the value of 2. This relationship provides a non-dimensional Walker-Wasley number, W, which relates to the probability of ignition. Similar to the J parameter in Eq. (35), $W=1$ represents the threshold where 50% of the samples reach ignition. $W>1$ and $W<1$ correspond to ignition probabilities greater than 50% and less than 50%, respectively.

The aluminized PBX initiation data is fit to the Walker-Wasley relation (Eq. (36)) in the P-τ space and the result is shown in Figure 36. The corresponding parameters used are listed in Table 15. As the volume fraction of aluminum increases, material-dependent parameter C also increases, indicating a lower sensitivity to ignition under similar loading conditions. At lower load intensities, the Walker-Wasley fits, when ploted on the log-log scale, do not distinguish the cases for different aluminum levels as well as the Hugh James relation.

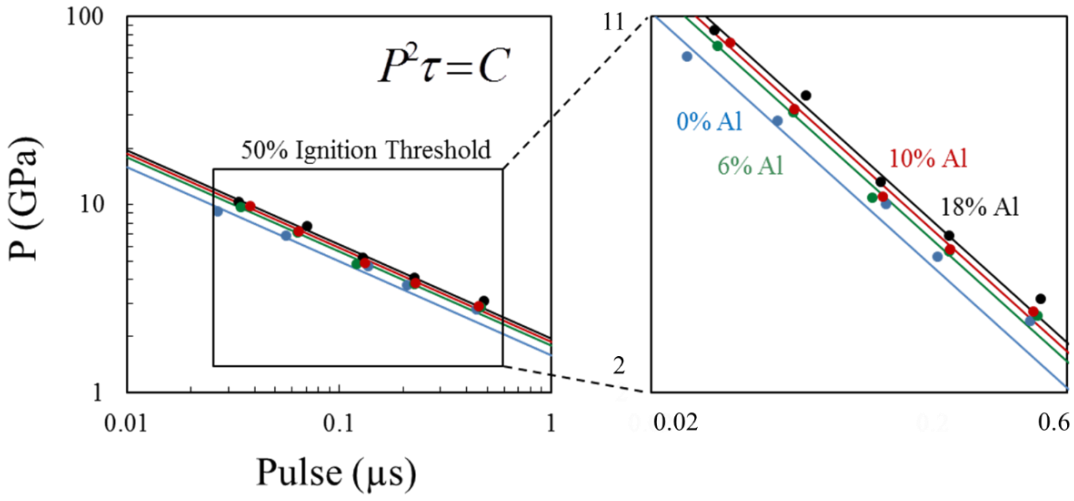

Figure 36 - 50% ignition thresholds of APBX with different levels (0%, 6%, 10%, 18%) of aluminization analyzed in the Walker-Wasley space.

Table 15. Walker-Wasley Parameter values from Figure 36

Aluminum Volume Fraction	*C*	*W*
0% Al	2.507	1
6% Al	3.187	1
10% Al	3.489	1
18% Al	3.781	1

4.3.2 Ignition Probability Mapping

For the 50% ignition probability analysis above, *J* is taken to be 1 in the Hugh James space and Eq. (35), with the understanding that if *J* is greater than or less than 1, the corresponding probability of ignition is greater than or less than 50%, respectively. The probability of ignition as a function of *J* is shown in Figure 37(a). By the same token, using the Walker-Wasley framework, the results of the ignition probability as a function of *W* is shown in Figure 37(b).

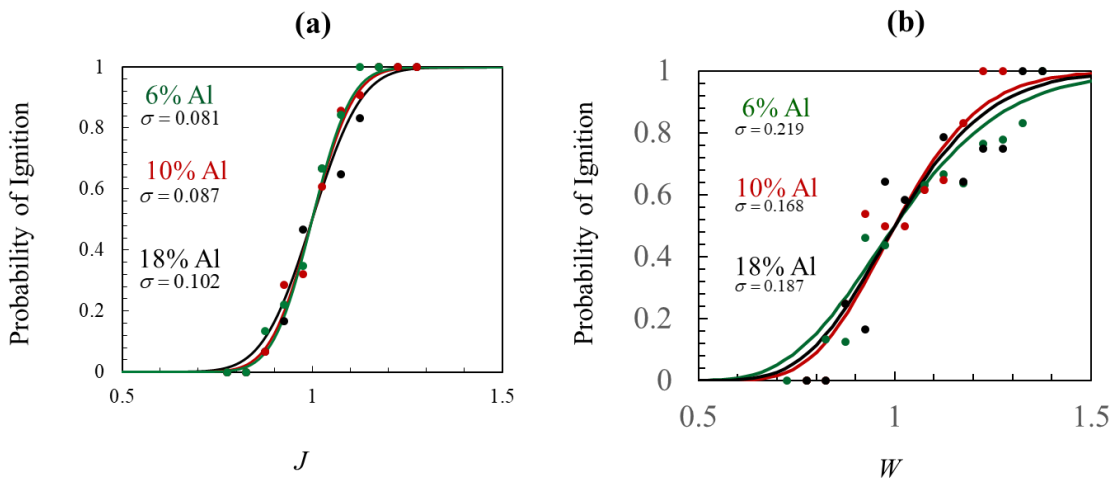

Figure 37 - Ignition probability as a function of *J* (a) and *W* (b) for APBX with different levels of aluminization, shown in terms of the cumulative distribution function (CDF) of the Gaussian distribution.

The relationship between the probability of ignition and J is fit using a cumulative Gaussian distribution, with a mean value of $J = 1$. The standard deviations σ = 0.081, 0.087, and 0.102 for sample sets with 6%, 10%, and 18% of aluminum, respectively. Written in terms of the loading parameters in the James space, the ignition probability is

$$\mathcal{P}(E,\Pi) = \frac{1}{2} + \frac{1}{2}\,\mathrm{erf}\left[\frac{1}{\sqrt{2}\sigma}\left(\frac{E\Pi}{E_c\Pi + \Pi_c E} - 1\right)\right], \tag{37}$$

where erf (·) is the error function. In the Walker-Wasley space, the probability of ignition as a function of W with a mean of $W = 1$ has the standard deviation of σ = 0.219, 0.168, 0.187 for microstructures with 6%, 10%, and 18% of aluminum, respectively. Written in terms of shock pressure, P, and pulse duration, τ, the probability of ignition has the form

$$\mathcal{P}(P,\tau) = \frac{1}{2} + \frac{1}{2}\,\mathrm{erf}\left[\frac{1}{\sqrt{2}\sigma}\left(\ln\left(P^2\tau\right) - \ln C\right)\right], \tag{38}$$

Figure 38 and Figure 39 provide the probability of ignition as functions of loading in the entire loading condition spectra in the James and Walker-Wasley spaces, respectively. In each figure, the black line corresponds to all possible combinations of loading conditions where 50% of samples reach ignition. The upper and lower red dashed lines represent, respectively, the loading conditions for which 90% and 10% of samples reach ignition.

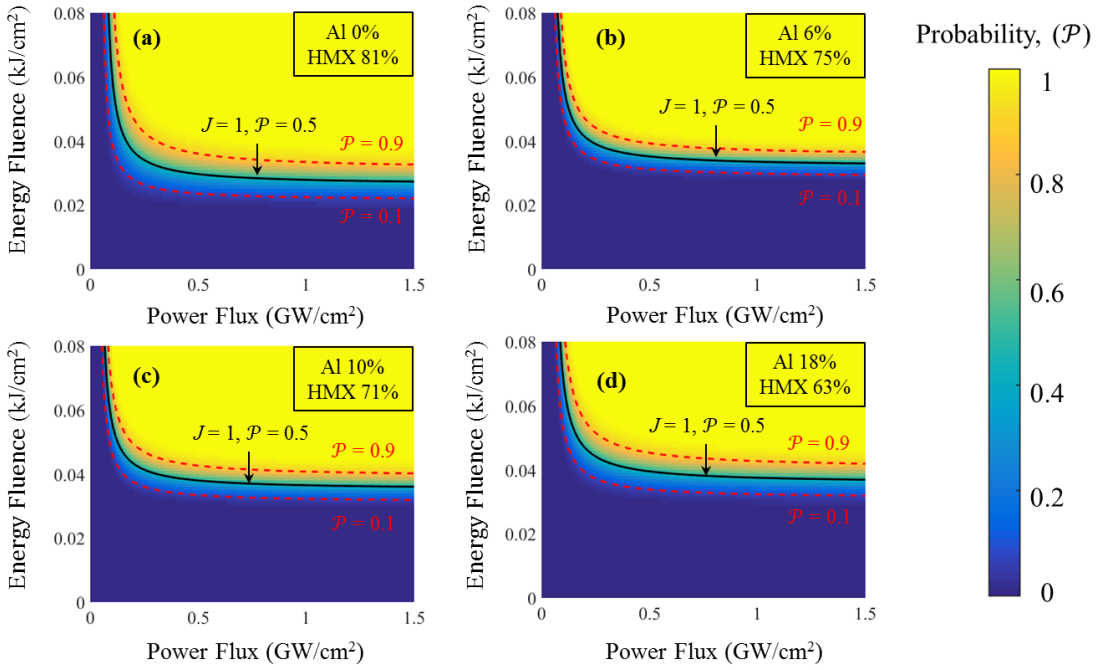

Figure 38 - Ignition probability distribution maps for the four levels of aluminization analyzed; (a) 0% Al; (b) 6% Al; (c) 10% Al; (d) 18% Al in the energy fluence - power flux (E-Π) space.

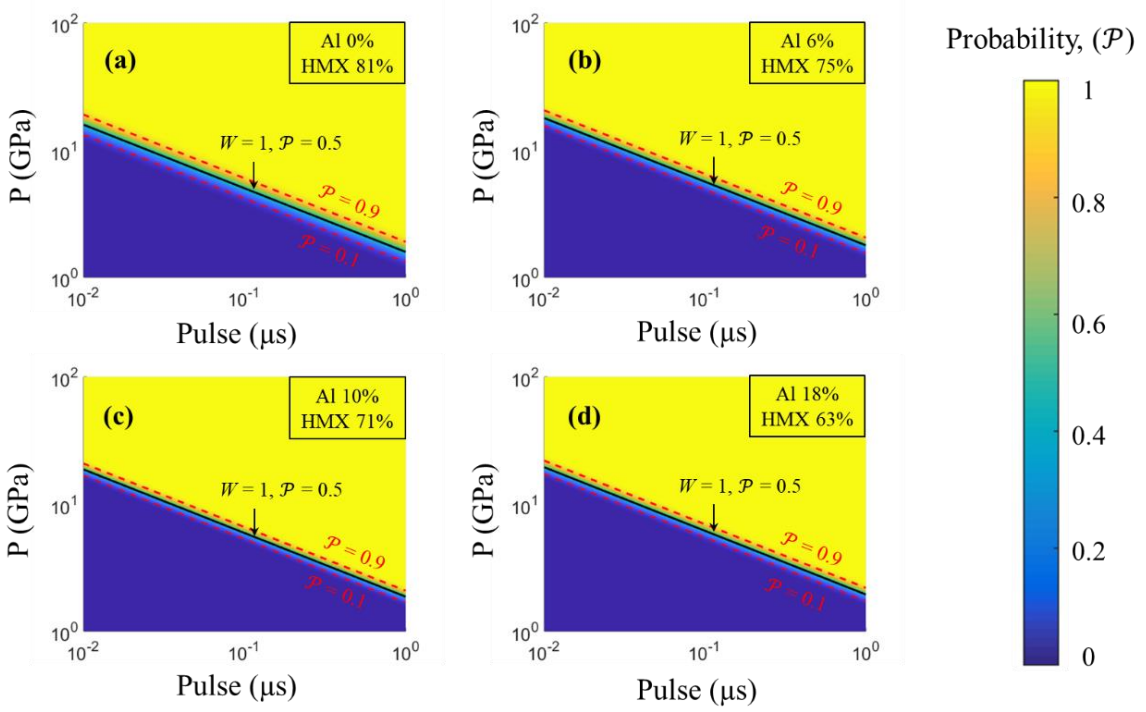

Figure 39 - Ignition probability distribution maps for the four levels of aluminization analyzed; (a) 0% Al; (b) 6% Al; (c) 10% Al; (d) 18% Al in the pressure - pulse duration $(P-\tau)$ space.

The reason that the standard deviations of ignition probability in Figure 37 for the different levels of aluminization are similar to each other is that the degree of microsctructure variations among the samples in the sets relative to their respective averages are similar. This can be partly seen from the similar standard deviations of grain size distributions of the samples in Figure 31. The effect of aluminization on ignition probability is primarily on the 50% ignition thresholds, as shown in Figure 35, Figure 36, Figure 38, and Figure 39. On the other hand, the probability spread relative to the 50% thresholds is a reflection of how different the samples in each material set are from each other. Indeed, the fact that samples of each material behave somewhat differently (statistical variations) because of inherent materials heterogeneities, and the probabilistic analyses here using J and W

captures these effects. To simply put, if all samples in a material set were identical to each other (no material hetergenity, which is impossible), there wouldn't be statistical variation in behavior.

It is likely that the standard deviations of the J-$\mathcal{P}$ and W-$\mathcal{P}$ relations obtained here are smaller than what would be seen in experiments. Although the samples used in this study are statistically similar, variability among experimental samples cannot be controlled as rigidly. In addition, there are additional sources of variation in real experimental samples not explicitly modeled computationally. Specifically microstructure voids, which are known to play a significant role in the generation of hotspots, are not explicitly modeled in this chapter. For more information on the effect of voids, see Chapters 5 and 6. Other factors can also contribute to measured property variations in experiments, including loading uncertainties and instrument error.

The correlation between the aluminum concentration and the modified James parameters, E_c and Π_c, as well as the modified Walker Wasley parameter, C, are shown below in Figure 40. The data is fit to a simple linear model to outline the trend, with α being the concentration of aluminum. The resulting material parameters are listed in Table 16. It can be seen that increasing from 10% to 18% volume fraction of aluminum has less effect on sensitivity than the increase from 0% to 6%. This coincides with the observation of optimum PBX performance (as measured by the velocity of detonation or heat of explosion) [56]. This coincidence of optimum effects on the ignition threshold studied here and performance in general may be a just coincidence, or there may be an intrinsic link. In this chapter, only the ignition sensitivity, as measured by the minimum amount of energy

required to cause ignition at a given energy input rate (the James threshold), is analyzed. To draw comparisons to overall explosive performance, analysis of the process beyond the point of critical hotspot initiation into detonation is required.

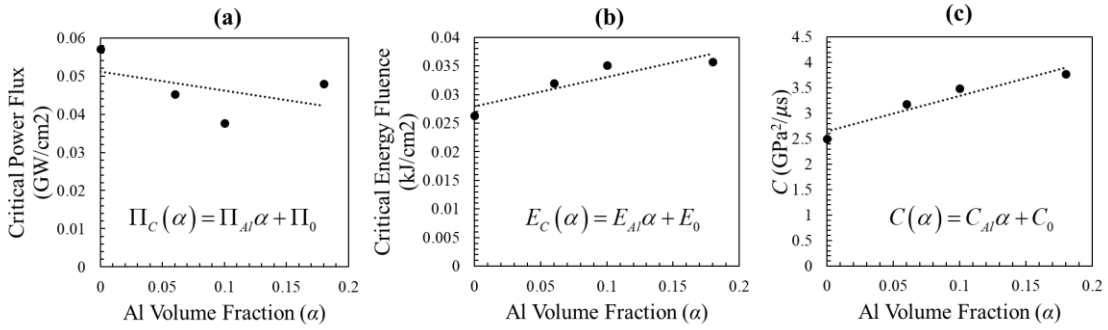

Figure 40 - Correlation between aluminum volume fraction and (a) critical power flux, (b) critical energy fluence, and (c) material-dependent parameter *C*.

Table 16. Material Properties for the linear relationships shown in Figure 40

Material Properties	$\Pi\left(\frac{GW}{cm^2}\right)$	$E\left(\frac{kJ}{cm^2}\right)$	$C\left(\frac{GPa^2}{\mu s}\right)$
Slope	$\Pi_{Al} = -0.050$	$E_{Al} = 0.052$	$C_{Al} = 6.95$
Intercept	$\Pi_0 = 0.051$	$E_0 = 0.028$	$C_0 = 2.65$

By combining the relations above with the probability functions in Eqs. (37) and (38), we can write the probability of ignition directly as a function of the aluminum concentration, α, as well as the loading conditions as

$$\mathcal{P}(\alpha, E, \Pi) = \frac{1}{2} + \frac{1}{2}\,\mathrm{erf}\left[\frac{1}{\sqrt{2}\sigma}\left(\frac{E\Pi}{\Pi\left(E_{Al}\alpha + E_0\right) + E\left(\Pi_{Al}\alpha + \Pi_0\right)} - 1\right)\right], \text{ and} \qquad (39)$$

$$\mathcal{P}(\alpha, P, \tau) = \frac{1}{2} + \frac{1}{2}\operatorname{erf}\left[\frac{1}{\sqrt{2}\sigma}\left(\ln\left(P^2\tau\right) - \ln\left(C_{Al}\alpha + C_0\right)\right)\right]. \quad (40)$$

Conversely, the ignition thresholds as functions of the aluminum concentration are

$$\frac{1}{J} = \frac{E_{Al}\alpha + E_0}{E} + \frac{\Pi_{Al}\alpha + \Pi_{0c}}{\Pi}, \text{ and} \quad (41)$$

$$\frac{P^2\tau}{C_{Al}\alpha + C_0} = W. \quad (42)$$

4.3.3 Effect of Aluminum on Hotspot Criticality

The physics governing the effect of aluminum incorporated into PBX are outlined in this section. Section 4.3.3.1 discusses the predominant mechanisms of heat generation, and how they are influenced by the inclusion of aluminum. Section 4.3.3.2 discusses the resulting effect of increasing the diameter of the aluminum particles from 50 μm to 100 μm.

4.3.3.1 Heat Generation in Aluminized Samples

In this analysis, three forms of heat generation due to energy dissipation are accounted for: frictional heating, plastic work in the HMX grains, and viscous dissipation in the binder. The relative effects of frictional work and plastic work in the HMX grains are analyzed in Figure 41. The heat generation from the viscoelastic dissipation in the binder is not analyzed here since its contribution to heating is mostly in the Estane matrix and the effect of heat transfer via conduction is minimal in the examined time scale. Additionally, it is found that shock heating is essentially negligible under the conditons of

the pulse loading considered, primarily due to the fact that decompression occurs quickly. Specifically, calculations show that shock heating raises the residual temperature (after decompression) by less than 1 K in most grains. This is in contrast to what happens under monotonic loading at high flyer velocities. It is important to study the effects of localized heat generation, rather than total heat generation, since hotspots only initialize from localized heating.

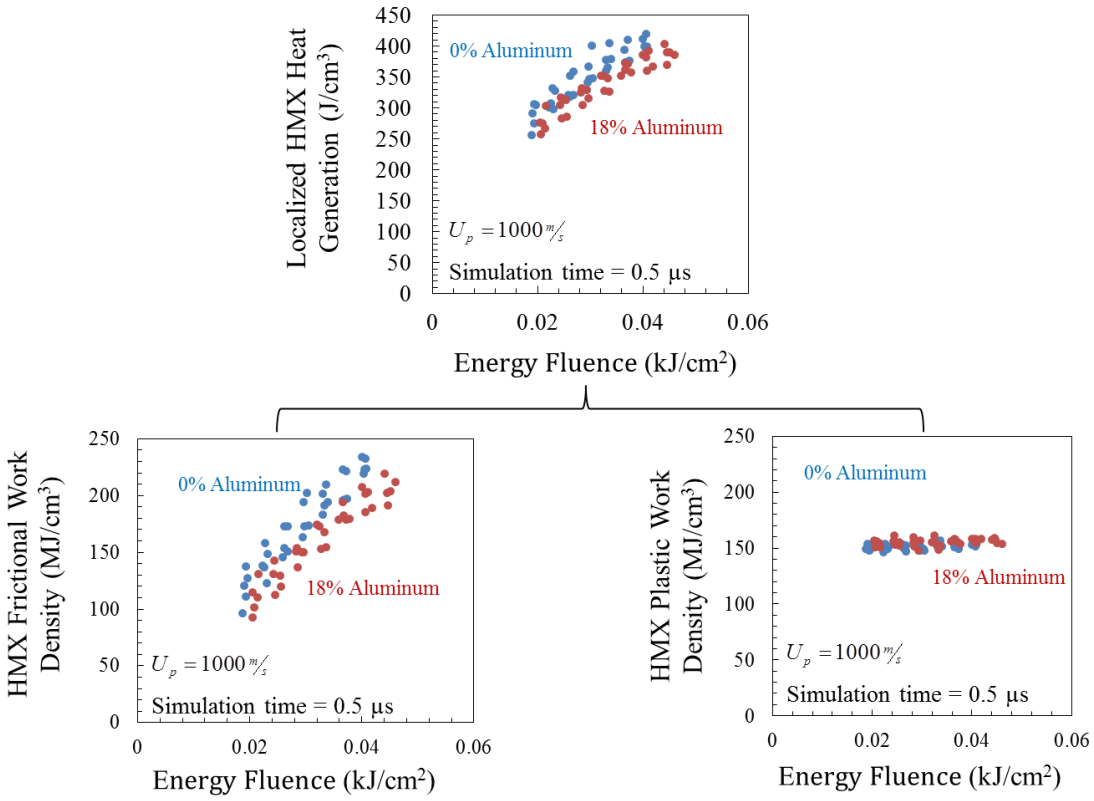

Figure 41 - Breakdown of heat generation in HMX grains due to frictional work and plastic work.

As seen in Figure 41, there is a greater amount of localized heat generation in HMX grains in samples with no aluminum as compared to samples with 18% aluminum (by volume). This difference is a direct result of the increased levels of frictional work

occurring in the HMX when no aluminum is present. The plastic work density and resultant heat generation from it remains relatively constant between samples regardless of the total energy fluence.

The crack density for three aluminum levels is shown in Figure 42 for U_p = 1000 m/s. This high piston velocity is chosen because the largest difference in ignition thresholds occurs at higher power flux values. The data for 6% Al is not shown to keep the plot less cluttered and easier to visualize. As the amount of aluminum is increased, the total amount of cracking remains nearly constant (Figure 42(a)), but the number of cracks associated with HMX decreases (Figure 42(b)). More cracks are forming between the aluminum and the binder or between the HMX and the binder, instead of in the HMX grains in the form of intergranular cracks. Since the main source of localized heat generation is frictional dissipation stemming from fracture and subsequent material interfacial movement, this means part of the heat generation in the material is moving away from HMX, and towards the Al particles instead. This phenomenon is examined more thoroughly in section 4.3.3.2.

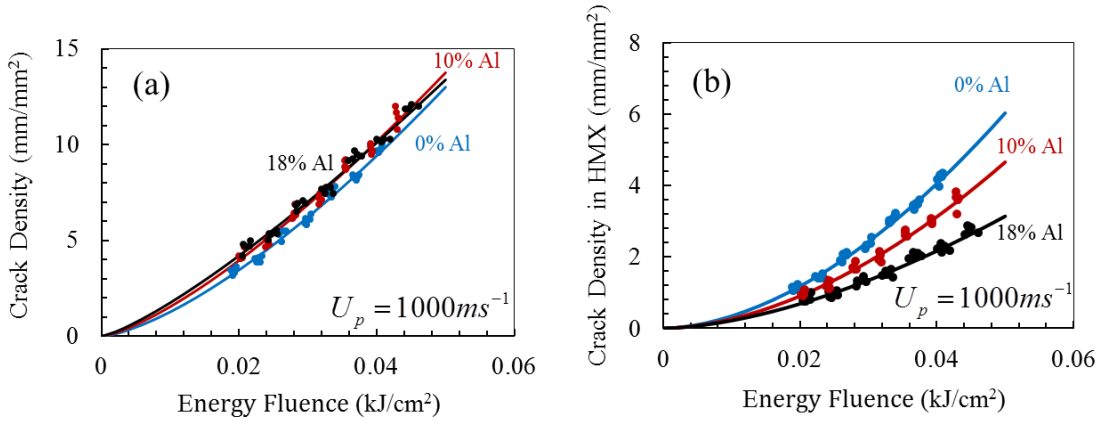

Figure 42 - Effect of Al volume fraction on crack density in relation to the imparted energy fluence when the particle velocity is 1000 m/s; (a) total crack density; (b) density of cracks associated with HMX. The crack density in (b) has been normalized to the volume fraction of the HMX.

4.3.3.2 Aluminum Particle Size Effect on Initiation

In addition to the above analysis with d = 50 µm, the analysis is repeated using a larger aluminum particle diameter of d = 100 µm. In both cases, the aluminum volume fraction is constant at 10%. The results are shown in Figure 43, with the corresponding James equation parameters listed in Table 17. Figure 44 shows the corresponding probability variation as J varies.

Table 17. Modified James Parameter values from Figure 43

Aluminum Diameter	E_c (kJ/cm²)	Π_c (GW/cm²)
50 µm	0.0351	0.0376
100 µm	0.0320	0.0306

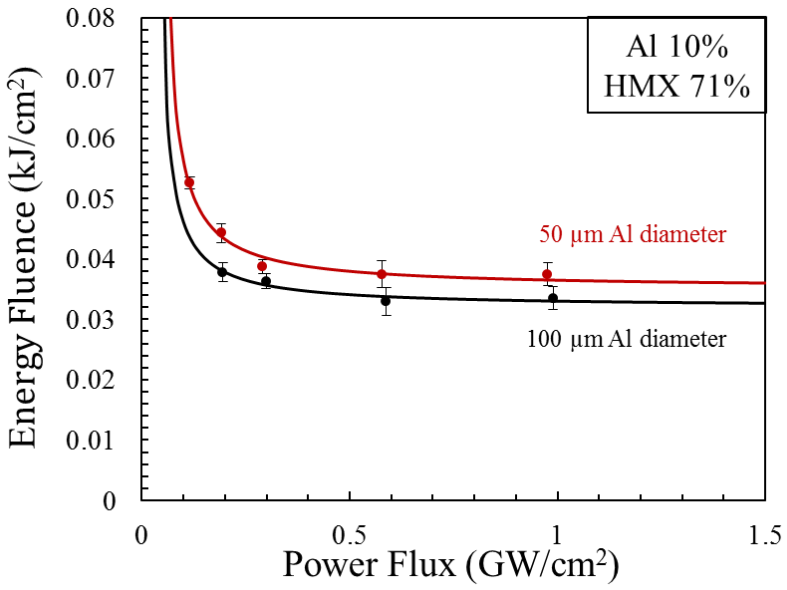

Figure 43 - ignition thresholds of 10% Al samples with 50 µm and 100 µm diameter aluminum particles.

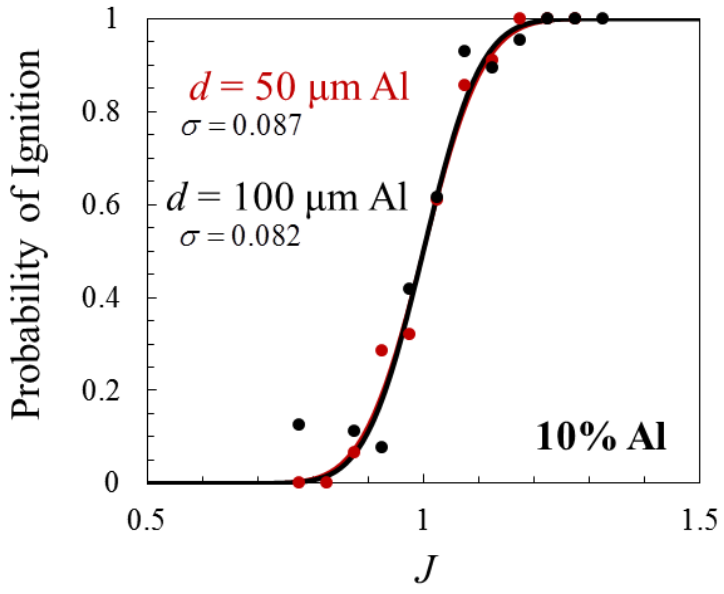

Figure 44 - Cumulative ignition probability as a function of *J* for APBX with 50 and 100 µm aluminum particles. In both cases, the aluminum volume fraction is 10%.

The larger particle diameter lowers the ignition threshold and increases the ignition sensitivity. Over the entire range of input power flux analyzed ($0.2 – 1$ GW/cm^2), the larger aluminum particle diameter consistently corresponds to lower energy fluence for the 50% ignition threshold. This is qualitatively consistent with experimental observations recorded by Gogulya et al. [159] showing that the detonation velocities of HMX based explosives decreased as aluminum particle size decreased (while the mass fraction of aluminum particles was held constant at 15%). As shown in Figure 44, the variation of the ignition threshold as J varies is essentially the same for the two aluminum particle sizes. As is the case for different aluminum concentrations (volume fractions) discussed earlier, Figure 44 does not imply that the ignition sensitivity thresholds for the two Al particle sizes are the same, but rather that the probability variations relative to the corresponding 50% thresholds essentially coincide.

First, as discussed in section 4.3.3.1, interfacial friction plays a more dominant role in heat generation than bulk inelastic deformation. Any fracture energy spent on crack propagation between the aluminum and binder is less energy available to the HMX grains, where the development of hotspots is key to ignition. Therefore, an increased amount of fracture on the aluminum surfaces results in desensitization. When comparing the crack density associated with aluminum particles (for both the 50 μm and 100 μm cases), over 98% of the cracks associated with aluminum are surface cracks. This implies that the total aluminum surface area has a more significant effect on sensitivity than aluminum concentration or volume fraction. Note also that smaller particles have higher surface-to-volume ratios, therefore, for the same volume fraction of aluminum the materials with smaller particles have more overall aluminum surfaces. Figure 45(a) shows how the

aluminum surface crack density compares between the 10% aluminum cases with large and small aluminum particle diameters. It is important to remember that no initial debonding exists in any sample. The crack density is significantly higher for the smaller particle cases, due to higher total surface area. When the total Al cracking is normalized to the total amount of Al surface area (Figure 45 (b)), the Al particle size becomes irrelevant. This evidence supports the claim that Al surface area plays a dominant role in ignition sensitivity.

The second reason why smaller aluminum particles lead to lower sensitivity to ignition is because a greater number of smaller particulates can be more spread out throughout the microstructure than fewer, larger ones. This allows for a more even dissipation of energy via aluminum debonding, which lowers the total potential energy available to the HMX phase. Since the aluminum particles are scattered randomly throughout the microstructure, decreasing their size while simultaneously increasing their quantity (to maintain the 10% Al volume fraction), increases the likelihood of an aluminum particle ending up near a potential hotspot location. The aluminum debonding can then function as an energy “sink”, preventing critical temperature rise in the nearby HMX.

It is important to note that this study is only focused on the mechanical effects that lead to hotspot formation, with aluminum particles in the micron scale. It is likely that smaller aluminum particles play a larger role in detonation when chemistry is considered, especially when dealing with Al particles in the nanoscale regime, but that is outside the scope of this chapter.

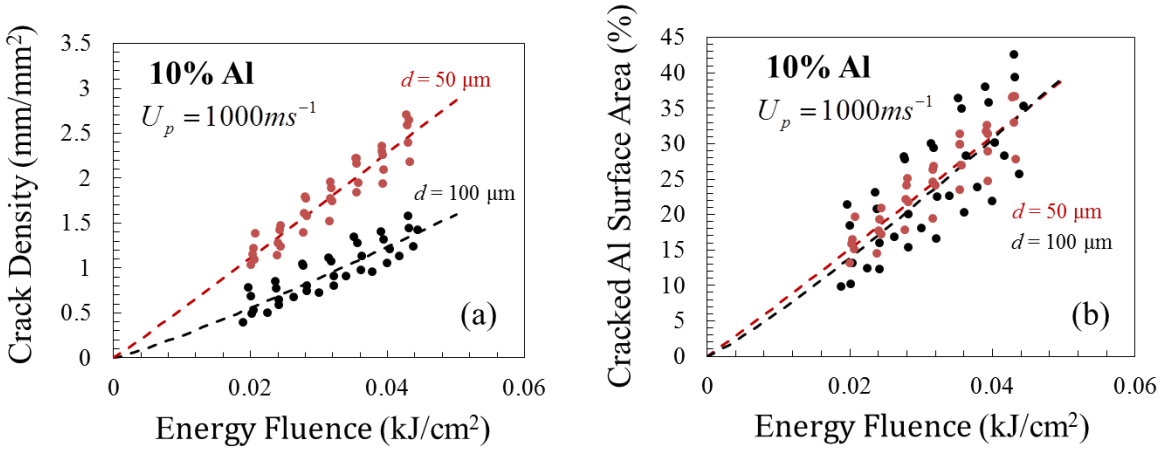

Figure 45 - (a) Surface crack density as a function of energy fluence in 10% Al samples with 50 µm and 100 µm diameter aluminum particles. (b) Percentage of total aluminum surface area that has fractured.

4.3.4 Experimental Validation

So far in the open literature, there is no direct experimental measurement of the quantities predicted here. As a result, direct comparison with experiments is not possible at this time. However, general trends seen in experiments concerning the ignition and detonation of aluminized PBX are consistent with the trends reported in this chapter, as stated in the discussions above. When studying HMX samples mixed with Al and ammonium perchlorate (AP), Li et al. [160] noticed that ignition sensitivity decreased with the addition of aluminum, and concluded, "…a plentiful [amount] of Al decentralizes the impact stress on explosive, accordingly diminishes the probability of hot-spots formation. Simultaneously, a vast [amount] of Al can improve heat transmit which hamper explosion propagation from hot-spots". A number of studies report decreasing detonation velocities as the aluminum volume fraction increases. Gogulya et al. [59, 161] found that the

detonation velocity decreased as the size of the aluminum particles decreased, while the volume fraction was held constant. It should be noted that nano-size aluminum particles may also significantly alter the detonation phase, which this study does not directly simulate. It is hoped that more direct experimental measurement concerning ignition thresholds will become available in the future.

4.4 Conclusion

The ignition behavior of APBX with microstructures containing 6%, 10%, and 18% Al by volume is analyzed and compared to that of the corresponding unaluminized PBX. The 50% ignition threshold for each Al concentration are mapped as a function of the power flux and energy fluence which are measures for loading condition. A probabilistic map is created to quantify the likelihood of ignition of the materials. The results show that, relative to the unaluminized PBX, the addition of aluminum reduces the 50% ignition threshold sensitivity by 21.7%, 33.5%, and 35.7% for APBXs with 6%, 10%, and 18% Al, respectively. In terms of the mechanisms responsible for the trend, the frictional dissipation between sliding crack surfaces plays a much more significant role in the development of critical hotspots than plastic deformation. At higher load intensities, the addition of aluminum does not significantly change the total amount of cracking in the materials, but it does encourage crack initiation in locations away from HMX, resulting in lower ignition sensitivity of the materials. The reason is that more energy is dissipated in the debonding of aluminum due to the lower cohesive strength between the Al particles and Estane binder, causing less localized heating in HMX. As the aluminum particle size is increased, the materials are more likely to generate critical hotspots for the same reason. Since larger Al

particles result in less total Al surface area (as compared to an equal volume of smaller Al particles), less energy is required to debond a majority of the Al particles, allowing more cracks to form in HMX grains, leading to higher ignition sensitivity.

Finally, it is useful to point out that the goal of this chapter is to illustrate the important micromechanical effects aluminum constituents have on the ignition sensitivity of PBXs. Through a thorough computational analysis, friction is identified as playing a dominant role in hotspot generation. These findings can help guide the direction of future experiments to focus on studying the importance of frictional heat dissipation under shock loading and efforts to modify the ignition sensitivity through material synthesis. A possible mechanism is to enhance the bonding strengths between different binders and constituents via design of the microstructure and change of synthesis routes.

CHAPTER 5. PREDICTION OF PROBABILISTIC DETONATION THRESHOLD VIA MILLIMETER-SCALE MICROSTRUCTURE-EXPLICIT AND VOID-EXPLICIT SIMULATIONS

This chapter is based on work currently in submission to Propellants, Explosives, Pyrotechnics (PEP). The work in this chapter was performed in collaboration with Drs. David Kittell and Cole Yarrington from Sandia National Laboratories.

5.1 Introduction

In this chapter, the dual nature of HEM shock initiation safety/performance is explored for HMX using a new computational framework; one that explicitly resolves microstructures, voids, and chemical reaction at the millimeter scale. These are mesoscale microstructure-explicit (ME), void-explicit (VE), and chemical-reaction-explicit (CRE) simulations performed with the Eulerian hydrocode CTH [87]. The objective is to show the SDT transition for the first time as a probability distribution map overlaid on a Pop plot, with the source of uncertainty being material heterogeneities. As described by Dick et al. [162], the Pop plot originated from shock initiation studies which varied the shock pressure input to a HEM with an explosive lens/attenuator. The response measure is the run distance to detonation recorded via a streak camera. The shock pressure vs run distance plot is usually in the log-log space and called the Pop plot (PP). Here, the probabilistic Pop plot (PPP) represents a further step beyond the previous work in Chapters 3 and 4 that have predicted a probabilistic ignition threshold in the James space [19, 20]. Randomized

microstructural generation is employed in addition to explicit modeling of the void distributions in order to quantify their rank-order effects on the total run distance to detonation. The probabilistic analysis is made possible via the generation and use of statistically equivalent microstructure sample sets (SEMSS). The multiple samples in a specific material set directly mimic the multiple samples in experiments, allowing statistical variations in material and material response to be studied [19, 20].

The microstructure-explicit (ME) and void-explicit (VE) simulations shown in this work not only resolve the material heterogeneities at the millimeter scale, they also capture the probabilistic nature of the SDT process. In these simulations, the constitutive relations are based on a simplified form of the SGL model, following recent success at calibrating this model in CTH [22]. Finally, a simplified reaction model is used to represent each of the individual HMX grains. This preliminary reaction model follows the work of Baer [14], which has been used in the absence of a more physically-relevant reaction model and equation of state (EOS) that are not currently available in CTH. The two-state history variable reactive burn model (HVRB), used here, has led to good agreement with experimental run distance to detonation and other continuum-level measurements in the past [14], and features a reaction rate that is based on local pressure. With these model assumptions, the shock to detonation transition events are set in motion by loading effected with an imposed piston velocity. This approach is often used to analyze the full SDT events on modern computing resources [163, 164].

Overall, the objectives of this work seeks to develop a novel probabilistic representation for quantifying both the shock sensitivity and performance of HEMs. While

the data sets used here to determine the parameters in the probabilistic representation come from computational simulations with the SEMSS, the probabilistic formulation can also be parameterized using independent experimental data sets. The results allow for the determination of the likelihood of observing SDT at a particular run distance under a given shock pressure. This further advance is based on, but goes beyond the work presented in Chapters 3 and 4 on thermal runaway and probabilistic ignition thresholds [19, 20]. In order to achieve this desired outcome, a new non-dimensionalized Pop plot characteristic parameter (called the Pop plot number) is proposed. The different effects of microstructure and voids on the probabilistic Pop plots are given in rank-order to gain insight into the meso (grain) scale mechanisms that underlie the SDT process. While current results pertain only to HMX, this approach could easily be repeated for other HEMs, including PBXs, which are either synthesized in a traditional manner or additively manufactured.

This chapter consists of two parts. The first part describes the computational framework used to study SDT at the mesoscale, including the design of the HMX microstructures, and a brief summary of the constitutive relationships and reaction model. The second part discusses the simulation results, focusing on the rank-order of the effects of different microstructural features as well as the development of the probabilistic Pop plot. This chapter concludes with major findings as well as directions for future work.

5.2 Framework of Analysis

Two-dimensional microstructures are generated and used. The impact loading is effected with a rigid piston traveling at different velocities. The run distance to detonation is calculated as the simulation progresses. The Sandia National Labs Eulerian hydrocode,

CTH, is used to simulate the full shock-to-detonation transition (SDT) process. The microstructure generation, constitutive relations, and computational framework are outlined in this section.

5.2.1 Material, Model and Microstructure

The material of interest is approximately based on class 3 pressed granular HMX [13]. Four types of models are considered: homogenous (H), microstructured without voids (M), homogenous with voids (V), and microstructured with voids (M+V), as shown in Figure 46. The homogeneous (H) and microstructured (M) samples are fully-dense (100% TMD). The voids in the V and M+V samples are circular in shape and have diameters of 50 μm. This void size is chosen to allow explicit resolution of each void in the 3×15 mm samples without rendering the already very intensive computations prohibitively expensive using 10,000-20,000 processor hours on supercomputers. Further discussions on mesh size and computational cost are in section 5.2.4. Section 5.3.1 studies the effect of void volume fractions ranging from 0% to 20%, while section 5.3.2 compares the effects of granular microstructure without voids relative to samples with 5% volume fraction of voids.

A set of five random but statistically similar granular HMX microstructures is generated using Voronoi tessellation. These samples conform to the statistical grain size distribution in Figure 47. This grain size distribution is monomodal, with a mean grain diameter of 220 μm. This method of microstructure generation results in realistic, randomized, and statistically equivalent microstructure sample sets (SEMSS). For samples with voids, individual voids are inserted randomly into either the homogenous or microstructure samples until the overall desired void volume fraction (0%, 5%, 10%, or

20%) has been reached. No two voids overlap, ensuring a constant void size and random void distribution. For further details on the microstructure generation process, see Chapter 2.

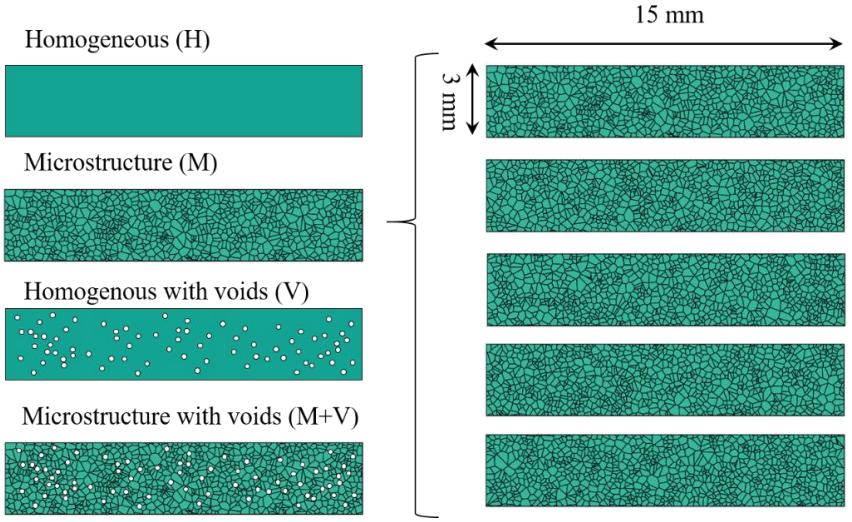

Figure 46 - Four HMX material cases considered in this study: homogeneous (H), microstructured (M), homogeneous with voids (V), and microstructured with voids (M+V). Multiple, randomized grain morphologies and void placements were generated to create the four statistically equivalent microstructure samples sets (SEMSS) for analysis.

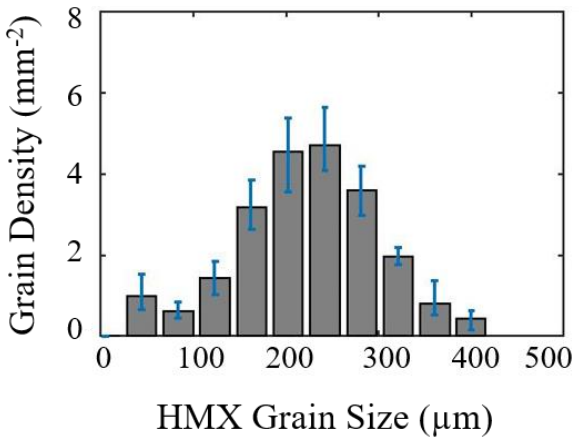

Figure 47 - Monomodal HMX grain size distribution used in the granular microstructures with and without voids.

Actual samples in experiments have more heterogeneous characteristics than those in the four sets of samples presented here. For example, nano- and micro-scale voids, microcracks, and directionality of the material properties due to the anisotropic nature of the HMX crystal all play roles in the response of the materials to shock loading. These factors are too small and computationally expensive to be explicitly resolved in the current model setting. To account for the effects of these factors via grain-level heterogeneities, the density of the HMX for each grain is set to one of three possible values: 70% TMD (1.33 g/cm^3), 100% TMD (1.90 g/cm^3), and 130% TMD (2.47 g/cm^3). These density variations emulate the effects of local variations in the material and represent one source of variations in fields behind the shock front normally attributed to localized material heterogeneities. It is important to note that even though 130% TMD is a nonphysical description of a material, the variations in density are employed here as a modeling tool to introduce the heterogeneous reactive behavior. More specifically, the Mie-Grüneisen EOS returns a different shock pressure for each initial density; and since the HVRB chemistry model used here is pressure dependent (further detailed in Section 5.2.2), even the explicit microstructure case (M) has spatial variations in the reaction rate. Such variations lead to the heterogeneous behavior as seen in actual samples, while keeping the overall HMX density consistent at 100% TMD. A variation of 30% about the 100% TMD was calibrated based on the work of Hardin et al. [165] who found the coefficient of variation in the longitudinal stress field in the quasi-steady region behind the stress wave front in polycrystalline HMX varies from 0.08 to 0.16 at piston velocities around 400 m/s. In this study, the grains are assumed to be perfectly bonded to one another. If two grains with the

same density are positioned next to one another, they behave as a single grain of the same density. For the H and V samples, the standard HMX 100% TMD (1.90 g/cm^3) is used.

The present framework represents a simplified approach toward explicitly resolving various microstructures commonly seen in HEM. While the method of varying the density of the HMX grains may replicate the trends seen in experiments, it is difficult to fully quantify the effect of heterogeneity into a single parameter. Actual experimental samples have clear defects not accounted for here, which are known to contribute to hotspot initiation and subsequent detonation [20, 101, 166, 167]. Other HEMs have binder and additive components, such as aluminum, which can affect the sensitivity of the material to ignition [155]. It is entirely possible that microstructure heterogeneity plays an even larger role than what is presented in the results of this study. However, the current framework should be regarded as a step toward fully accounting for the most essential material heterogeneities up to the overall mm macroscopic size scale.

5.2.2 Constitutive Relations

The elastic-viscoplastic model, equation of state (EOS), and chemistry model are most relevant to the community and the analyses here. Consequently, they are discussed in this section. Only a brief summary is provided here, as the full details of these models have already been described in Chapter 2.3. The specimen is initially stress-free and at rest. This is a 2D model and the conditions of plane-strain prevail. A single piston velocity (U_P) is applied on one end of the sample to effect shock loading. The side (lateral) boundaries are constrained in a frictionless manner to maintain the overall conditions of sample-level uniaxial strain typical of planar impact experiments.

A simplified Steinberg-Guinan-Lund strain-dependent flow stress model (SGL) is used to account for the viscoplastic behavior of HMX. This model has been calibrated to match the elasto-viscoplastic model used for HMX in Chapters 3 and 4 of this thesis which in turn was based on available experimental data. The values of the material parameters in the model are listed in Table 4 in Chapter 2. The bulk response to hydrostatic pressure is modeled using the first order Mie–Grüneisen EOS. This is a common EOS used to model material subjected to shock loading. Unlike the Birch-Murnaghan EOS used in the Lagrangian framework in Chapters 2 and 3, the Mie–Grüneisen EOS includes an internal energy dependence that is estimated at each time step by integrating the specific heat with respect to temperature as described in Eq. (16). The values of the material parameters in the EOS model are listed in Table 5 in Chapter 2.

The process of chemical reaction initiation and progression follows the history variable reactive burn model (HVRB). This is a pressure dependent burn model which does not explicitly track species of reactants or products. Reactive burn models have been widely used to simulate the ignition and detonation of HEMs [14, 83, 84]. These empirical models are often calibrated to Pop plot data. As a result, the localized extent of reaction behind the shock front may not be perfectly resolved (which is a known limitation for the HVRB model). However, with available data and models, this is a reasonable trade-off in order to reach the macroscale from the mesoscale, since the focus here is on analyzing macroscale material behavior. The HVRB model provides a straightforward method of accounting for chemical reaction at larger size scales which would otherwise prove more computationally intensive if an Arrhenius-based chemical reaction rate model is used. Still, it is worthwhile to note that if and when a more useful chemistry model is made available,

it can be easily used in the current framework – there is no fundamental impediment to the use of other, especially more mechanisms-based, reaction models.

5.2.3 Shock Pressure and Run Distance Calculation

Run distance to detonation (RDD) is a common performance metric used to measure SDT sensitivity and performance of an energetic material. In this analysis, the RDD is defined as the longitudinal distance the shock wave travels into the explosive before the detonation wave front is established. Initially, the stress field following the shockwave is relatively uniform (in the homogeneous samples), due to the monotonic loading applied. When voids or microstructure are introduced, the stress field deviates from this idealized scenario as the shock front encounters material heterogeneity. The reaction builds up behind the shock front, and at later times strengthens it before eventually overtaking the shock front and propagating through the uncompressed material as a detonation wave.

The relationship between the RDD and pressure of imposed shock loading, or the Pop plot, can be used to compare the relative performance of different materials. In the analysis here, the relations are used to quantify the differences in performance due to microstructure and voids of the four HMX cases. The shock pressure is calculated based on the spatially averaged pressure profile of each sample. The initial plateau of the stress wave is measured and averaged over both sample distance and time in order to determine the most accurate monotonic shock pressure for a given impact velocity. In order to calculate the run distance, the location of the shock front in the sample is recorded as a function of time. Since the detonation wave propagates faster than the inert shock wave, the run distance is easily measured by examining the change in velocity of the shock front

itself. An example pressure profile and shock front location of a granular microstructure without voids under loading by a piston velocity of $U_p = 800\,\text{m/s}$ is shown in Figure 48.

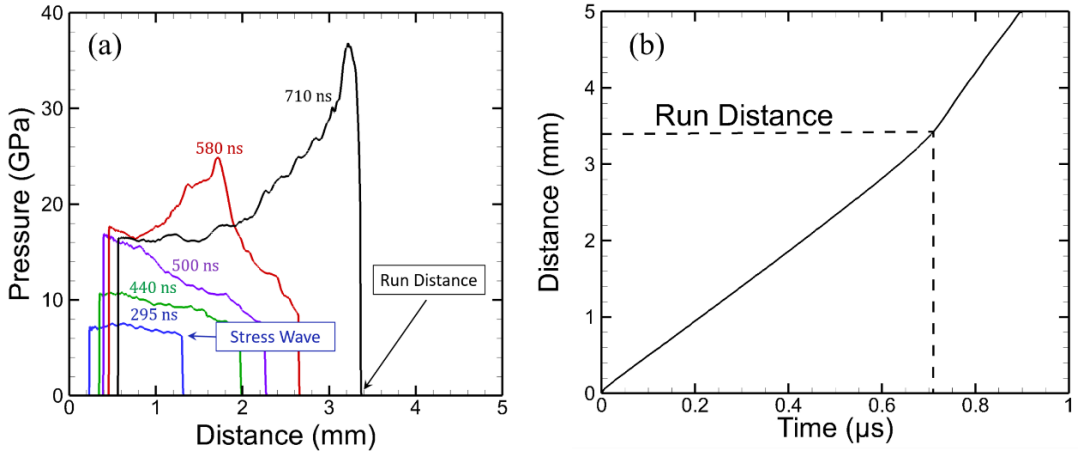

Figure 48 - (a) Pressure profile behind the shock front at multiple time steps for a microstructure sample impacted at $U_P = 800$ m/s. (b) Distance traversed by the shock front as a function of time for the same microstructure sample impacted at $U_P = 800$ m/s.

The fields of pressure, temperature, and the extent of reaction (λ) are analyzed to delineate the effects of voids and granular heterogeneity. Figure 49 shows the pressure fields at different stages of the SDT process for a microstructured HMX sample with voids impacted by an aluminum flyer at 400 m/s. The fields cover hotspot initiation to full detonation completion.

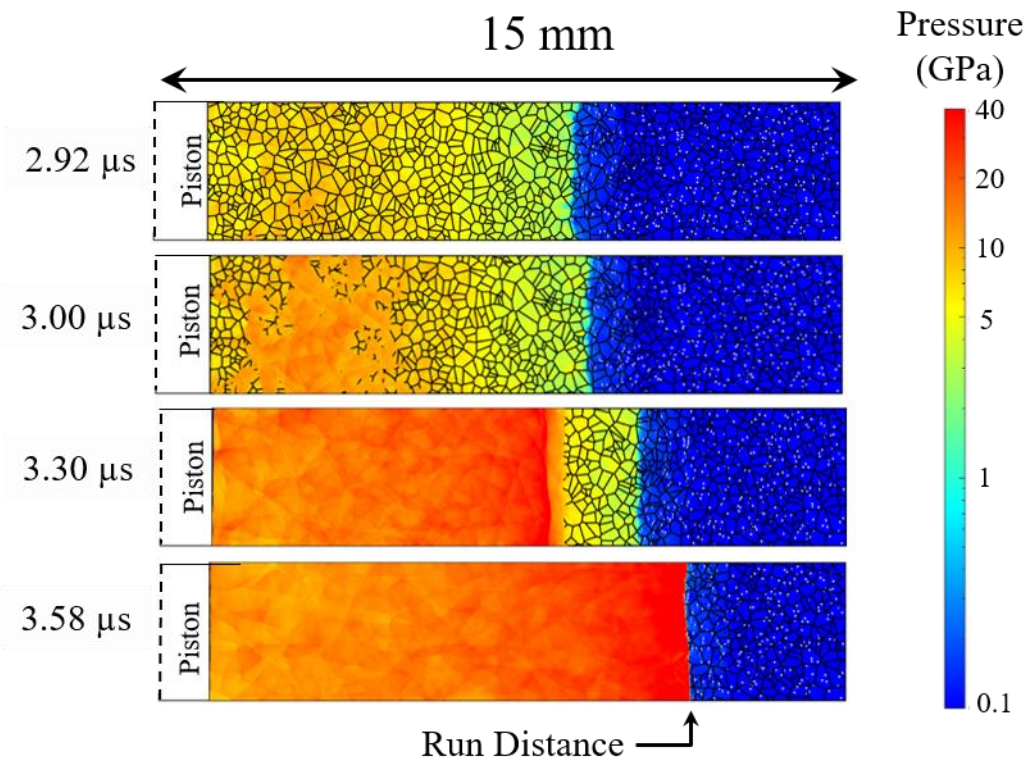

Figure 49 - Pressure fields for an HMX sample containing both microstructure and voids impacted by an aluminum flyer at $U_P = 400$ m/s.

5.2.4 Mesh and Size Convergence

To ensure accurate results, a mesh convergence study is carried out to determine the proper mesh size necessary to explicitly resolve both the grains and voids and ensure convergence of solution of interest. To this end, shock pressure and RDD are calculated for samples including both microstructure and voids at mesh sizes ranging from 30 μm to 500 nm. The M+V sample set was chosen for this purpose because it accounts for both kinds of heterogeneities. Naturally, the mesh sufficient for modeling the most complicated HMX microstructures should be sufficient for the less complicated microstructures as well. As shown in Figure 50, the shock pressure is found to converge at any resolution finer than

20 µm, while the run distance converges for any mesh size finer than 5 µm. For this reason, a final mesh size of 5 µm is chosen for all subsequent tests. It is important to note that this study is focused on the macroscale detonation properties of the material. A finer mesh resolution would likely be required to accurately resolve local temperatures which may be required for an Arrhenius-based chemical reaction rate model, as is commonly used for small scale simulations in the literature. The HVRB chemical reaction model used here (as outlined in section 5.2.2) is a pressure-dependent model that does not require direct use of temperature. For this reason, the convergence study here also provides a validation of the average shock pressure.

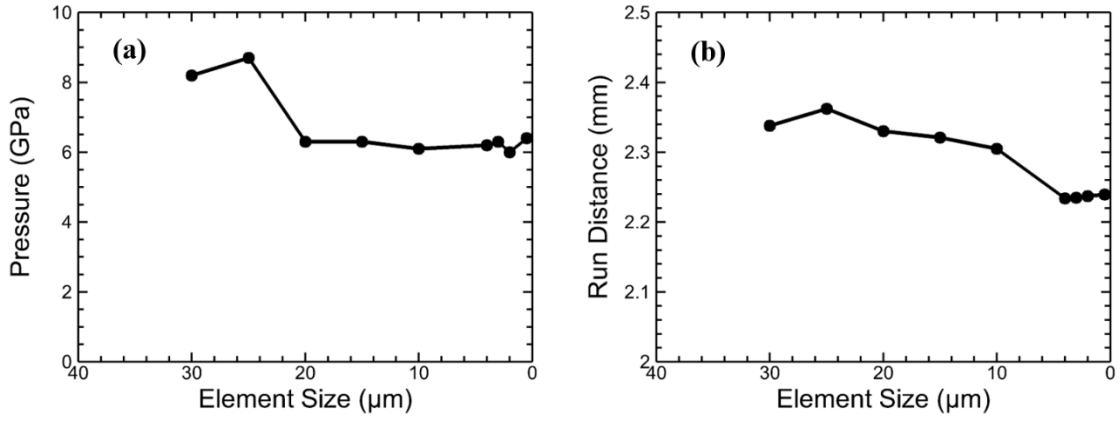

Figure 50 - (a) Shock pressure and (b) run distance to detonation for a sample with granular microstructure and voids at mesh resolutions ranging from 30 µm elements to 500 nm elements.

In addition to a mesh resolution study, it is important to determine whether the sample size chosen serves as an acceptable representative volume element (RVE) for the microstructure as a whole. While the smallest microstructure feature (voids) dictates the necessary mesh resolution, the largest microstructure feature (grains) dictates the necessary RVE size of the sample. To this end, five 1 mm × 5 mm samples, with the same randomized

grain distributions as in the 3 mm × 15 mm samples (see Figure 47), are subject to the same impact loading and the detonation process is analyzed in the same as manner as that in the 3 mm × 15 mm samples. The resulting shock pressure prior to detonation and the run distance to detonation are calculated. The results are shown in Figure 51. The overlap and near full coincidence of the data points from the two sets of samples indicate that the 1 mm × 5 mm sample size yields practically the same results as the 3 mm × 15 mm sample size, and therefore the 1×5 mm samples are large enough to be RVEs. For the remainder of this analysis, calculations are conducted using 1 mm × 5 mm samples to minimize computational cost.

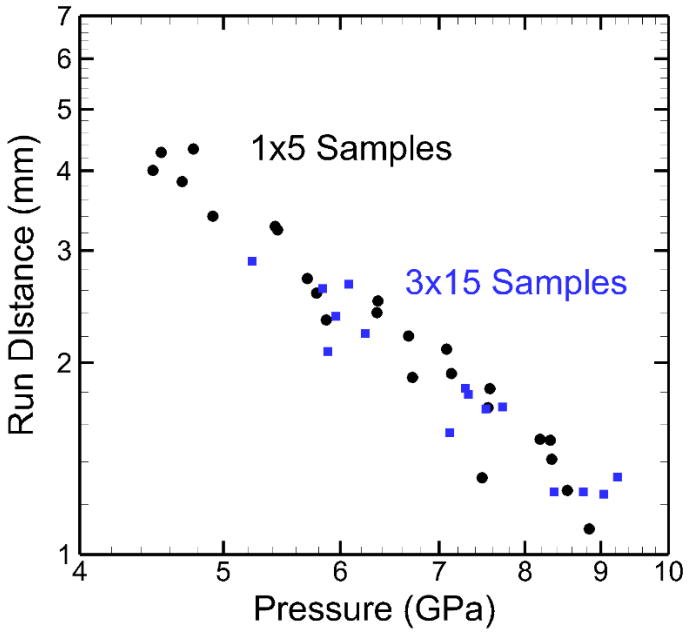

Figure 51 - Run distance to detonation as a function of shock pressure for five 1×5 mm samples (black circles) and five 3×15 mm samples (blue squares) with randomized grain distributions and no voids. Piston velocities ranging from 600 m/s – 1000 m/s are used to generate the range of shock pressures seen here.

5.3 Results and Discussion

A systematic quantification of the effect of granular microstructure and void volume fraction on the performance and sensitivity of pressed HMX is carried out. Section 5.3.1 compares the effects of homogenous samples with four volume fractions of 50 μm circular voids (0%, 5%, 10%, and 20%) on the Pop plot. Section 5.3.2 discusses the differences in samples with and without voids and granular microstructure; a comparative rank-ordering of the Pop plot results is also given. A probabilistic model for the SDT transition is developed in section 5.3.3, using the results presented in section 5.3.2. This formulation allows the likelihood of achieving run to detonation at a given distance to be mapped over the entire range of loading pressures studied. Finally, in section 5.3.4 the prediction obtained in section 5.3.2 is compared with available experimental data.

5.3.1 Effects of Void Volume Fraction

It is well known that microstructural heterogeneities contribute to increased sensitivities of energetic materials to ignition. The presence of voids in the material results in extreme shear stress and local plastic deformation at the defect locations under shock loading conditions. The hotspot formations due to pore collapse are considered to play a dominate role in the sensitivity, and subsequent detonation of HEMs. Accurately characterizing the effects of voids is essential in mesoscale simulations [168]. In this section, we examine the effect of increasing the volume fraction of voids on the run distance to detonation of HMX samples without microstructure or other forms of heterogeneity.

Homogeneous HMX samples with four levels of void volume fractions are analyzed: 0% (homogeneous), 5%, 10%, and 20%. These values are chosen to track void volume fractions commonly observed in experiments of pressed HMX [43]. All voids are initially circular with the same diameter of 50 μm. The voids are placed randomly so that no two voids initially overlap or directly contact the edges of the sample. For each of the four void volume fractions, five statistically equivalent random samples are generated, resulting in five 5% void samples, five 10% void samples, and five 20% void samples. Each sample is subjected to loading at each of the following piston velocities: U_{P} = 600, 700, 800, 900, and 1,000 m/s. The use of multiple statistically equivalent samples over a range of piston velocities allows for measurement of both shock pressure and run distance in a manner that captures the stochastic variations in the material behavior. The results of this analysis are shown in Figure 52. Clearly, the run distance decreases as the void volume fraction increases. The average decrease in run distance with void volume fraction is normalized with respect to the 0% void case and is listed in Table 18.

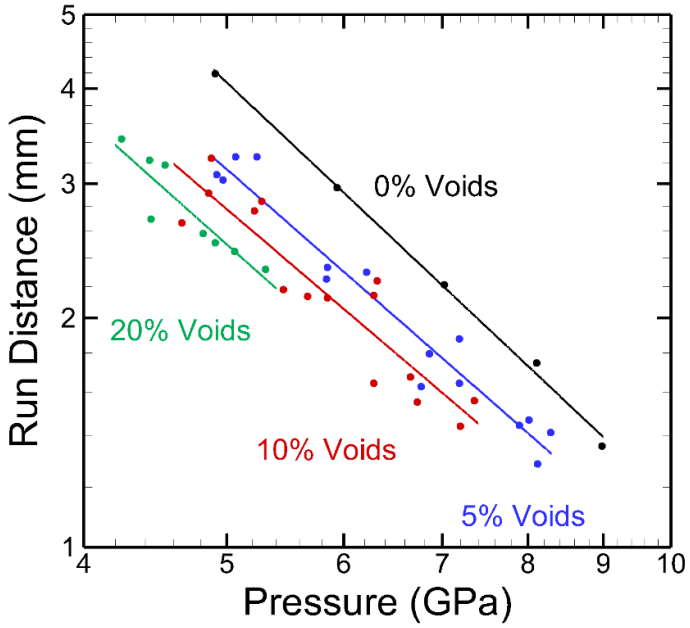

Figure 52 - Pop plots of samples with 0% void (black), 5% voids (blue), 10% voids (red), and 20% voids (green) by volume. All voids are initially 50 μm in diameter. Other than the voids, the samples contain no other heterogeneities.

Table 18. Effect of void volume fraction on normalized run distance

Void Volume Fraction	Average Decrease in Run Distance
0%	0%
5%	20.6%
10%	28.8%
20%	37.2%

For a given shock pressure, increasing the volume fraction of voids in turn causes the run distance to detonation to decrease (and therefore lowers the PP line). Table 18 shows that the rate of decrease in the run distance decreases at higher void volume

fractions. Specifically, a 5% volume fraction of voids causes the run distance to decrease on average by 20.6% relative to the homogeneous material case over the entire range of shock pressure. Increasing the void volume fraction from 5% to 20%, on the other hand, causes the run distance decrease relative to the 0% case to change from 20.6% to 37.2%, a smaller 16.6% change. While increasing the volume fraction of voids lowers the Pop plot line, a trend that is associated with better detonation performance of a HEM by itself, trade off must also be considered. Specifically, voids cause the overall effective density of the material to decrease, which leads to lower shock pressure under the same impact velocity. This means a higher, more severe loading might be required to generate the same performance or effect. In addition, voids also decrease the overall energy content in a HEM, causing the overall energy output per unit macroscopic volume of the material to be lower. These factors must be weighed.

5.3.2 Effect of Granular Heterogeneities

We now consider the effects of the granular microstructure, as well as the interactions between the effects of the microstructure and voids, on the Pop plot. For this purpose, the four material cases in Figure 46 are considered: homogeneous (H), granular microstructure only (M), 5% voids only (V), and both microstructure and voids (M+V). The overall results are shown in Figure 53. As different forms of heterogeneities and material defects, microstructure and voids each causes the Pop plot lines to shift to the lower left in pressure-run distance space. In other words, the run distance decreases at a given shock pressure as more heterogeneities are included. The average decrease in run distance for each material

case (H, M, V, M+V) has been normalized with respect to the homogeneous case (H), as listed in Table 19.

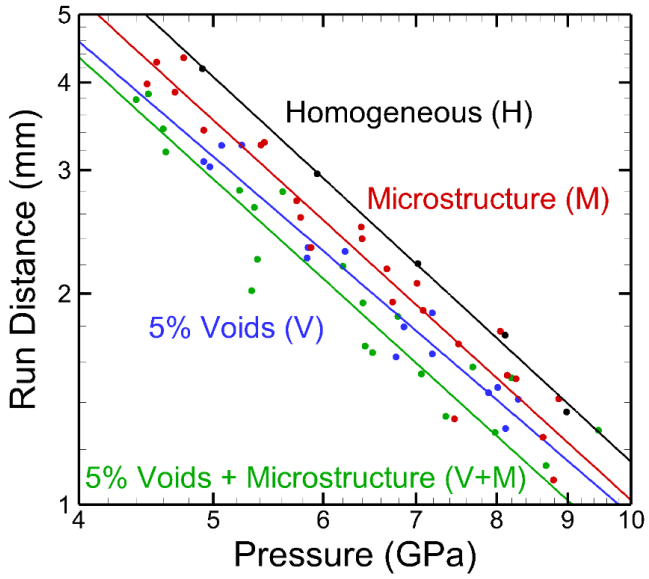

Figure 53 - Pop plot lines for the homogeneous samples (black), granular microstructured samples (red), samples with 5% voids by volume only (blue), and samples with 5% voids and granular microstructure (green).

Table 19. Effect of material heterogeneities on normalized run distance

SEMSS	Average Decrease in Run Distance
Homogeneous (H)	0%
Microstructure (M)	12.3%
5% Voids (V)	20.6%
5% Voids and Microstructure (V+M)	27.5%

For the range of pressure considered, homogeneous samples have the highest Pop plot line, or the longest run distance at a given pressure. Voids and granular microstructure

each cause the Pop plot line to move toward the lower left in the shock pressure-run distance space. Relatively speaking, the effects of 5% voids are stronger than the effects of granular heterogeneities embodied by ±30% grain-grain variations in the density of the material. The Pop plot line for samples with both microstructure and voids have the lowest Pop plot line, or the fastest SDT in terms of run distance and time among the cases analyzed. The results in Table 18 allow a rank-order of the effects of microstructure and voids to be established. A graphical illustration of this ordering is given in Figure 54. From the lowest to highest SDT performance: homogenous HMX, HMX with only microstructure, HMX with 5% voids, HMX with 5% voids and microstructure, HMX with 10% voids, and HMX with 20% voids.

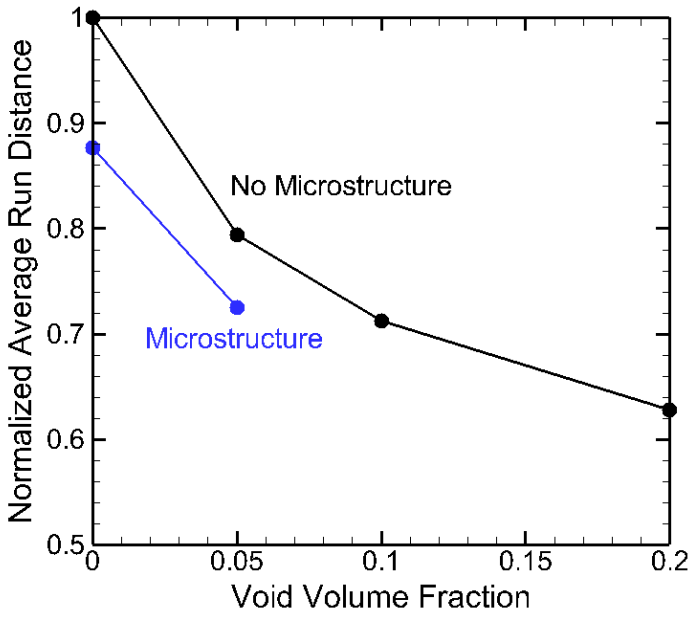

Figure 54 - Normalized averaged decrease in run distance of samples with and without granular microstructure (blue and black respectively) as compared to homogeneous HMX as a function of void volume fraction.

For the 0% and 5% void cases, adding granular microstructure decreases the run distance by 12.3% and 6.9%, respectively. Clearly, microstructure has a significant effect on the SDT behavior and the Pop plot. It is important to point out that a relatively idealized microstructure representation is used here, as the only material heterogeneity is in the density (which in turn affects the EOS). In reality, material heterogeneities lie in constitutive behavior, crystal orientation and associates strength anisotropy, reaction kinetics, and thermal behavior. As such, the overall effects of microstructure are likely more pronounced than what is stated here. The current analysis should be regarded only as a first order estimate of the lower bound of the effects of microstructure relative to the effects of voids. In addition, only one relatively large void size (50 μm) is analyzed here. Void size is expected to affect the results [18, 169, 170].

5.3.3 Probabilistic Pop plot model

Up until now, the discussions regarding the rank-ordering of the effects of different microstructural attributes on SDT behavior have focused on the best curve fit associated with each Pop plot data set. This takes the form of a single line that represents the "average" behavior or trend. The analysis does not account for the fact that the behavior of HEM are stochastic due to several factors, the most important of which is intrinsic material heterogeneities at lower scales. The behavior of individual samples scatter around the overall trend line and the type and extent of heterogeneities determine the statistical spread and the uncertainties involved. There is a strong need to quantify not only the overall "average" behavior, but also the statistical distribution of the material behavior. The quantification must allow the uncertainties associated with SDT behavior assessment to be

determined. Here, we use the SEMSS and the statistical SDT data sets obtained from the SEMSS to develop a probabilistic formulation for the Pop plot itself. To begin, each set of Pop plot data is fit to the standard power law

$$x^* = SP_s^{-m}, \tag{43}$$

where S is a material-dependent scaling parameter, m is an exponential fitting parameter, x^* is the run distance, and P_s is the shock pressure. This standard method Pop plot line represents the threshold of having 50% of the samples in a data set achieve SDT by a given run distance at a given pressure. In order to capture the probabilistic behavior of the Pop plot data set and quantify the likelihood of observing SDT at other combinations of run distance and shock pressure away from this line, a modified form of Eq. (43) is proposed with the introduction of a new, non-dimensional parameter D in the form of

$$D = \frac{\left(P_s - P_0\right)^m \left(x^* - x_0^*\right)}{S}. \tag{44}$$

This parameter can be regarded as the Pop plot characteristic number or the Pop plot number (PPN). It provides a measure of deviation from the 50% trend line of Eq. (43) in the run distance vs. shock pressure space, with $D > 0$. In particular, $D = 1$ represents the threshold where 50% of the samples reach detonation (i.e., the traditional PP line); and $D > 1$ and $D < 1$ correspond to conditions for attaining SDT at greater than 50% and less than 50% probabilities, respectively. P_0 is the shock pressure below which no SDT occurs, and x_0^* is the minimum run distance for observing SDT. These quantities can be regarded as material parameters which constitute bounds for P_s and x^*, respectively. Including these

parameters allows the model to account for and separate conditions under which SDT may or may not occur. In particular, shock pressures that are too low may never lead to detonation (no go) as the applied energy disperses too quickly to form critical hotspots. The minimum run distance x_0^* , on the other hand, recognizes the fact that chemical reactions cannot occur instantaneously. Unlike the *S* and *m* material parameters in Eq. (43) the values for P_0 and x_0^* cannot be accurately predicted by fitting Eq. (44) to the data set here, as the calculations carried out here do not concern the physical conditions for these parameters. Instead, their values must be carefully determined based on independent experimental observations or separate computations with appropriate constitutive, EOS and chemistry models at both high and low shock pressures. That task is beyond the scope of this thesis. According to the LASL explosive property database, the lowest recorded pressure tested for SDT is 4.41 GPa [171]. Low density HMX (65% TMD), which is known to be more sensitive than 100% TMD HMX, has been observed to reach SDT at shock pressures as low as 400 MPa [172]. Welle et. al calculated a minimum possible power flux required for ignition of Class 3 pressed HMX samples of 0.35 GW/cm^2 [13]. Using the basic dynamic pressure equations, this minimum flux value roughly corresponds to a shock pressure of 2.26 GPa. Due to the lack of experimental data required to provide an accurate value for either P_0 or x_0^*, they are treated here as insensitive fitting parameters. An accurate calibration of both parameters is required for future work in either the high or low pressure regime. If and when such data is obtained, they can be used to demarcate the domain in the shock pressure – run distance space in which the probabilistic analyses below can be more accurately used. Within that domain, these parameters have negligible bearing on the accuracy or validity of the analyses here.

The PPN offers a mechanism to quantitatively determine the probability of reaching SDT at any given point in the entire run distance and shock pressure space (the Pop plot space). Under the assumption that the distribution of data points in each data set follows a log-normal distribution about the line of Eq. (43), D can be used to obtain the cumulative probability of observing SDT in the form of

$$\mathscr{P}(D) = \frac{1}{\sigma_d \sqrt{2\pi}} \int_0^D \frac{1}{x} \exp\left[\frac{-\left(\ln x - \mu\right)^2}{2{\sigma_d}^2} \right] dx, \tag{45}$$

where μ is the mean of the natural logarithm of the PPN, and is the standard deviation of the spread of all data points in a given set around the 50% mean represented by Eq. (43). A log-normal distribution is chosen as it ensures the probability is symmetric about the PP line in log-log space. Since the mean value of the PPN is unit by definition, Eq. (45) may be simplified to

$$\mathscr{P}(D) = \frac{1}{\sigma \sqrt{2\pi}} \int_0^D \frac{1}{x} \exp\left[\frac{-\left(\ln x\right)^2}{2{\sigma_d}^2} \right] dx. \tag{46}$$

This may be rewritten as

$$\mathscr{P}(D) = \frac{1}{2} + \frac{1}{2} \operatorname{erf}\left(\frac{\ln D}{\sqrt{2}\sigma_d} \right), \tag{47}$$

where $\mathscr{P}$ is the probability of reaching SDT and D determines the location in the Pop plot space via Eq. (44). The fit for the homogeneous with 5% voids (V) SDT data set is shown in Figure 55. The material parameters for all data sets are shown in Table 20.

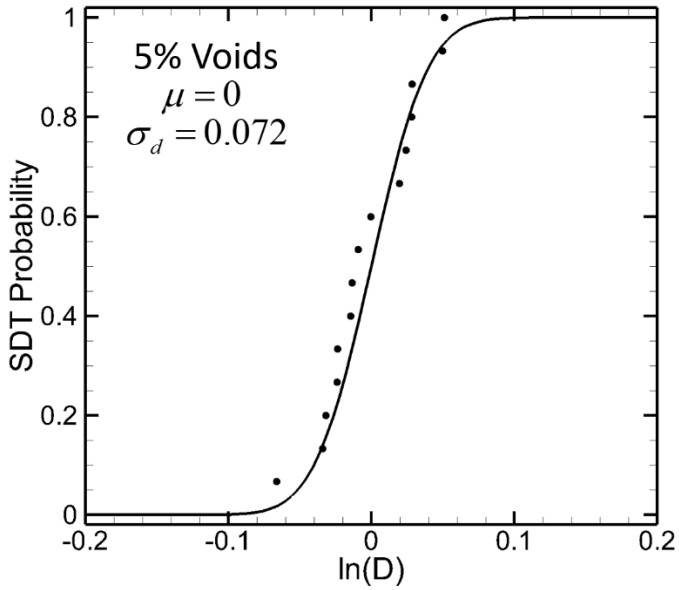

Figure 55 - Cumulative SDT Probability as a function of the natural logarithm of the Pop plot number, *D*, for homogeneous samples with 5% voids (V). The data set is fit to Eq. (47).

Table 20. Probabilistic material parameters for all cases of HMX

Sample Type / Material Parameter	σ_d	S	m
Homogeneous (H)	0.024	73.5	1.80
Microstructure (M)	0.094	62.0	1.78
5% Voids (V)	0.072	58.2	1.84
5% Voids + Microstructure (V+M)	0.179	56.6	1.93

The form of Eq. (47) mirrors the probabilistic ignition threshold proposed in Chapter 3, which was initially based on the *J* parameter (or James number) first proposed by Gresshoff

and Hrousis [106]. Here, the Pop plot number *D* resembles the *J* parameter. Substituting Eq. (44) into Eq. (47) gives the probability function in terms of the run distance and shock pressure, i.e.,

$$\mathscr{P}(P_s, x^*) = \frac{1}{2} + \frac{1}{2}\,\mathrm{erf}\left[\frac{1}{\sqrt{2}\sigma_d}\left(\ln\left(\left(P_s - P_0\right)^m\right) + \ln\left(x^* - x_0^*\right) - \ln S\right)\right]. \tag{48}$$

In the above expression, $\mathrm{erf}\left(\cdot\right)$ is the error function. Using Eq. (48), we can generate a probability map for the entire Pop plot space of shock pressures and run distance for each material case. The resulting probability maps for the four materials cases analyzed are shown in Figure 56. These SDT probability distribution maps are the first of their kind and provide a systematic and quantitative means for predicting the probability of observing SDT at any combination of run distance and shock pressure. This analytical form can be used to guide experiments and selection of material by quantitatively relating common macroscopic measures. It is useful to point out that σ_d, *m*, and *S* in Eq. (48) are material parameters that are determined by the data set (obtained computationally or experimentally) for each material case. Ultimately, they can and should be expressly written as functions of material attribute measures such as constitutive properties, grain size, grain volume fraction, void content/size, and interfacial properties. Such an endeavor is not undertaken here, but the framework developed here lends itself to such future development.

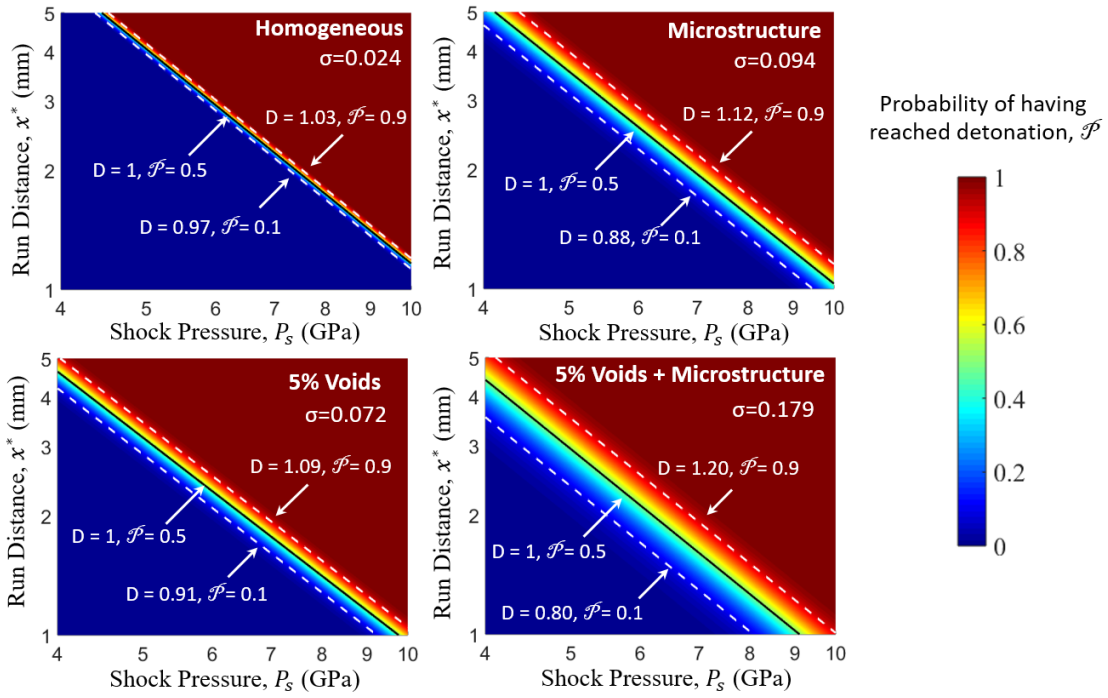

Figure 56 - SDT probability distribution maps for the four cases of HMX analyzed: homogeneous (top left), microstructure (top right), 5% voids only (bottom left), and both voids and microstructure (bottom right).

Recently, Wei et al. extended this probabilistic approach from the James space for ignition thresholds to the Pop plot space for detonation thresholds [173]. It is further expanded upon here by recognizing that the SDT probability itself may serve as an input parameter for evaluating other quantities of interest in different design or materials selection scenarios. While Eq. (48) is useful in determining the likelihood of observing SDT for a given combination of shock pressure and run distance, it may also be used to calculate necessary conditions needed in order to reach a desired probability of detonation at a particular run distance or shock pressure. Specifically, the relation can be recast in the following form for calculating the minimum run distance required for achieving SDT with a given level of probability under a particular shock pressure

$$x^*(\mathscr{P}, P_s) = \frac{S}{\left(P_s - P_0\right)^m} \exp\left[\sqrt{2}\sigma_d \left(\text{erf}^{-1}\left(2\mathscr{P} - 1\right)\right)\right] + x_0^*. \tag{49}$$

In the above relation, $\text{erf}^{-1}(\cdot)$ is the inverse error function, which approaches negative infinity at $\mathscr{P} = 0$ and positive infinity at $\mathscr{P} = 1$. There is no convenient closed form expression for the inverse error function and it is generally calculated numerically. The relationship described by Eq. (49) has been mapped out over shock pressures ranging from 4-10 GPa and is shown in Figure 57 for the four material cases analyzed.

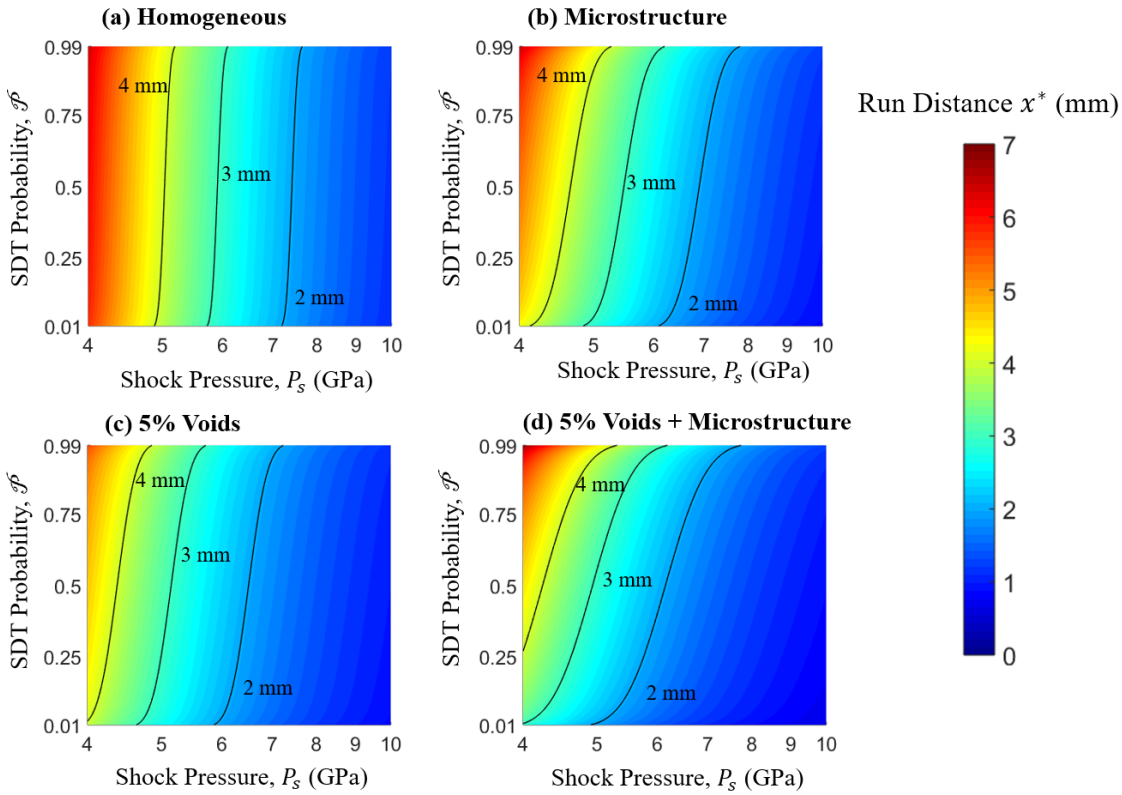

Figure 57 - Necessary run distance to achieve a desired SDT probability under a given shock pressure for the four cases of HMX analyzed: (a) homogeneous, (b) microstructure, (c) 5% voids only, and (d) both voids and microstructure.

Similarly, the shock pressure required to achieve SDT at a specific run distance at a required probability is

$$P_s(\mathscr{P}, x^*) = \left\{ \frac{S}{\left(x^* - x_0^*\right)} \exp\left[\sqrt{2}\sigma_d \left(\text{erf}^{-1}\left(2\mathscr{P} - 1\right)\right)\right] \right\}^{\frac{1}{m}} + P_0. \tag{50}$$

This relationship has been mapped out over run distances ranging from 1-5 mm for the four material cases, and the result is shown in Figure 58.

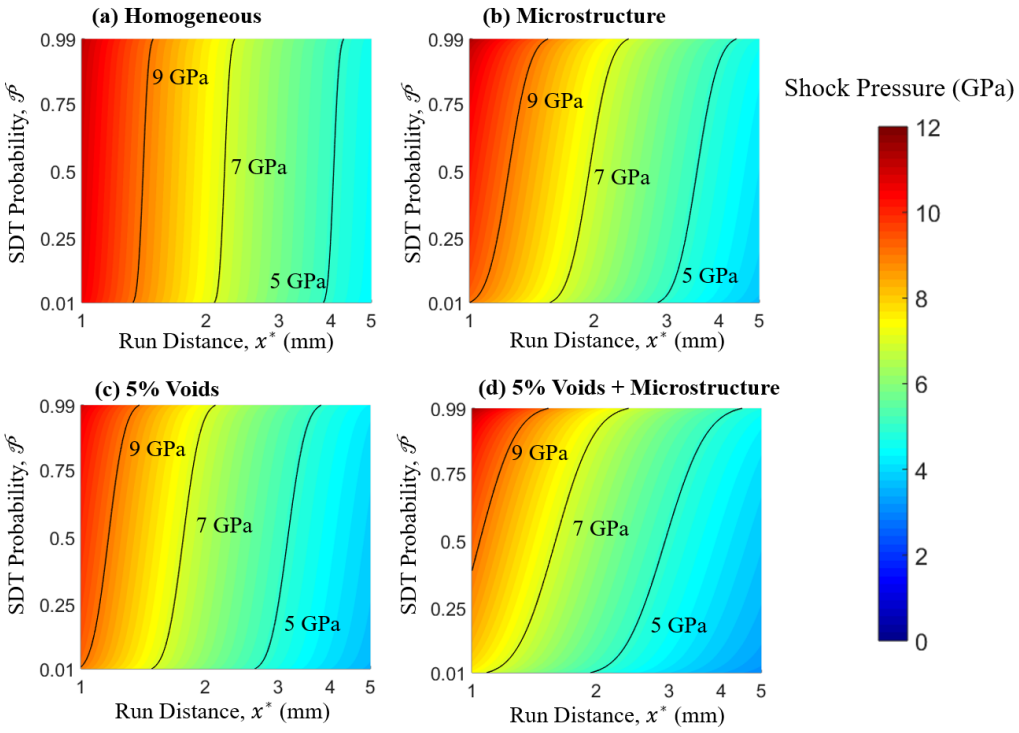

Figure 58 - Necessary shock pressure to achieve a desired SDT probability at a given run distance for the four cases of HMX analyzed: (a) homogeneous, (b) microstructure, (c) 5% voids only, and (d) both voids and microstructure.

Both Eq. (49) and Eq. (50) result from simple algebraic manipulations of Eq. (48).

5.3.4 Experimental Comparison

A look at the prediction presented here in the context of available experimental data is in order and helpful. Figure 59 compares the results from section 5.3.2 with reported experimental Pop plot results for HMX (86% TMD) from Lawrence Livermore National Lab (LLNL) [172] and fully packed HMX (100% TMD) from Los Alamos National Lab (LANL) [171]. The results here are in general agreement with the experimental data in terms of overall trend. Only the 50% lines are shown, as there is a lack of statistical quantification in the experimental data sets. The decreasing of the predicted Pop plot lines as heterogeneities increase is consistent with the trend in the experimental data (density decreases). This is a first attempt at predicting the macroscopic PP using ME and VE mesoscale models. It is important to bear in mind the challenges in comparing such simulations to experiments. First, there are wide variations among the different experimental data sets. Possible reasons include material sample differences and inconsistencies (different batches of materials prepared at different times and locations can be significantly different), lack of quantification of grain size, void content, and statistical variations of these attributes, and experimental loading condition differences (different types of flyers, shock pressure and run distance measurement errors, etc.). Second, like any model, the model used here includes simplifications and assumptions, including the use of the specific HVRB chemistry model. With these factors in mind, we see that the simulations show that the homogeneous HMX case has a Pop plot line that is below that of the experimentally reported 100% TMD material. This may be the result of limiting the computational analysis to a 2D plane strain model and the calibration of the HVRB used. The exact cause of this discrepancy should be analyzed in future work. The work presented

in this chapter is only a first attempt at modeling the behavior of HMX at the macroscale with explicit account of both voids and microstructure. More localized material factors and processes are not explicitly resolved, and may account for some of the discrepancies seen between the simulations and experiments. Note also that the samples with voids (V) approximately correspond to the 95% TMD HMX in the experiments, with the understanding that detailed microstructure analyses were not reported in the references cited.

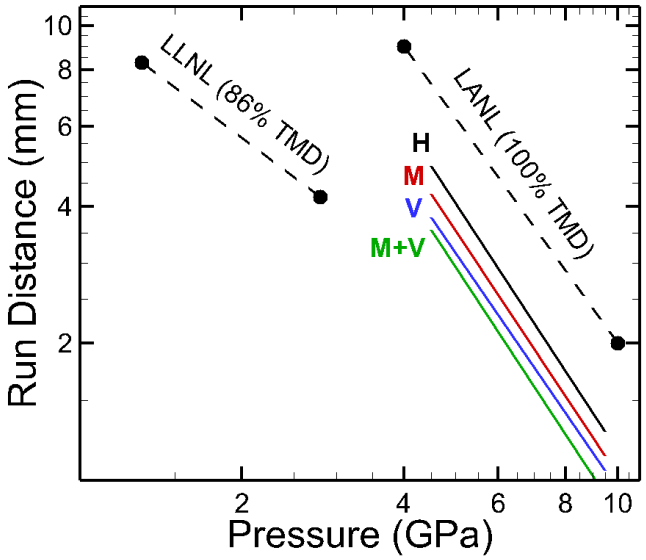

Figure 59 - Comparison of the predicted Pop plot lines (colored solid) with available experimental data in the literature (dash lines). The predicted lines shown are for homogeneous HMX (H), HMX with microstructure (M), HMX with 5% void volume fraction (V), and HMX with both microstructure and voids (M+V) material cases.

5.4 Conclusion

This chapter has presented a mm-scale model for analyzing the SDT behavior of heterogeneous energetic materials. The model samples are microstructure-explicit, void-explicit, and large enough (mm length scale) to track the largest material size scale and

SDT behavior size scale for common polymer-bonded explosives and granular explosives. The shock to detonation (SDT) behaviors of homogeneous HMX, HMX with granular microstructure, HMX with voids, and HMX with both granular microstructure and voids are analyzed and rank-ordered. The full transition from hotspot initiation to detonation is simulated using an Eulerian computational framework which resolves the material heterogeneity and the coupled thermal-mechanical-chemical processes underlying the response of energetic materials under shock loading.

Simulations carried out show that adding a 5% volume fraction of voids to an otherwise homogeneous material decreases the average run distance by 20.6%. On the other hand, increasing the void volume fraction from 5% to 20% shortens the run distance by 37.2% relative to the homogeneous case. The heterogeneous microstructure also plays an important role in affecting the SDT behavior, causing the average run distance to decrease by 12.3% relative to the homogenous material. When both microstructure and voids (M+V) are present, the average run distance decreases by another 6.9% over that of the material with 5% voids by volume. The results show that both voids and microstructure significantly affect the SDT process and the SDT thresholds. Further, as sources of heterogeneities, the effects of microstructure and voids on the SDT behavior are additive and interactive, implying that both must be considered and one cannot be used to account for the effects of the other. It is useful to bear in mind that the representation and resolution of microstructure heterogeneities are relatively simple and not exhaustive. Actual effects of microstructure are likely larger. The effects of void size are not explored in this work.

A probabilistic formulation for quantifying the Pop plot is developed. This relation is general in nature and applicable to any type of HEM. It provides a useful framework for analyzing, selecting, and designing HEM. The relationship (Eq. (48)) can be used to determine the probability of observing the SDT at a given shock pressure and run distance. If a specific probability of SDT is desired, Eqs. (49) and (50) may be used to determine the necessary shock pressure or run distance, respectively. Ultimately, parameters in these relations can and should be expressed as functions of material constituent properties and microstructure attributes.

Finally, it is useful to point out that the goal of this chapter is to illustrate the relative importance of two dominate microstructural aspects on the SDT process. This work is among the first to quantify the relative effects of grains and voids using an Eulerian framework. While only the detonation behavior of pressed HMX is studied here, the effects of binder and additives in composite PBXs are still a main focus of the energetics community. The SDT probability study presented here can be expanded to other energetic compositions in the future.

CHAPTER 6. THREE-DIMENSIONAL MICROSTRUCTURE-EXPLICIT AND VOID-EXPLICIT MESOSCALE SIMULATIONS OF DETONATION OF HMX AT MILLIMETER SAMPLE SIZE SCALE

This chapter is based on work in collaboration with Daniel Olsen.

6.1 Introduction

This chapter presents fully three dimensional (3D) microstructure-explicit (ME) and void-explicit (VE) mesoscale models at the millimeter scale (ME-VE-MM-MS) for pressed granular HEs under shock loading. Both material microstructures and voids are explicitly resolved. The overall size scale of the models are up to 3×3×15 millimeters, large enough to resolve the full process from onset of loading to eventual SDT with the detonation front propagating in the remaining un-shocked part of the material. At the largest size scale, the samples have ~30,000 grains and ~206,265 voids. Each simulation can require over 2 days (50 hours) on over 1,400 computing cores on supercomputers at the DoD Supercomputing Resource Centers (DSRCs). The processes captured include thermal-mechanical response, hotspot development, reaction initiation, formation of a detonation front, and the SDT. In the calculations carried out, the particular material of choice is HMX (Octahydro-1,3,5,7-tetranitro-1,3,5,7-tetrazocine). Four model cases are considered: homogenous material with no microstructure or voids, material with a granular microstructure but no voids, material with voids but no microstructure, and material with both voids and granular microstructure. Shocking loading is generated by an aluminum flyer thick enough to

maintain continuous loading on the HMX sample without unloading. The focus of the analyses is on the SDT process and the run-to-detonation-distance (RDD), rather than the details of local fields in the material. Statistically equivalent microstructure sample sets (SEMSS) for the heterogeneous cases are used, allowing probabilistic quantification of the Pop plot (PP) and statistically significant assessment of the rank order of the influences of different material factors (microstructure, voids, and combinations thereof). The results from 2D and fully 3D simulations are compared to outline their potential differences and highlight factors that should be addressed in the future for more systematic comparisons and assessment of the multi-dimensional models.

The quantification of the probabilistic nature or uncertainties of the Pop plots uses the statistical approach first proposed by Wei et al. [173] for ignition thresholds and later expanded upon in Chapter 5 of this thesis to Pop plots. This analysis results in the generation of probabilistic Pop plots along with analytical relations. These relations can also be used to determine the necessary shock pressure, RDD, or SDT probability given any two of the three quantities. Although the material of focus is HMX, the models, the approach, and the analytical relations developed are applicable to PBX and other energetic materials.

6.2 Framework of Analysis

The 3D simulations are carried out using CTH, the Sandia National Labs solid mechanics code. Sustained loading is effected on the sample via the use of a thick aluminum flyer with velocities varying from 600 m/s to 1200 m/s, resulting in shock pressures between 4 and 8 GPa. In section 6.2.1, the method for generating 3D statistically

equivalent microstructure sample sets (SEMSS) is discussed. An outline of the constitutive models used is given in section 5.2.2. The results of mesh convergence and sample size effects are discussed in section 5.2.4.

6.2.1 Material, Model and Microstructure

In order to accurately quantify the effects of microstructure heterogeneities on the detonation behavior, we consider four types of samples: homogenous (H), microstructured without voids (M), homogenous with voids (V), and microstructured with voids (M+V). A microstructured sample and the corresponding void distribution are shown in Figure 60. The homogeneous (H) and microstructured (M) samples are fully-dense (100% TMD). The voids in the V and M+V samples are spheres and have diameters of 50 μm. This void size is chosen to allow explicit resolution of each void in the 3×3×15 mm samples without making the computational time prohibitively expensive. Depending on the shock intensity, each run can require up to 50 hours using 1,400 cores on a supercomputer. Further discussions on mesh size and computational cost are in section 5.2.4.

A set of five random but statistically similar microstructures is generated using Voronoi tessellation. These samples conform to the statistical grain size distribution in Figure 61. This monomodal distribution has a mean grain diameter of 164.7 μm. This method of microstructure generation results in reasonably realistic, randomized, and statistically equivalent microstructure sample sets (SEMSS). For the homogenous or microstructured samples with voids, the individual voids are inserted randomly until a total void volume fraction of 10% has been reached or an average void density of 1528/mm^3. For the 3×3×15 mm samples, this porosity level corresponds to 206,265 voids in each

sample. No two voids overlap, ensuring a constant void size and random void distribution. For visual clarity, only 5% of all the voids are shown in Figure 60(b).

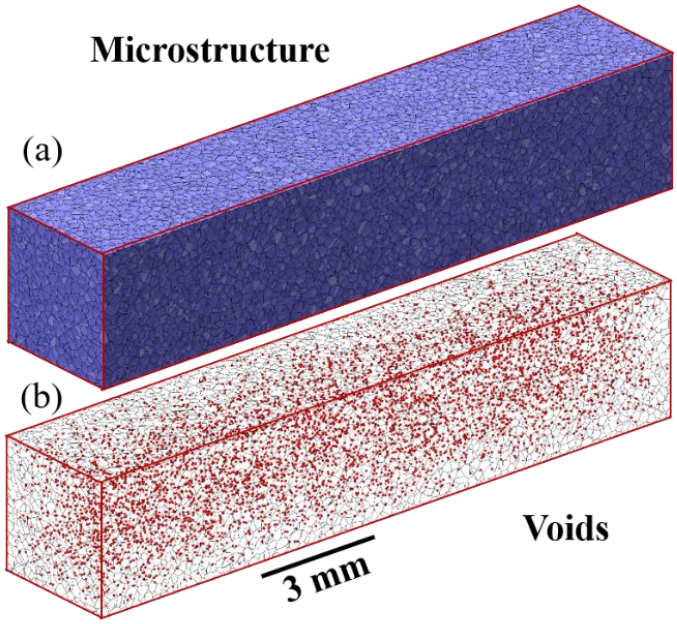

Figure 60 -(a) Three-dimensional microstructure of a sample in the microstructured (M) material case generated by Voronoi tessellation. The sample size is 3×3×15 mm. (b) A random void distribution in the V and V+M cases. The void volume fraction considered is 10% and each void is a sphere with a diameter of 50 μm. The total number of grains is 29,093 in the model shown. The total number of voids is 206,265, giving rise to a void density of 1528/mm^3. Only 5% of the voids are actually illustrated in (b) for visual clarity.

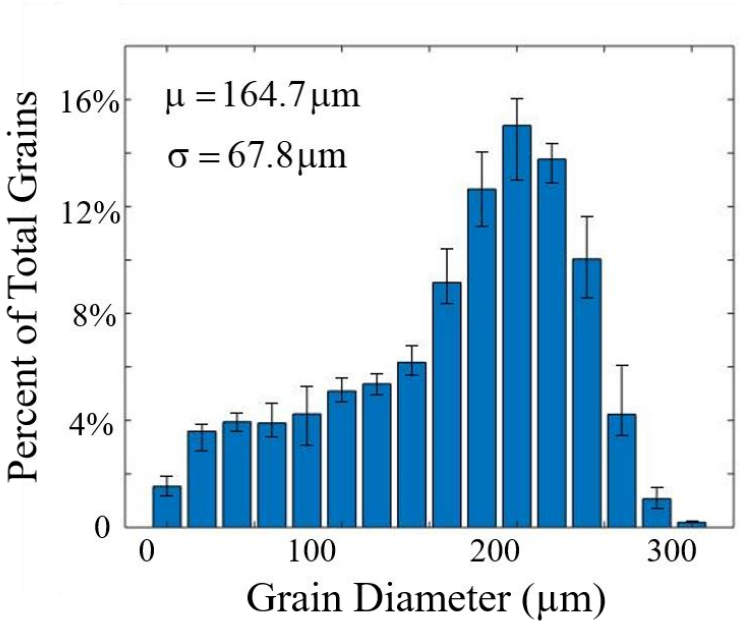

Figure 61 - Monomodal HMX grain size distribution in the statistically equivalent microstrucutre sample sets of the M and M+V material cases.

Actual samples in experiments have more heterogeneous characteristics than those in the four sets of samples presented here. For example, nano- and micro-scale voids, microcracks, and directionality of the material properties due to the anisotropic nature of the HMX crystal all play roles in the response of the materials to shock loading. These factors are too small, too complicated, or computationally expensive to be explicitly resolved in the current model setting. They are often ignored in many models reported in the literature. To account for the effects of these factors via grain-level heterogeneities, the density of the HMX for each grain is set to one of three possible values: 80% TMD (1.52 g/cm^3), 100% TMD (1.90 g/cm^3), and 120% TMD (2.28 g/cm^3). These density variations emulate the effects of local variations in the material and represent one source of variations in fields behind the shock front normally attributed to localized material heterogeneities. It is important to note that even though 120% TMD is a nonphysical description of a material,

this variation in density is used as a modeling tool to account for microstructural aspects not explicitly resolved in this study. It also allows the average density at the overall sample level and across multiple samples in a SEMSS to conform to the density of the material for samples without voids. Since the HVRB chemistry model used here (further detailed in section 6.2.2) is pressure-dependent (density-dependent), the density variations are a source of heterogeneous reaction behavior as well as mechano-thermal behaviors, as seen in experiments. In this study, the grains are assumed to be perfectly bonded to one another. If two grains with the same density are positioned next to one another, they behaves as a single grain of the same density. For the H and V samples, the standard HMX 100% TMD (1.90 g/cm^3) is used.

The present framework represents a simplified approach toward explicitly resolving some important features in microstructures of common heterogeneous energetic materials (HEM). While the method of varying the density of the HMX grains may replicate the trends seen in experiments, it is difficult to fully quantify the effect of heterogeneities into a single parameter. Actual experimental samples have clear defects not accounted for here, which are known to contribute to hotspot initiation and subsequent detonation [20, 101, 166, 167]. Other HEMs may have binder and additive components, such as aluminum, which can affect the sensitivity of the material to ignition (as discussed in Chapter 4 of this thesis). It is entirely possible that microstructure heterogeneity plays an even larger role than what is presented in the results of this study. However, as one of the first 3D millimeter macroscale microstructure-explicit and void-explicit modeling approaches, the current framework should be regarded as a step toward fully accounting for the most essential material heterogeneities using mesoscale models.

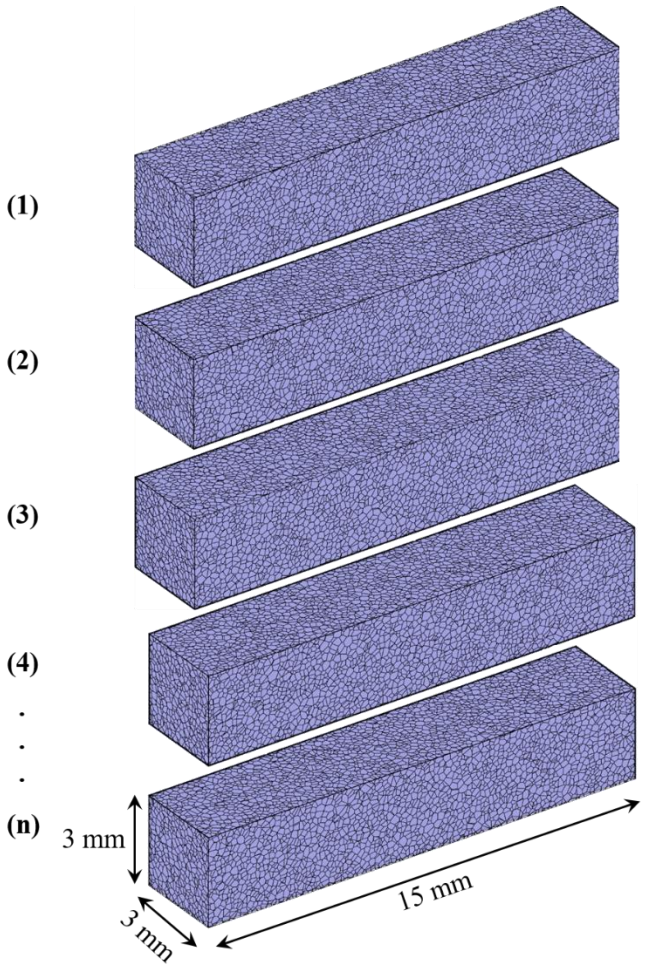

Figure 62 - Statistically equivalent microstructure sample set (SEMSS) for the M and M+V material cases.

6.2.2 Constitutive Relations

The computational analysis is performed using CTH, a multi-material, Eulerian solid mechanics simulation platform developed at Sandia National Laboratories. The constitutive models used are the same as used in Chapter 5, so only a brief summary will

be provided here. The full descriptions of each of these constitutive models are described in Chapter 2.3. The specimen is initially stress-free and at rest. A thick aluminum flyer impacts the sample at velocity (U_p) to generate sustained shock loading for the duration of the simulation. The side (lateral) boundaries are constrained in a frictionless manner to maintain the overall conditions of macroscopic sample-level uniaxial strain typical of planar impact experiments. The coupled mechanical, thermal, and chemical events in the samples are fully three-dimensional, along with the ME and VE material model.

A simplified Steinberg-Guinan-Lund strain-dependent flow stress model (SGL) is used to account for the viscoplastic constitutive behavior of HMX. This strain-rate dependent model is well-suited for high strain-rate deformation and accounts for the effects of thermal softening. The model has been calibrated to match the elasto-viscoplastic model used for HMX in Chapters 3 and 4 of this thesis, which in turn was based on available experimental data. The bulk response to hydrostatic pressure is modeled using the first order Mie–Grüneisen EOS and the effects of chemical reaction initiation and progression are described using the history variable reactive burn model (HVRB). Reactive burn models have been widely used to simulate the ignition and detonation of HEMs [14, 83, 84]. These empirical models are often calibrated to Pop plot data. As a result, the localized extent of reaction behind the shock front may not be perfectly resolved (which is a known limitation for the HVRB model). However, with available data and models, this is a reasonable trade-off in order to reach the macroscale from the mesoscale, since the focus here is on analyzing macroscale material behavior, rather than fine details of local fields.

6.2.3 Mesh and Size Convergence

To ensure accurate results for the analysis of the RDD (quantity of interest or QoI), a mesh convergence study is carried out to determine the proper mesh size necessary to explicitly resolve both the grains and voids and to ensure convergence of the QoI. To this end, shock pressure and RDD are calculated for samples including both microstructure and voids (M+V) at mesh sizes ranging from 30 μm to 5 μm. The M+V sample set was chosen for this purpose because it accounts for both types of heterogeneities and therefore poses the most stringent requirement for resolution. As shown in Figure 63, a mesh resolution of 15 μm is sufficient to reach convergence for the shock pressure, with further mesh refinement down to 5 μm resulting in relative fluctuations of ~1.2%. For the RDD, convergence is observed for mesh sizes finer than 10 μm, with further refinement down to 5 μm resulting in relative fluctuations of ~1.5%. For both the pressure and RDD, the further refinement does not lead to a specific trend (increase or decrease). For this reason, a mesh size of 10 μm is chosen for all subsequent production calculations. At the resolution of 10 μm, a 3×3×15 mm sample has 1.35×10^{8} volumetric elements; at a resolution of 5 μm, the same sample has 1.08×10^{9} elements. The computational savings are significant. It is important to note that this study is focused on the macroscale detonation behaviors of the materials, not on details of local fields, as is the case in many other studies. A finer mesh resolution would likely be required to accurately resolve local temperatures and pressures. Such local analyses may also appropriately call for the use of an Arrhenius-type chemical reaction rate model, as is commonly the case for small-scale simulations [70, 170, 174, 175]. The HVRB model used here (as outlined in section 6.2.2) is a simplified, pressure-dependent chemistry model that does not require direct use of local temperature or account

for specific chemical species. It is understandable that a coarser mesh can be used for the study of macroscale parameters such as the run distance because macroscale responses and events reflect the aggregate effects of local fluctuations at lower scales.

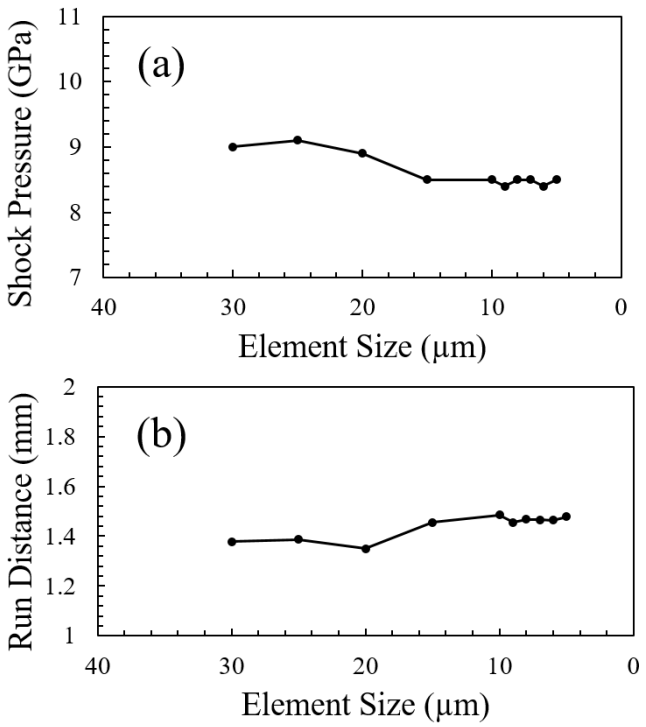

Figure 63 - (a) Shock pressure and (b) run distance to detonation (RDD) for a sample with microstructure and voids (M+V) at mesh resolutions ranging from 30 μm to 5 μm.

In addition to the mesh resolution study, an analysis is also carried out on the sample size effects so as to ensure a sufficiently large representative volume element (RVE) for the material while potentially minimizing computational cost. Here, while the smallest microstructure features (voids) dictate the necessary mesh resolution, the largest microstructure features (grains) and the length scale of the SDT process (the run distance

to detonation) dictate the necessary RVE size of the sample. As such, in addition to the 3×3×15 mm sample size, smaller sizes are also considered. Note that for the pressure range of interest (4-8 GPa), the run distance to detonation is within 6 mm. Therefore, two smaller sample sizes, 2×2×6 mm and 1×1×6 mm, are used. The run distance to detonation is calculated for five separate shock intensities, the results show strong agreement among all the sizes, indicating that the smaller sample sizes are acceptable. To minimize computational cost without significant loss of accuracy, the remaining calculations are carried out using a sample size of 1×1×6 mm.

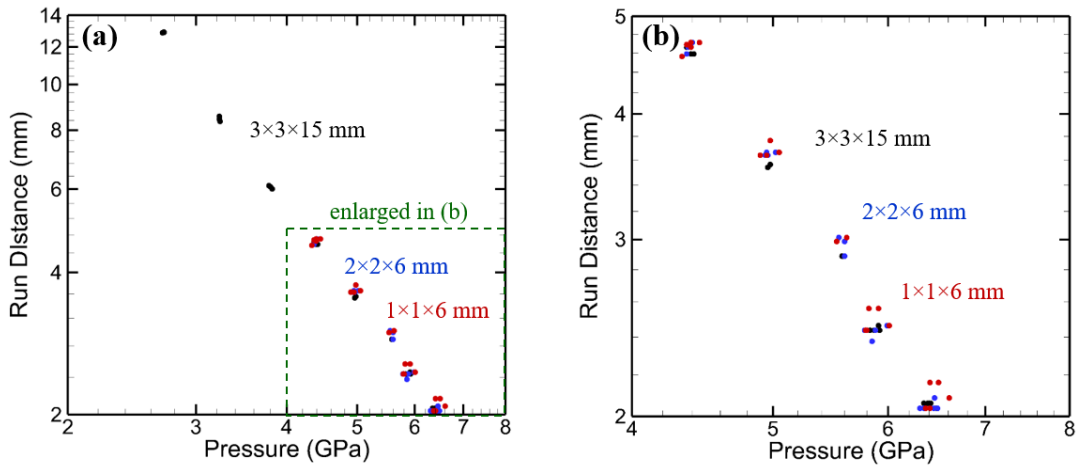

Figure 64 - (a) Run distance to detonation (RDD) as a function of shock pressure (Pop plot) for the microstructured material case (M) for three different sample sizes: 3×3×15 mm, 2×2×6 mm, and 1×1×6 mm. (b) An enlarged portion of the plot in (a).

6.3 Results

A systematic quantification of the effect of the microstructure and voids on the SDT behavior and Pop plot of pressed HMX is carried out. Section 6.3.1 discusses how the shock pressure and run distance are determined for each sample. Section 6.3.2 discusses

the effects of microstructure and voids on the Pop plot for 3D samples. Section 6.3.3 compares the results between 3D and equivalent 2D samples. Finally, Sections 6.3.4 and 6.3.5 present a thorough statistical framework which may be used to predict detonation behavior over the entire range of shock pressures.

6.3.1 Determination of Shock Pressure and Run Distance

The RDD is a performance metric used to measure the SDT sensitivity and performance of energetic materials. In this analysis, the RDD is defined as the longitudinal distance the shock wave travels in the sample when the detonation wave front is fully formed and transitions into propagation in undeformed material.

The relationship between the RDD and the pressure of the imposed shock loading (shock pressure), or the Pop plot, is both material-dependent and microstructure-dependent. This relation can be used to compare the relative performances of different materials and identify microstructure effect trends. In the analysis here, the relations are used to quantify the differences in performance due to microstructure and voids of the four HMX cases described earlier. To determine the shock pressure in each simulation, the pressure profile along the entire length of the sample is calculated by averaging the pressures on cross-sections that are perpendicular to the loading direction. The plateau of this profile starting from the impact face is measured and used to obtain an average over both sample distance and time. This allows the most accurate assessment of the shock pressure. To calculate the run distance, the location of the shock front in the sample is recorded as a function of time. Since the detonation wave propagates faster than the inert shock wave, the run distance is easily measured by examining the sharp change in the

propagation velocity of the shock front. The pressure fields showing shock front locations at four different times of one sample with microstructure and voids (M+V) at an impact of $U_{\mathrm{P}} = 1000\,\mathrm{m/s}$ are shown in Figure 65. The time histories of pressure at nine spatial locations for this sample are shown in Figure 66.

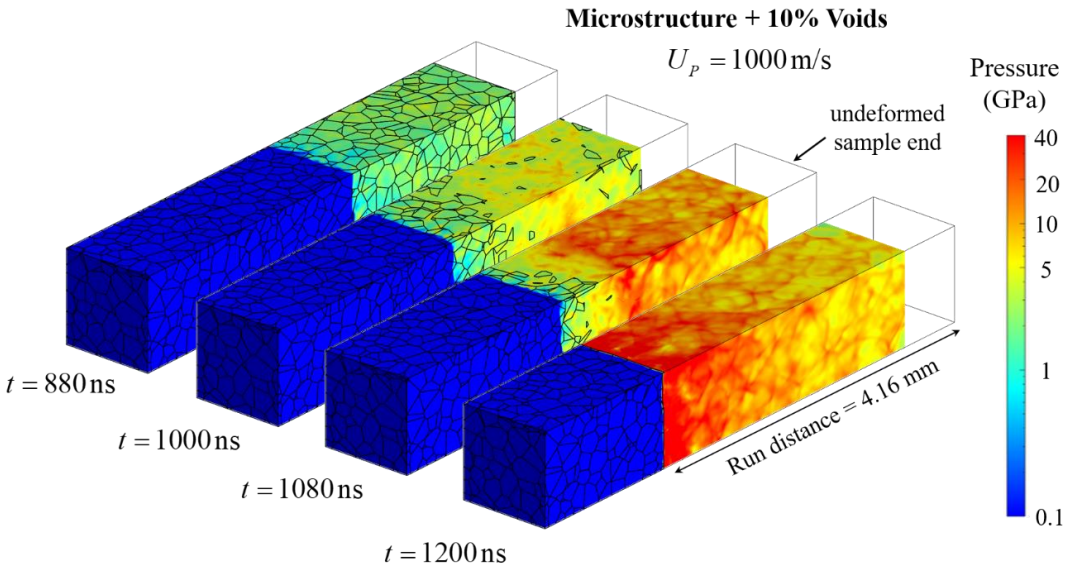

Figure 65 - The shock-to-detonation process in a HMX sample containing both microstructure and voids (10% by volume). The pressure fields are shown on the current (deformed) configurations. Shock loading is due to impact by a thick aluminum flyer at 1000 m/s. The resulting run distance to detonation is 4.16 mm.

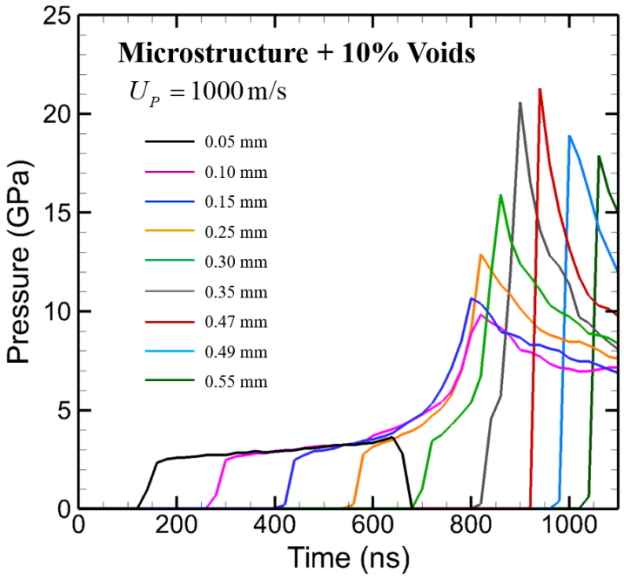

Figure 66 - Time history of pressure at nine locations during the SDT process shown in Figure 65. Each line represents the average pressure on the cross section perpendicular to the impact direction at a given distance from the impact face.

6.3.2 Effects of Microstructure and Voids in 3D

In this section, the effects of microstructure heterogeneities are quantified and rank-ordered. The four types of samples described earlier: homogeneous (H), homogeneous with only voids (V), microstructured (M), and microstructured with voids (M+V), are analyzed. A SEMSS with five samples for each of the heterogeneous cases (V, M, and M+V) are used in the analyses. The primary focus is on the effects of the heterogeneities on the Pop plot for 3D samples. For comparison, companion 2D cases for each material case are also analyzed with a corresponding SEMSS. The 2D and 3D SEMSS sets have generally matching attributes in terms of grain size, grain size distribution, void size, and void volume fraction. The 2D and 3D results are compared at the end of this section. While the

2D simulations are similar to the results presented in Chapter 5, the 2D simulations here are new calculations whose microstructural parameters have been tailored to match that of the 3D samples.

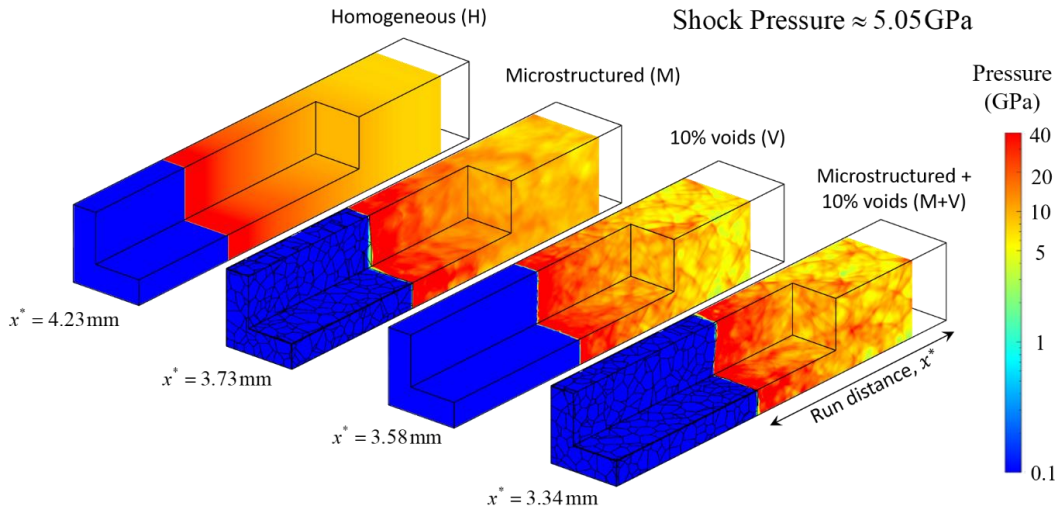

Figure 67 - Run-to-detonation distance (RDD) comparison for a sample of each material case under similar pressures. For visual clarity, a cutout of each sample has been removed to show the detonation process in the interior.

Impact loading is effected by a thick aluminum flyer traveling at velocities ranging from 600 m/s to 1200 m/s, resulting in shock pressures ranging from 4 to 8 GPa. A single visual comparison of each of the cases is shown in Figure 67 and the Pop plot (relation between the RDD and the shock pressure) for the cases analyzed is shown in Figure 68. Shorter run distances under a given shock pressure suggest higher impact sensitivity and more rapid SDT. It is desirable to not only rank-order the Pop plot lines for different material cases, but also to quantify the effects of the underlining material mesoscopic factors – microstructure and voids. Also, because of uncertainties or statistical variations

resulting from mesoscopic material heterogeneities, the quantification should account for the probabilistic nature of the results. The plot shows both the RDD data sets for the four SEMSS and the Pop plot lines that represent the “average” RDD-shock pressure relation for each material case. More specifically, these “average” lines represent the RDD-shock pressure conditions corresponding to a 50% probability of observing SDT. The SDT probability is greater than 50% above the “average” line for a material and less than 50% below the line. For the cases considered, the rank order of the four “average” or 50% lines from the lowest to the highest SDT sensitivity (longest to shortest RDD at the same shock pressure) is: homogeneous (H), microstructured (M), homegenous with voids (V), and microstructures with voids (M+V). To quantified the differences, the average percentage vertical distance between 50% line for the homegenous (H) case and that for each of the other three cases is calcualted and listed in Table 21.

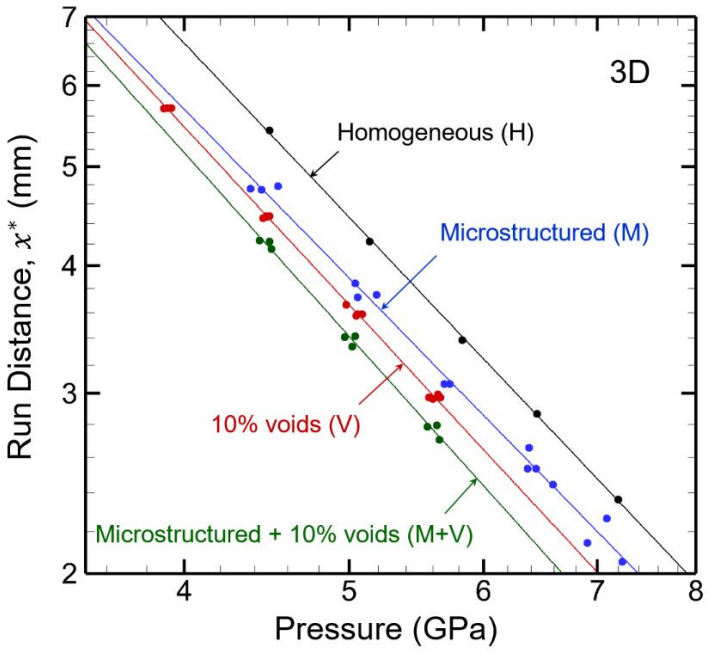

Figure 68 - Run distance to detonation (RDD) as a function of shock pressure (Pop plot) for the four material cases analyzed using 3D simulations. The data sets are: homogeneous (H, black), microstructured (M, blue), homogeneous with 10% voids by volume (V, red), and microstructured with10% voids (M+V, green). The line for each data set (or material case) represents the average trend or the conditions for a 50% probability of SDT. The probability of SDT is higher than 50% above the line and lower than 50% below the line.

Table 21. Effect of material heterogeneities on normalized run distance for 3D samples

SEMSS	Average decrease in RDD relative to H
Homogenous (H)	0%
Microstructured (M)	12.2%
Homogeneous with 10% voids (V)	18.2%
Microstructured with 10% voids (M+V)	24.3%

Clearly, the introduction of heterogeneities (microstructure, voids) increases the SDT sensitivity (shifting the Pop plot data sets and Pop plot lines to the lower left in the RDD-pressure space) of the material over the shock pressure regime analyzed. Relative to the homogeneous case, the introduction of 10% voids decreases the average run distance by 18.6%, while the microstructured case on average has a RDD that is 12.5% lower than that of the homogeneous case. The material with both microstructure and voids is the most sensitive, with RDDs that are on average 24.1% lower than those of the homogeneous case. Several processes are at play here. The microstructure heterogeneities cause highly inhomogeneous stress and strain fields, thereby giving rise to inhomogeneous and localized temperature rises. Voids lead to sharp spikes in stresses, strains, and temperature via severe distortion and collapse. The result is the development of hot spots. Note that the levels of these effects are only reflective of the level of material heterogeneities and size scale of the voids considered here.

6.3.3 2D-3D Pop plot comparison

Since most simulations hitherto are carried out in 2D, there is naturally an interest in understanding the potential differences between the two types of models. Three-dimensional models not only can resolve the full 3D nature of the material microstructure and void distributions but also resolve an additional dimension and level of complexity in the evolution of the thermal, mechanical, and chemical fields. In contrast, 2D models involve more simplifications. Full understanding and quantification of the relations between the two require much more detailed study than what is possible in this chapter. Nevertheless, a preliminary analysis is conducted here to gain a look at the issue and

illustrate the need for more such analyses. While many factors are at play, the approach here involves generating 2D microstructures sample sets (SEMSS) with statistical attributes that are similar to those of the 3D SEMSS already analyzed. As mentioned previously, the 2D simulations carried out here are based on the work presented in Chapter 5, but are also independent of the results in Chapter 5. The 2D microstructures used in Chapter 5 and Chapter 6 are unique from each other. The "matching" 2D samples used here are 1×6 mm in size and have an average grain size distributions shown in Figure 69 and the same void diameter (50 μm) and void volume fraction (10%). By matching the attributes, we hope to focus on the effects of the additional dimensionality on the material behavior. The same four materials cases as in 3D are considered: homogeneous (H), microstructured without voids (M), homogeneous with voids (V), and microstructured with voids (M+V). The resulting Pop plot from the 2D simulations are shown in Figure 70, and the average decrease in the normalized run distance relative to the homogenous case is listed in Table 22.

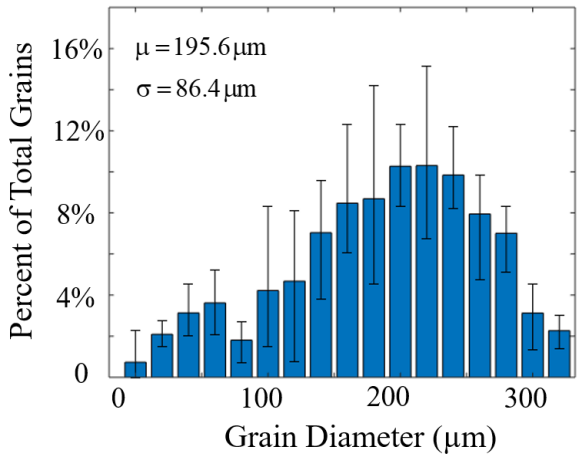

Figure 69 - Monomodal HMX grain size distribution in the statisically equivlaent microstrucutre sample sets of the 2D M and M+V material cases.

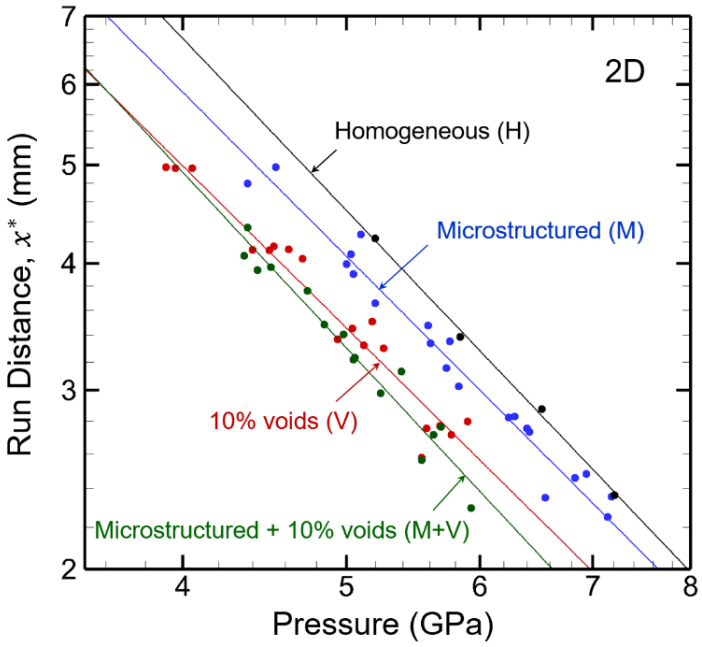

Figure 70 - Run distance to detonation (RDD) as a function of shock pressure (Pop plot) for the four material cases analyzed using 2D simulations.

Table 22. Effect of material heterogeneities on normalized run distance for 2D samples

SEMSS	Average Decrease in Run Distance
Homogeneous (H)	0%
Microstructured (M)	10.1%
10% Voids (V)	22.9%
Microstructured with 10% voids (M+V)	27.2%

There are noticeable differences between the 3D and 2D results (Figure 68 and Figure 70 respectively) in the heterogeneous (V, M, and M+V) cases, as seen in Figure 71, while the homogenous (H) case results are essentially the same in 3D and 2D as expected. For the M case, the 3D RDDs that are shorter than the corresponding 2D RDDs. For the V and the M+V cases, the trend is the opposite overall, with significant overlap in the data sets. In all three inhomogeneous material cases, the 2D data sets appear to have wider scatter of the data points than the corresponding 3D data sets. The differences here partly highlight the complexities in comparing 2D and 3D models. One important issue is that representing fundamentally three-dimensional material microstructures using 2D models invariably leaves out factors that cannot be captured, as 3D is more complex than 2D. As one example, uniformly sized spherical voids (or solid spheres for that matter) appear as circles of various diameters on 2D cross-sections through the material, as the voids are intercepted by the cross-section at different off-center locations, resulting in an extra degree of variation. The same is true for grains or particles. How should 2D representations be developed is a question that needs to be carefully addressed. One potential answer is to use direct cross-sections of the 3D samples. However, the average size and size distributions of grains and voids would not be the same as those in the original material. The objective

of this discussion here is not to provide answers for the questions, but rather to illustrate the challenges in comparison 2D and 3D models and bring to attention the need for further analyses.

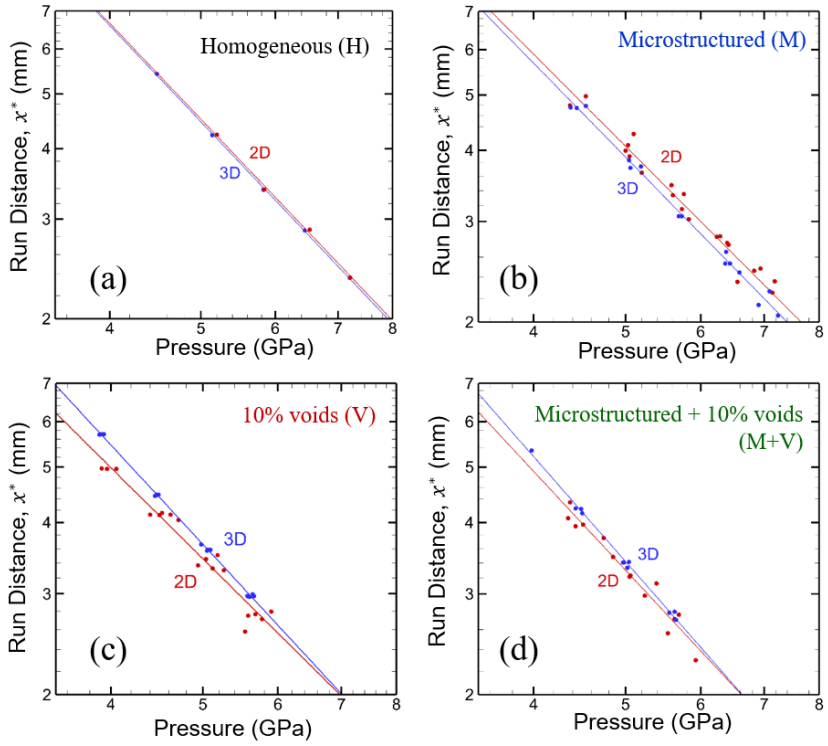

Figure 71 - Comparison of the Pop plots obtained from 2D and 3D simulations. (a) Homogenous (H), (b) Microstructured (M), (c) Homogenous with 10% voids (V), and (d) Microstructured with 10% voids (M+V).

6.3.4 Quantification of Stochasticity in Material Response

To quantify the statistical variations in the Pop plot results, a probabilistic formulation is required. To this end, we introduce a non-dimensional measure in the form of

$$D = \frac{\left(P_s - P_0\right)^m \left(x^* - x_0^*\right)}{S}, \tag{51}$$

where S is a material-dependent scaling parameter, m is a material-dependent exponent, x^* is the run distance, and P_s is the shock pressure. P_0 is the shock pressure below wich no SDT occurs, and x_0^* is the minimum run distance for observing SDT. These quantities should be regarded as material-dependent parameters which constitute bounds for P_s and x^*, respectively. This relationship was first proposed in Chapter 5 to fully recognize the probabilistic nature of the Pop plot. When D =1, Eq. (51) reduces to a standard power law, which is commonly used to fit data in the pressure-run distance space [29]. This line of best fit corresponds to the physical space where the SDT is likely to be observed in 50% of samples. The non-dimensional D can be considered as the Pop plot number (PPN) which allows the quantification of the probability of observing SDT above or below the "mean" Pop plot line of D =1. Specifically, D >1 and D <1 correspond to conditions for attaining SDT at greater than 50% and less than 50% probabilities, respectively. In order to connect the PPN to a specific probability, a log-normal cumulative distribution function (CDF) is fit to the data set for each material case (H, V, M, and M+V). Since the mean value of D is known or set as unit by definition here, the only remaining parameter in the log-normal distribution to determine via the fit for each material case is the standard deviation σ_d. The results for the 2D and 3D data sets are shown in Figure 72.

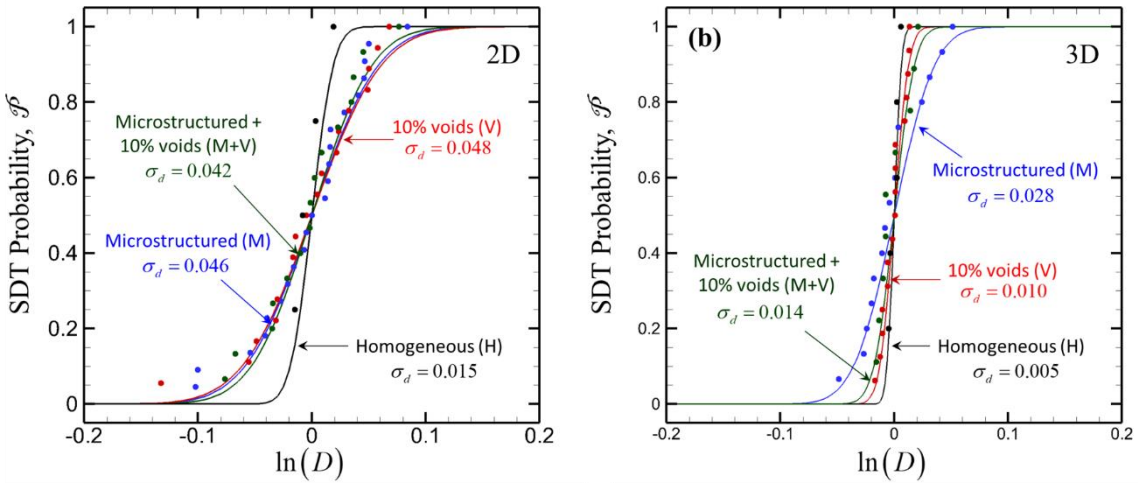

Figure 72 - Cumulative SDT probability obtained from (a) 2D and (b) 3D simulations. The lines are fits to the log-normal cumulative distribution function for the sample sets of the four material cases. The D parameter is computed for each data point using Eq. (51)

Once σ_d has been calculated for each data set, the corresponding probability map can be generated using

$$\mathcal{P}(P_s, x^*) = \frac{1}{2} + \frac{1}{2}\,\mathrm{erf}\left[\frac{1}{\sqrt{2}\sigma_d}\left(\ln\left(\left(P_s - P_0\right)^m\right) + \ln\left(x^* - x_0^*\right) - \ln S\right)\right]. \qquad (52)$$

The relation in Eq. (52) is strictly a slightly modified log-normal CDF where the PPN is treated as the independent variable. A full derivation of this equation can be found in Chapter 5.3.3.

The material parameters σ_d, S, and m for the four materials cases in both 2D and 3D are shown in Table 23. The conditions for which P_0 and x_0^* are relevant are outside the pressure regime of 4-8 GPa analyzed here. Accurate determination of values of P_0 and x_0^*

requires separate experimental data or threshold SDT analyses which are not carried out here. The fitting process shows that their values are low for the data sets here, therefore for D =1, Eq. (52) essentially approximates the power law for the traditional Pop plot line in Reference [29]. However, the form of Eq. (52) allows data sets to be more accurately determined whenever the relevant threshold data is made available by experiments or separate computations.

Table 23. Material parameters for the probabilistic relation in Eq. (52)

Dimensionality	Material case	σ_d	S	m
3D	Homogeneous (H)	0.013	69.3	1.78
3D	Microstructured (M)	0.028	60.0	1.70
3D	Homogeneous with 10% voids (V)	0.010	66.4	1.85
3D	Microstructured with 10% voids (M+V)	0.015	67.5	1.94
2D	Homogeneous (H)	0.015	77.8	1.82
2D	Microstructured (M)	0.046	56.7	1.64
2D	Homogeneous with 10% voids (V)	0.048	45.5	1.60
2D	Microstructured with 10% voids (M+V)	0.042	54.5	1.74

With Eq. (52), the SDT probability in the entire shock pressure vs. RDD space is mapped for each material case. The probability maps for the 2D results are shown in Figure 73, and the maps for the 3D results are shown in Figure 74. These figures (and Table 23) show that microstructure is the primary source of stochasticity in the Pop plot, i.e., the microstructured case (M) has the highest standard deviation. On the other hand, voids tend to significantly increase the standard deviation in 2D and only slightly increase the standard deviation in 3D. While much more systematic analyses are needed to explain why, one conjecture is that 3D samples involve many more voids than the 2D samples thereby "smooths" out some of the fluctuations in behavior.

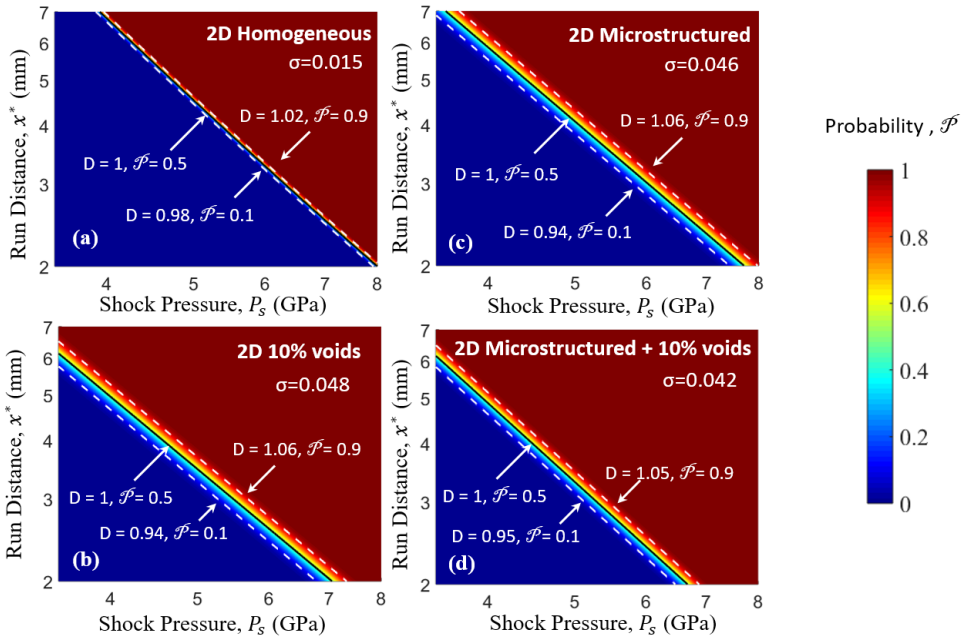

Figure 73 - SDT probability distribution maps for the four material cases obtained using 2D simulations: (a) homogeneous, (b) homogenous with 10% voids, (c) microstructures without voids, and (d) microstructured with 10 % voids.

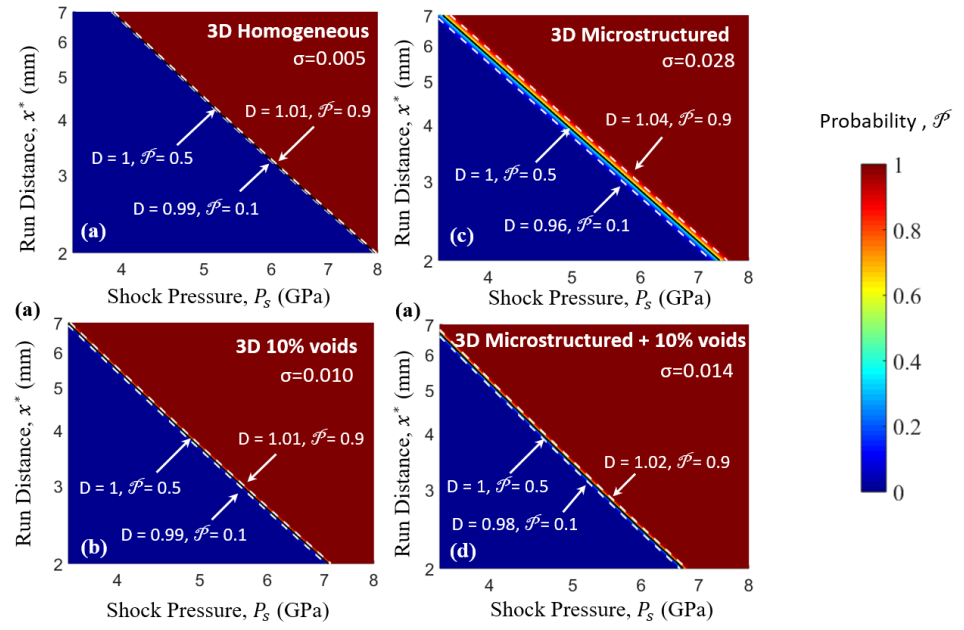

Figure 74 - SDT probability distribution maps for the four material cases obtained using 3D simulations: (a) homogeneous, (b) homogenous with 10% voids, (c) microstructures without voids, and (d) microstructured with 10% voids.

The probability maps shown here are a useful tool for examining the effects of microstructure heterogeneity on detonation behavior. Equation (52) allows the probability for observing SDT at a given run distance under shock loading with a given pressure. Often, it is also desirable to determine the shock pressure required or the minimum run distance necessary to ensure a desired probability of observing SDT. To find the answers to these questions, Eq. (52) can be rearranged to express $\mathscr{P}$ as function of P_s or x^*, and x^* as a function of P_s and $\mathscr{P}$, i.e.,

$$P_s(\mathscr{P}, x^*) = \left\{ \frac{S}{\left(x^* - x_0^*\right)} \exp\left[\sqrt{2}\sigma_d \left(\text{erf}^{-1}\left(2\mathscr{P} - 1\right)\right)\right] \right\}^{1/m} + P_0, \tag{53}$$

$$x^*(\mathscr{P}, P_s) = \frac{S}{\left(P_s - P_0\right)^m} \exp\left[\sqrt{2}\sigma_d \left(\text{erf}^{-1}\left(2\mathscr{P} - 1\right)\right)\right] + x_0^*. \tag{54}$$

These relations are previously derived in Chapter 5.3.3 and can be used to generate corresponding maps which are not shown here.

6.3.5 Probabilistic rank order of Pop plot lines of different material cases

In Figure 68, and Figure 70, the statistical data sets for different material cases overlap, making the comparison of the run distances of different materials a probabilistic endeavor. More specifically because the statistical data sets overlap, questions such as “what is the likelihood that the run distance of a random “M+V” sample is shorter than the run distance of a random “M” sample?” is of great interest and can only be answered in a probabilistic

manner. Graphically, the 50-50% probability lines for the cases in Figure 68, and Figure 70 and quantitatively ranked in Tables IV and V only show how the average run distances compare over the entire range of shock pressure of interest. Here, a more general approach is presented that allows the run distances of two random samples of two different materials at any given shock pressure to be compared in a probabilistic manner.

To facilitate the discussion, the probability density function (PDF) distributions of the RDD in the $\mathcal{P}$ - x^* space for the microstructured (M) and microstructured with voids (M+V) material cases obtained from the 2D simulations are shown in Figure 75(a). For a given shock pressure P_s, the PDFs are illustrated in Figure 75 (b). The probabilistic comparison is carried out on such cross-sections for different P_s values over the range of interest.

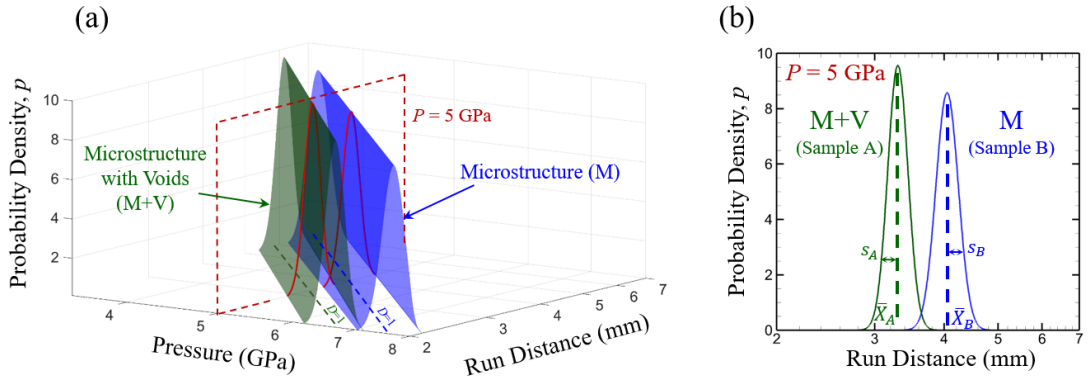

Figure 75 - (a) Probability density function (PDF) distributions of the RDD in the $\mathcal{P}$ - x^* space for the microstructured (M) and microstructured with voids (M+V) material cases obtained from the 2D simulations. The function values represent the probability of observing SDT at combinations of run distance and shock pressure. (b) A comparison of the PDFs at a shock pressure of 5 GPa. $\bar{X}$ and s represent the sample mean run distance and standard deviation at the given pressure, respectively.

Although the data sets in Figure 75 are for the M+V and M material cases, for the ease of discussion and generality, we will refer to these two cases as "A" and "B", respectively, in the formulas below because the approach described here is applicable to the comparison of any two different materials. At any given shock pressure P_s, the probability density *p* for each material as a function of x^* can be obtained from Eq. (52) as

$$p\left(x^*;P_s\right)=\frac{1}{x^* s\sqrt{2\pi}}\exp\left(-\frac{\left(\ln x^*-\ln X\right)^2}{2s^2}\right), \tag{55}$$

where

$$X\left(P_s\right)=\frac{H}{\left(P_s-P_0\right)^m}+x_0^*, \tag{56}$$

and

$$s\left(P_s\right)=\frac{H\sigma}{\left(P_s-P_0\right)^m}. \tag{57}$$

In the above relations, $\bar{X}$ is the mean and s is the standard deviation as illustrated in Figure 75(b). In this notation, the PDFs for *A* and *B* at P_s are denoted as $p_A\left(x^*;P_s\right)$ and $p_B\left(x^*;P_s\right)$, respectively. The probability of the RDD of *A* being shorter than the RDD of *B* for any given shock pressure P_s is

$$\mathscr{P}_{A<B}\left(P_s\right)=\int_0^\infty\left[p_{A<B}\left(x^*;P_s\right)\right]dx^*, \tag{58}$$

where $p_{A<B}\left(x^*;P_s\right)$ is the probability density of the RDD of a random sample in distribution A being lower than the RDD of a random sample in distribution B at x^*. This probability density can be evaluated via

$$p_{A<B}\left(x^*;P_s\right)=\left[\int_0^{x^*} p_A\left(x^*;P_s\right)dx^*\right]\cdot p_B\left(x^*;P_s\right), \tag{59}$$

where $\int_0^{x^*} p_A\left(x^*;P_s\right)dx^*$ is the probability of observing the RDD of a random sample in *A* being shorter than or equal to x^*. Since the maximum cumulative probability of any probability density function is unit by definition, $\int_0^{x^*} p_A\left(x^*;P_s\right)dx^*\le 1$ and, therefore $p_{A<B}\left(x^*;P_s\right)\le p_B\left(x^*;P_s\right)$. By the same token, $\int_0^{\infty} p_B\left(x^*;P_s\right)dx^*=1$ which means there exists an upper bound for $\int_0^{\infty}\left[p_{A<B}\left(x^*;P_s\right)\right]dx^*$ such that the $\mathscr{P}_{A<B}\left(P_s\right)$ evaluated via Eq. (58) satisfies

$$0\le\mathscr{P}_{A<B}\left(P_s\right)\le 1. \tag{60}$$

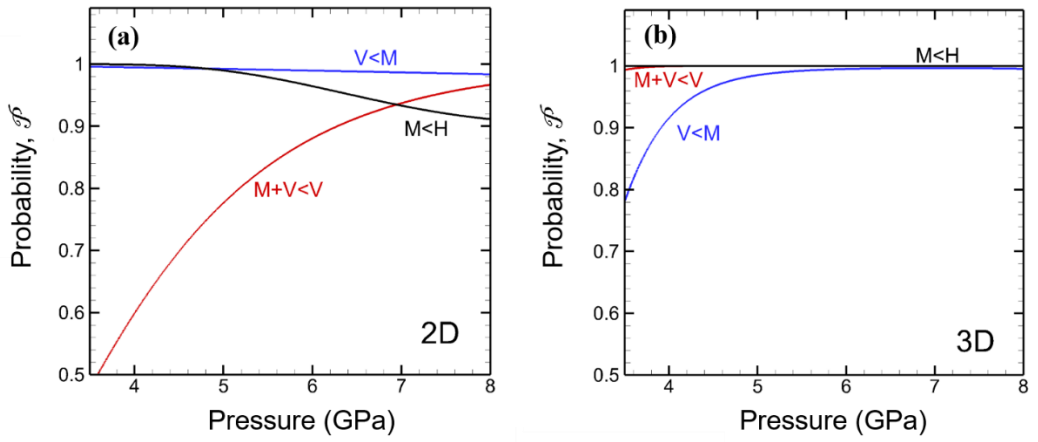

Figure 76 - Probability that: (1) M+V samples have a shorter RDD than V samples (red), (2) V samples have a shorter RDD than M samples (blue), and (3) M samples have a shorter RDD than H samples (black) as a function of shock pressure for (a) 2D and (b) 3D samples.

Equations (58) and (59) are used to compare the RDDs for the four material cases over the entire range of shock pressure studied. The confidence levels for the rank order of $x^*_{\mathrm{M+V}} < x^*_{\mathrm{V}} < x^*_{\mathrm{M}} < x^*_{\mathrm{H}}$ are shown in Figure 76 for both the 2D and the 3D simulations. In the case of the 2D simulations, the confidence level for the M+V samples resulting in shorter RDDs than the V samples increases as the shock pressure increases. In contrast, both the likelihoods for the M samples having shorter RDDs as compared to the H samples and the V samples as compared to the M samples decrease as the shock pressure increases. For the 3D simulations, the confidence level increases as the shock pressure increases for all three comparisons: $x^*_{\mathrm{M+V}} < x^*_{\mathrm{V}} < x^*_{\mathrm{M}} < x^*_{\mathrm{H}}$. Again, more systematic studies are required to explain why 2D and 3D simulations are different.

6.4 Conclusion

There is a long-standing interest in three-dimensional (3D) simulations of the behavior of energetic materials and in understanding potential differences between 2D and 3D simulations. While 2D simulations have been extensively carried out at the micron to tens-of-microns size scales, simulations at the millimeter scale explicitly accounting for microstructure and voids are rare. 3D simulations at the millimeter scale are equally sparse. Millimeter scale model sizes are important for two reasons. One is the need to have sufficient representative volume of the heterogeneous material microstructure, the other is the need to capture the entire process of shock loading, reaction initiation, onset of detonation, and the transition from shock to detonation – which occurs over distances of millimeters for most materials under shock pressures of several GPa. This chapter reports a first attempt at carrying out large-scale 3D simulations and corresponding 2D simulations. As such, simplifications or idealizations are involved, as is the case in most analyses. For example, nanoscale defects, additives, material anisotropy and crystalline behavior have not been considered here. While the material of focus is pressed HMX, the approach is applicable to other materials as well, including PBXs.

The fully dimensional (3D) mesoscale models presented here are microstructure-explicit and void-explicit for the simulations of the shock-to-detonation transition (SDT) process. The samples have overall sizes up to 3×3×15 millimeters. The material cases considered revolve around pressed granular HMX and are designed to allow systematic delineation of the effects of microstructure and voids. The analysis has focused on the effects of microstructure and voids on the run-to-detonation distance (RDD), a

macroscopic performance measure for HE. For comparison purposes, 2D simulations are also carried out to assess the differences between the 2D and 3D simulations. One feature of the analysis is the use of statistically equivalent microstructure sample sets (SEMSS) to establish statistical and probabilistic Pop plots (PP). Sample sets with different combinations of microstructure heterogeneities and voids allow the effects of microstructure and voids to be systematically delineated. The effects of both microstructure (heterogeneous grain size, morphology, and distribution) and voids on the RDD and the PP are quantified using a probabilistic formulation. This formulation is further used to rank order the influences of microstructure and voids, allowing confidence levels to be established in the assessments of the trends.

The 2D and 3D models yielded results that overall consistent with each other, but with significant differences. In general, the 2D simulations exhibit wider scatter of the RDD in all material cases as compared to the 3D simulations. The level of the RDD are also somewhat different. This comparison is preliminary, illustrates the complexities of the 2D vs. 3D issue, and points out the need for more systematic analyses in the future including more consistent generation of the 2D and 3D SEMSS.

The 3D simulations show that homogeneous HMX is the least sensitive (having the longest RDD or requiring the highest shock pressure for SDT initiation under otherwise identical conditions). Relative to the homogenous material, the average run distance of the heterogeneous microstructured material is 12.2% lower. On the other hand, the introduction of a 10% voids by volume to the homogeneous material causes the average run distance to decrease by 18.2%. The material with both microstructure and 10% voids

has the lowest average run distance which is 24.3% lower relative to that of the homogeneous material.

CHAPTER 7. SUMMARY AND FUTURE DIRECTIONS

7.1 Summary

The work presented in this thesis focuses on developing a better understanding of the role of microstructure in the ignition and detonation process of high explosives (HEs) during shock loading. As a shock wave propagates through an HE, material heterogeneities such as voids, cracks, additives, and grain morphology all contribute to energy dissipation in localized areas, thereby forming hotspots. These local temperature spikes serve as the initiation sites for chemistry in the material, and if enough hotspots coalesce prior to quenching, a detonation wave can form. This whole process is known as the shock to detonation transition (SDT), and understanding how mechanical dissipations influence the chemistry remains a long standing challenge of the energetics community at large. The work presented in this thesis serves to advance the greater understanding of the detonation process in HEs and contributes both new ideas and useful engineering tools to aid in the design process of future HEs.

Chapter 2 lays out the computational framework and capabilities for both the Cohesive Dynamics for Explosives (CODEX) and CTH codes used in Chapters 3-6. CODEX is a Lagrangian cohesive finite element method (CFEM) framework which accurately tracks the material response prior to the ignition of hotspots. Using CODEX, sample sensitivity is determined by monitoring critical hotspots, which occur due to localized energy dissipations resulting primarily from plastic and viscoelastic deformation, crack propagation, and friction. CTH is an Eulerian solid mechanics hydrocode developed

at Sandia National Laboratories which is able to track more extensive deformation, including the SDT at the cost of not being able to effectively track friction. Both of these frameworks are useful in studying the effects of microstructure and chemistry at different times in the detonation process.

Chapter 3 studies the microstructural effects on the ignition sensitivity of pressed HMX. Three sets of HMX microstructures are considered, each with a different average grain size: 220 μm, 130 μm, and 70 μm. Using CODEX, the ignition sensitivity of each material case is rank-ordered in E - Π space using the modified James relation presented in Eq. (25). It is found that decreasing the mean grain size of the pressed HMX leads to an increase in the sample sensitivity to ignition. This chapter also introduces a first of its kind statistical quantification of the results in E - Π space, which is used to derive a probabilistic formulation (Eq. (25)) of the likelihood of ignition. Using Eq. (25), the probability of ignition is mapped over the entire range of potential loading conditions. Finally, a new parameter, R, is introduced to provide a simple analysis for categorizing hotspots according to the proximity of their size-temperature state to the criticality condition. The approaches developed in this chapter provide useful engineering tools for the design and sensitivity evaluation of future HEs.

Chapter 4 applies a similar methodology developed in Chapter 3 to a mm scale PBX, containing HMX grains, an Estane binder, and aluminum (Al 7075) particulates. A set of statistically equivalent microstructure sample sets (SEMSS) are generated, and a shock loading is effected using a rigid flyer for various pulse durations. The volume fraction of the Estane binder is held constant at 19% while four different volume fractions

of aluminum are studied: 0%, 6%, 10%, and 18%. It is found that the ignition sensitivity of the PBX sample increase as the aluminum concentration increases, which is consistent with experimental results in the literature. The sensitivity analysis is carried out using both the High-James criterion in E - Π space and the Walker-Wasley criterion in $P - \tau$ space. The relative effects of frictional energy dissipation are compared to localized plastic work, and friction is shown to play a dominant role in the development of critical hotspots. Incorporating aluminum particulates causes cracks to appear between the aluminum and binder elements, which may otherwise occur as intragranular cracks in the HMX. Another study was conducted comparing the effects of two aluminum particle diameters: 50 μm and 100 μm. Smaller aluminum particles are found to further decrease the material sensitivity to ignition and the total energy dissipated by cracks in the aluminum is found to scale with the total aluminum particle surface area.

Chapter 5 returns to the study of pressed HMX in 2D, this time using the Eulerian framework CTH. The entire shock to detonation transition (SDT) is explicitly modeled using a history variable reactive burn model (HVRB), and the primary focus is on the effect of explicitly modeled voids and microstructure. Multiple SEMSS are impacted with a rigid flyer at varying velocities and the run distance to detonation (RDD) is calculated as a function of shock pressure to generate a Pop plot for the material. Initially, SDT simulations are carried out on samples containing an increasing volume fraction of voids (5%, 10%, and 20% voids), and the increased void concentration is found to lower the average run distance (as compared to the Homogeneous case) by 20.6%, 28.8%, and 37.2% respectively. To compare the relative effect of microstructure and voids, four material cases are generated and simulated under shock loading (Homogeneous (H), Microstructured (M),

Homogeneous with 5% voids (V), and Microstructured with 5% voids (M+V)). As more material heterogeneities are introduced the Pop plot line is found to decrease – indicating the sample is achieving its RDD in a shorter distance for similar shock pressures. Both microstructure and voids significantly affect the Pop plot and samples with only 5% voids are found to have a stronger effect than samples with only microstructure. Samples with both microstructure and voids (M+V) have the largest effect. A probabilistic analysis is developed, based on work initially carried out in Chapter 3, which maps the likelihood of observing SDT at any given shock pressure and RDD. This analysis is expanded to incorporate probability itself as a potential input to calculate either the RDD or pressure necessary to observe SDT given one or the other.

Chapter 6 develops a model for 3D simulations of pressed, granular HMX by expanding the computational framework previously employed in Chapter 5. The size scale of these simulations are 3×3×15 mm, with roughly 30,000 grains and over 200,000 voids. Four material cases are analyzed: Homogeneous (H), Microstructured (M), Homogeneous with 10% voids (V), and Microstructured with 10% voids (M+V). In addition, new statistically equivalent 2D cases are also run to have a reliable basis of comparison between 2D and 3D simulations. The 2D Pop plot results are found to have a much higher degree of scatter than their 3D counterparts, indicating that 3D simulations are necessary to capture true material behavior. A new statistical approach is formulated to illustrate a how the relative importance of each microstructural characteristic changes as a function of shock pressure. As the shock pressure increases, the importance of accounting for voids on top of microstructure alone also increases in the case of 3D simulations.

7.2 Suggestions for Future Directions

While the work presented here answers many questions posed by the energetics community, the overall role of microstructure and chemistry is still not fully understood. This part of the chapter outlines some questions that still remain unanswered, as well as ideas for potential ways to expand upon the framework of analysis presented in this thesis. While this dissertation serves as an important stepping stone to further the overall understanding of HE ignition and detonation, there are always improvements to be made.

To begin, the idea of an *R* parameter was introduced in Chapter 3 as a potential way to quantify subcritical hotspots within the material. It currently requires a significant number of runs to quantify *J* but only one to determine *R* for a single sample. Since the two parameters *J* and *R* are strongly correlated, the number of samples required to obtain the James type ignition threshold may be greatly reduced by analyzing the relationship between the *R* and *J* values. It would be of interest to study how the *R* quantification of the material affects predictions about the overall SDT transition as explored in Chapters 5 and 6. Finding new ways to reduce the computational time necessary to statistically quantify material would be a major improvement, and could lead to even faster microstructural characterization in the future.

The scope of void effect in this thesis did not consider void size – rather a single diameter of 50 μm diameter voids were used. This void size is far larger than are typically seen in experimental samples, but was a necessary tradeoff in order to fully study the effect of voids at mm length scales. Further studies should be carried out, accounting for more complete representations of material microstructure heterogeneities, including a range of

void size, void volume fraction, and void morphologies. Additionally, two separate computational frameworks were used: a Lagrangian one to study the frictional effects, and an Eulerian one to study the void effect. Ultimately, an approach is needed that can account for both of these mechanisms simultaneously, as they have both been shown to strongly affect the ignition sensitivity of the material.

In Chapter 6, a preliminary comparison between 2D and 3D SDT simulations was performed, however the 2D microstructures were generated independently from the 3D samples. To better draw conclusions on the true effect of dimensionality, including resulting data scatter effects, 2D simulations of actual 3D cross sections should be run. This will require some careful planning, as a single "slice" of the 3D sample will be unlikely to have the same grain and void distributions as the overall 3D sample. 3D simulations are computationally intensive, and any further work to identify just how necessary (or unnecessary) they are to accurately model energetic material behavior will be vastly appreciated by the shock physics community at large.

This thesis uses the pressure-dependent History Variable Reactive Burn (HVRB) model to track the evolution of chemistry in the shocked sample. While this model is widely used in the community, it is still an empirical model calibrated to match Pop plot results, not local fields. Due to this, transitioning to a more localized (although still empirical) Arrhenius-based chemical kinetics model may be desirable in order to better study the evolution of hotspots in CTH. Typically chemical-kinetics models require explicit tracking of the chemical species and have a reaction rate that evolves exponentially with temperature. This often requires an extremely fine computational time step in order to fully

resolve the chemistry. A simplified next step may involve transitioning the chemistry model to an Arrhenius Reactive Burn (ARB) model, which follows the overall reaction rate evolution model without explicitly tracking the product and reactant species. This intermediate step may lead to observing a more heterogeneous detonation than is seen in Chapters 5 and 6. Real HEs have been observed to have a heterogeneous wave front [9, 176, 177], and the HVRB still does not fully capture that effect, even though the macroscale run distance results are accurate.

Finally, the work in Chapters 3, 5, and 6 have focused on pressed HMX. While the microstructural analyses and probabilistic developments from these chapters were kept general, the next logical step is to apply the conclusions here to more PBX explicit models. In addition, several other phenomena are of interest to the community which were not studied in this work. These include analyzing the effects of PBX aging, ignition sensitivity to vibration, and the transition from deflagration to detonation at low impact velocities, among others. While many of these questions may not be answered in the immediate future, they provide a good direction to expand upon the contributions made in this thesis.

APPENDIX A. DERIVATION OF EQUIVALENT JAMES RELATION

Walker and Wasley [53] introduced a shock initiation threshold based on the critical energy input of

$$E_{cr} = \frac{m_{fly} V_{fly}^2}{2}, \tag{A-1}$$

where m_{fly} and V_{fly} are the mass and velocity of the flyer, respectively. For simplicity, assuming the impedance of the flyer is the same as the impedence of the sample, they used the following substitutions of variables.

$$\left.\begin{aligned} & m_{fly} = Aw\rho_{fly}, \quad \tau = \frac{2w}{c_{fly}}, \\ & V_{fly} = 2U_p, \text{ and } U_p = \frac{P}{\rho_{fly} c_{fly}} \end{aligned}\right\} \tag{A-2}$$

where A is area, w is thickness, ρ_{fly} is the density of the flyer, and c_{fly} is the speed of the stress wave in the flyer. The pressure in the sample and flyer is denoted by P. Plugging the variables in Eqs. (A-2) into Eq. (A-1) yields

$$P^2\tau = \mu \frac{E_{cr}}{A} = const., \tag{A-3}$$

where μ is the impedance of the flyer ($\mu = \rho_{fly} c_{fly}$) which is assumed to be a constant. James [54] converted the P –τ relation to the Σ – τ relation in the form of

$$\Sigma = \frac{1}{2}U_p^2 = \frac{E_c}{2\mu\tau}, \tag{A-4}$$

where E_c is critical energy fluence ($E_c = E_{cr}/A$) and Σ is specific kinetic energy ($\Sigma = 0.5U_p^2$). To achieve a better representation of experimental data at low flyer velocities, James added an additional asymptotic line, denoted by Σ_c, which gives

$$\Sigma = \frac{E_c}{2\mu\tau} + \Sigma_c . \tag{A-5}$$

Since $E = PU_p\,\tau$, Eq. (A-5) can be represented as

$$1 = \frac{E_c}{E} + \frac{\Sigma_c}{\Sigma}. \tag{A-6}$$

Welle et al. [13] replaced the specific kinetic energy ($\Sigma = 0.5U_p^2$) by the power flux ($\Pi = PU_p$) to give

$$1 = \frac{E_c}{E} + \frac{\Pi_c}{\Pi}. \tag{A-7}$$

Since the power flux ($\Pi = PU_p$) is the rate of energy imparted to the material ($\Pi = dE/dt$), we can eliminate the energy fluence and recast Eq. (A-7) in the Π - τ space as

$$\Pi = \Pi_c \cdot \left(1 + \frac{E_c/\Pi_c}{\tau}\right). \tag{A-8}$$

REFERENCES

1. Bourne, N.K. and G.T. Gray, *Dynamic response of binders; teflon, estane™ and Kel-F-800™.* Journal of Applied Physics, 2005. **98**(12): p. 123503.

2. Campbell, A.W. and J.R. Travis. *Shock desensitization of PBX-9404 and Composition B-3*. in *8th International Detonation Conference*. 1985. Albuquerque, NM.

3. Provatas, A., *Energetic polymers and plasticisers for explosive formulations-A review of recent advances*. 2000, DEFENCE SCIENCE AND TECHNOLOGY ORGANISATION MELBOURNE (AUSTRALIA).

4. Cooper, J., et al., *Explosive composition*. 2018, Google Patents.

5. Campbell, A.W., et al., *Shock Initiation of Solid Explosives.* Physics of Fluids, 1961. **4**(4): p. 511-521.

6. Gustavsen, R.L., S.A. Sheffield, and R.R. Alcon, *Measurements of shock initiation in the tri-amino-tri-nitro-benzene based explosive PBX 9502: Wave forms from embedded gauges and comparison of four different material lots.* Journal of Applied Physics, 2006. **99**(11): p. 114907.

7. Campbell, A.W., W.C. Davis, and J.R. Travis, *Shock Initiation of Detonation in Liquid Explosives.* Physics of Fluids, 1961. **4**(4): p. 498-510.

8. Sheffield, S.A., et al., *Shock initiation and detonation study on high concentration H2O2/H2O solutions using in-situ magnetic gauges*. 2010, Los Alamos National Lab.(LANL), Los Alamos, NM (United States).

9. Johansson, C.H. and P.-A. Persson, *Detonics of high explosives*. 1970: Academic Press.

10. Mader, C.L., *Numerical modeling of explosives and propellants*. 2nd ed. 1998: CRC press.

11. Johnson, J.N., P.K. Tang, and C.A. Forest, *Shock-wave initiation of heterogeneous reactive solids.* Journal of Applied Physics, 1985. **57**(9): p. 4323-4334.

12. Bowden, F.P. and A.D. Yoffe, *Initiation and growth of explosion in liquids and solids*. 1952: Cambridge University Press.

13. Welle, E.J., et al., *Microstructural effects on the ignition behavior of HMX*. Journal of Physics: Conference Series, 2014. **500**(5): p. 052049.

14. Baer, M.R., *Modeling heterogeneous energetic materials at the mesoscale.* Thermochimica Acta, 2002. **384**(1-2): p. 351-367.

15. Mader, C.L., *Initiation of Detonation by the Interaction of Shocks with Density Discontinuities.* The Physics of Fluids, 1965. **8**(10): p. 1811-1816.

16. Austin, R.A., et al., *Direct numerical simulation of shear localization and decomposition reactions in shock-loaded HMX crystal.* Journal of Applied Physics, 2015. **117**(18): p. 185902.

17. Handley, C.A., et al., *Understanding the shock and detonation response of high explosives at the continuum and meso scales.* Applied Physics Reviews, 2018. **5**(1): p. 011303.

18. Rai, N.K. and H.S. Udaykumar, *Mesoscale simulation of reactive pressed energetic materials under shock loading.* Journal of Applied Physics, 2015. **118**(24): p. 245905.

19. Kim, S., et al., *Computational prediction of probabilistic ignition threshold of pressed granular octahydro-1,3,5,7-tetranitro-1,2,3,5-tetrazocine (HMX) under shock loading.* Journal of Applied Physics, 2016. **120**(11): p. 115902.

20. Kim, S., et al., *Prediction of shock initiation thresholds and ignition probability of polymer-bonded explosives using mesoscale simulations.* Journal of the Mechanics and Physics of Solids, 2018. **114**: p. 97-116.

21. Jackson, T.L., et al., *Multi-dimensional mesoscale simulations of detonation initiation in energetic materials with density-based kinetics.* Combustion Theory and Modelling, 2018. **22**(2): p. 291-315.

22. Wood, M.A., et al., *Multiscale modeling of shock wave localization in porous energetic material.* Physical Review B, 2018. **97**(1): p. 014109.

23. Yarrington, C.D., R.R. Wixom, and D.L. Damm, *Shock interactions with heterogeneous energetic materials.* Journal of Applied Physics, 2018. **123**(10): p. 105901.

24. Bennett, J.G., et al., *A constitutive model for the non-shock ignition and mechanical response of high explosives.* Journal of the Mechanics and Physics of Solids, 1998. **46**(12): p. 2303-2322.

25. Benson, D.J. and P. Conley, *Eulerian finite-element simulations of experimentally acquired HMX microstructures.* Modelling and Simulation in Materials Science and Engineering, 1999. **7**(3): p. 333-354.

26. Rao, P.T. and K.A. Gonthier. *Analysis of Dissipation Induced by Successive Planar Shock Loading of Granular Explosive*. in *51st AIAA/SAE/ASEE Joint Propulsion Conference*. 2015. Orlando, FL.

27. Field, J.E., et al., *Hot-Spot Ignition Mechanisms for Explosives and Propellants.* Philosophical Transactions of the Royal Society of London Series a-Mathematical Physical and Engineering Sciences, 1992. **339**(1654): p. 269-283.

28. Tarver, C.M., S.K. Chidester, and A.L. Nichols, *Critical conditions for impact- and shock-induced hot spots in solid explosives.* Journal of Physical Chemistry, 1996. **100**(14): p. 5794-5799.

29. Ramsay, J. and A. Popolato, *Analysis of shock wave and initiation data for solid explosives*. 1965, Los Alamos Scientific Lab., Univ. of California, N. Mex.

30. Bourne, N. and A. Milne, *The temperature of a shock-collapsed cavity.* Proceedings of the Royal Society of London. Series A: Mathematical, Physical and Engineering Sciences, 2003. **459**(2036): p. 1851-1861.

31. Bourne, N.K. and J.E. Field, *Explosive ignition by the collapse of cavities.* Proceedings of the Royal Society a-Mathematical Physical and Engineering Sciences, 1999. **455**(1987): p. 2411-2426.

32. Austin, R.A., et al., *Modeling pore collapse and chemical reactions in shock-loaded HMX crystals.* Journal of Physics: Conference Series, 2014. **500**(5): p. 052002.

33. Chidester, S., L. Green, and C. Lee, *A frictional work predictive method for the initiation of solid high explosives from low-pressure impacts*. 1993, Lawrence Livermore National Lab., CA (United States).

34. Chaudhri, M.M., *Photographic Evidence for Ignition by Friction in a Deflagrating Explosive Single-Crystal.* Journal of Physics D-Applied Physics, 1992. **25**(3): p. 552-557.

35. Browning, R.V. and R.J. Scammon, *Microstructural model of ignition for time varying loading conditions.* Shock Compression of Condensed Matter-2001, Pts 1 and 2, Proceedings, 2002. **620**: p. 987-990.

36. Gruau, C., et al., *Ignition of a confined high explosive under low velocity impact.* International Journal of Impact Engineering, 2009. **36**(4): p. 537-550.

37. Curtis, J.P., et al., *Modeling Violent Reaction Following Low Speed Impact on Confined Explosives.* Shock Compression of Condensed Matter - 2011, Pts 1 and 2, 2012. **1426**.

38. Barua, A., Y. Horie, and M. Zhou, *Energy localization in HMX-Estane polymer-bonded explosives during impact loading.* Journal of Applied Physics, 2012. **111**(5): p. 054902.

39. Barua, A., Y. Horie, and M. Zhou, *Microstructural level response of HMX–Estane polymer-bonded explosive under effects of transient stress waves.* Proceedings of

the Royal Society of London A: Mathematical, Physical and Engineering Sciences, 2012. **468**(2147): p. 3725-3744.

40. Barua, A. and M. Zhou, *Computational analysis of temperature rises in microstructures of HMX-Estane PBXs.* Computational Mechanics, 2013. **52**(1): p. 151-159.

41. Czerski, H. and W.G. Proud, *Relationship between the morphology of granular cyclotrimethylene-trinitramine and its shock sensitivity.* Journal of Applied Physics, 2007. **102**(11).

42. Bardenhagen, S.G., et al., *Detailed Characterization of Pbx Morphology for Mesoscale Simulations.* Shock Compression of Condensed Matter - 2011, Pts 1 and 2, 2012. **1426**.

43. Burnside, N.J., et al. *Particle characterization of pressed granular HMX*. in *Shock Compression of Condensed Matter*. 1997. AIP Conference Proceedings.

44. Swallowe, G. and J. Field. *Effect of polymers on the drop-weight sensitiveness of explosives*. in *7th Symp. on Detonation*. 1981.

45. Rimoli, J.J., E. Gürses, and M. Ortiz, *Shock-induced subgrain microstructures as possible homogenous sources of hot spots and initiation sites in energetic polycrystals.* Physical Review B, 2010. **81**(1): p. 014112.

46. Bowden, F.P. and A.D. Yoffe, *Fast reactions in solids*. 1958: Butterworths Scientific Publications.

47. Semenov, N.N., *Chemical Kinetics and Chain Reactions*. 1935: Oxford University Press, London.

48. Frank-Kamenetskii, D.A., Zhurnal Fizicheskoi Khimii, 1939. **13**.

49. Thomas, P.H., *On the Thermal Conduction Equation for Self-Heating Materials with Surface Cooling.* Transactions of the Faraday Society, 1958. **54**(1): p. 60-65.

50. Boddington, T., et al., *Thermal Explosions with Extensive Reactant Consumption - a New Criterion for Criticality.* Proceedings of the Royal Society of London Series a-Mathematical Physical and Engineering Sciences, 1983. **390**(1798): p. 13-30.

51. Tarver, C.M. and T.D. Tran, *Thermal decomposition models for HMX-based plastic bonded explosives.* Combustion and Flame, 2004. **137**(1-2): p. 50-62.

52. Henson, B.F., et al., *Ignition chemistry in HMX from thermal explosion to detonation.* Shock Compression of Condensed Matter-2001, Pts 1 and 2, Proceedings, 2002. **620**: p. 1069-1072.

53. Walker, F.E. and R.J. Wasley, *Critical Energy for Shock Initiation of Heterogeneous Explosives.* Explosivstoffe, 1969. **17**: p. 9-13.

54. James, H.R., *An extension to the critical energy criterion used to predict shock initiation thresholds.* Propellants Explosives Pyrotechnics, 1996. **21**(1): p. 8-13.

55. Roth, G., *Performance of explosives*. 1900: German Patent No. 173327

56. Vadhe, P.P., et al., *Cast aluminized explosives.* Combustion Explosion and ShockWaves, 2008. **44**(4): p. 461-477.

57. Grishkin, A.M., et al., *Effect of Powdered Aluminum Additives on the Detonation Parameters of High Explosives.* Combustion Explosion and Shock Waves, 1993. **29**(2): p. 239-245.

58. Akhavan, J., *The Chemistry of Explosives*. 2004, Cambridge: The Royal Society of Chemistry.

59. Gogulya, M.F., A.Y. Dolgoborodov, and M.A. Brazhnikov, *Fine structure of detonation waves in HMX-Al mixtures.* Chemical Physics Reports, 1998. **17**(1-2): p. 51-54.

60. Antić, G. and V. Džingalašević, *Characteristics of cast PBX with aluminium.* Scientific Technical Review, 2006. **56**(3-4): p. 52-58.

61. Dlott, D.D., *New Developments in the Physical Chemistry of Shock Compression.* Annual Review of Physical Chemistry, Vol 62, 2011. **62**: p. 575-597.

62. VonNeumann, J. and R.D. Richtmyer, *A Method for the Numerical Calculation of Hydrodynamic Shocks.* Journal of Applied Physics, 1950. **21**(3): p. 232-237.

63. Bowers, R.L. and J.R. Wilson, *Numerical modeling in applied physics and astrophysics*. 1991: Jones and Bartlett Publishers.

64. Segletes, S.B., *Thermodynamic stability of the Mie–Grüneisen equation of state, and its relevance to hydrocode computations.* Journal of Applied Physics, 1991. **70**(5): p. 2489-2499.

65. Ahrens, T.J., D.L. Anderson, and A.E. Ringwood, *Equations of state and crystal structures of high-pressure phases of shocked silicates and oxides.* Reviews of Geophysics, 1969. **7**(4): p. 667-707.

66. Dattelbaum, D.M. and L.L. Stevens, *Chap 4. Equations of State of Binders and Related Polymers,* in *Static Compression of Energetic Materials,* S.M. Peiris and G.J. Piermarini, Editors. 2008, Springer: Virginia, USA. p. 127-202.

67. Jouguet, E., *On the propagation of chemical reactions in gases.* J. de mathematiques Pures et Appliquees, 1905. **1**(347-425): p. 2.

68. Davison, L., *Fundamentals of Shock Wave Propagation in Solids (Chap. 13)*. Shock Wave and High Pressure Phenomena, ed. L. Davison and Y. Horie. 2008: Springer Berlin Heidelberg.

69. Horie, Y., *Hot Spots, High Explosives Ignition, and Material Microstructure*. Materials Science Forum, 2014. **767**: p. 3-12.

70. Laidler, K.J., *The development of the Arrhenius equation.* Journal of Chemical Education, 1984. **61**(6): p. 494.

71. Springer, H.K., et al., *Investigating short-pulse shock initiation in HMX-based explosives with reactive meso-scale simulations.* Journal of Physics: Conference Series, 2014. **500**(5): p. 052041.

72. Tarver, C. and C. May. *Short pulse shock initiation experiments and modeling on LX-16, LX-10, and ultrafine TATB.* in *Fourteenth International Detonation Symposium*. 2010.

73. Zhan, C.-G. and D.A. Dixon, *A Density Functional Theory Approach to the Development of Q− e Parameters for the Prediction of Reactivity in Free-Radical Copolymerizations.* The Journal of Physical Chemistry A, 2002. **106**(43): p. 10311-10325.

74. Tarver, C., *Chemical energy release in self-sustaining detonation waves in condensed explosives.* Combustion and Flame, 1982. **46**: p. 157-176.

75. Mader, C.L., *Two dimensional homogeneous and heterogeneous detonation wave propagation*. 1976, Los Alamos Scientific Lab., N. Mex.(USA).

76. Cady, H.H., A.C. Larson, and D.T. Cromer, *The crystal structure of alpha-HMX and a refinement of the structure of beta-HMX.* Acta Cryst., 1963. **16**: p. 617-623.

77. Karpowicz, R.J. and T. Brill, *The beta to delta transformation of HMX-Its thermal analysis and relationship to propellants.* Aiaa Journal, 1982. **20**(11): p. 1586-1591.

78. Sorescu, D.C., B.M. Rice, and D.L. Thompson, *Theoretical studies of the hydrostatic compression of RDX, HMX, HNIW, and PETN crystals.* The Journal of Physical Chemistry B, 1999. **103**(32): p. 6783-6790.

79. Kimura, J. and N. Kubota, *Thermal decomposition process of HMX*. Propellants, Explosives, Pyrotechnics, 1980. **5**(1): p. 1-8.

80. Farber, M. and R. Srivastava, *Mass spectrometric investigation of the thermal decomposition of RDX.* Chemical Physics Letters, 1979. **64**(2): p. 307-310.

81. Kishore, K., *Thermal Decomposition Studies on Hexahydro-1, 3, 5-trinitro-s-triazine (RDX) by differential scanning calorimetry.* Propellants, Explosives, Pyrotechnics, 1977. **2**(4): p. 78-81.

82. McGuire, R. and C. Tarver, *Chemical-decomposition models for the thermal explosion of confined HMX, TATB, RDX, and TNT explosives*. 1981, Lawrence Livermore National Lab., CA (USA).

83. Lee, E.L. and C.M. Tarver, *Phenomenological model of shock initiation in heterogeneous explosives.* Physics of Fluids, 1980. **23**(12): p. 2362-2372.

84. Menikoff, R. and M.S. Shaw, *Reactive burn models and ignition & growth concept.* New Models and Hydrocodes for Shock Wave Processes in Condensed Matter, 2010. **10**.

85. Menikoff, R. and M.S. Shaw, *Review of the Forest fire model for high explosives.* Combustion Theory and Modelling, 2008. **12**(3): p. 569-604.

86. Hertel, E., et al., *CTH: A software family for multi-dimensional shock physics analysis*, in *Shock Waves@ Marseille I*. 1995, Springer. p. 377-382.

87. McGlaun, J.M., S.L. Thompson, and M.G. Elrick, *CTH: A three-dimensional shock wave physics code.* International Journal of Impact Engineering, 1990. **10**(1): p. 351-360.

88. S. K. Chidester, K.S.V., C. M. Tarver, *Shock Initiation of Damaged Explosives*. 2009, LLNL.

89. Tarver, C.M., *Chemical Kinetic Modeling of HMX and TATB Laser Ignition Tests.* Journal of Energetic Materials, 2004. **22**(2): p. 93-107.

90. Nichols III, A.L. and C.M. Tarver. *A statistical hot spot reactive flow model for shock initiation and detonation of solid high explosives*. in *Twelfth International Symposium on Detonation, Office of Naval Research, San Diego, CA*. 2002.

91. Tarver, C.M., *Effects of Chemical Energy-Release on Detonation-Waves in Condensed Explosives.* Bulletin of the American Physical Society, 1979. **24**(4): p. 713-713.

92. Massoni, J., et al., *A mechanistic model for shock initiation of solid explosives.* Physics of Fluids, 1999. **11**(3): p. 710-736.

93. Kapila, A., et al., *Two-phase modeling of deflagration-to-detonation transition in granular materials: Reduced equations.* Physics of fluids, 2001. **13**(10): p. 3002-3024.

94. Fried, L.E., et al., *LLNL CHEETAH Code*.

95. Barua, A. and M. Zhou, *A Lagrangian framework for analyzing microstructural level response of polymer-bonded explosives.* Modelling and Simulation in Materials Science and Engineering, 2011. **19**(5): p. 055001.

96. Barua, A., et al., *Ignition criterion for heterogeneous energetic materials based on hotspot size-temperature threshold.* Journal of Applied Physics, 2013. **113**(6): p. 064906.

97. Kapahi, A. and H.S. Udaykumar, *Three-dimensional simulations of dynamics of void collapse in energetic materials.* Shock Waves, 2015. **25**(2): p. 177-187.

98. Rai, N.K., *Numerical Framework for Mesoscale Simulation of Heterogeneous Energetic Materials*, in *Mechanical Engineering*. 2015, University of Iowa. p. 173.

99. Lambrecht, M.R., et al., *Electromagnetic modeling of hot-wire detonators.* IEEE Transactions on Microwave Theory and Techniques, 2009. **57**(7): p. 1707-1713.

100. Fried, L.E., et al. *The role of viscosity in TATB hot spot ignition*. in *AIP Conference Proceedings*. 2012. AIP.

101. Wei, Y., et al., *Quantification of probabilistic ignition thresholds of polymer-bonded explosives with microstructure defects.* Journal of Applied Physics, 2018. **124**(16): p. 165110.

102. Rai, N.K., M.J. Schmidt, and H.S. Udaykumar, *High-resolution simulations of cylindrical void collapse in energetic materials: Effect of primary and secondary collapse on initiation thresholds.* Physical Review Fluids, 2017. **2**(4): p. 043202.

103. Baer, M., M. Kipp, and F.v. Swol, *Micromechanical modeling of heterogeneous energetic materials*. 1998, Sandia National Labs., Albuquerque, NM (United States).

104. Reaugh, J., *Grain-scale dynamics in explosives Lawrence Livermore National Laboratory Tech. Rep*. 2002, UCRL-ID-150388-2002.

105. Rai, N.K. and H. Udaykumar, *Three-dimensional simulations of void collapse in energetic materials.* Physical Review Fluids, 2018. **3**(3): p. 033201.

106. Gresshoff, M. and C.A. Hrousis. *Probabilistic Shock Threshold Criterion*. in *14th International Detonation Symposium*. 2010. Coeur d'Alene, ID.

107. Nichols III, A.L. *Statistical hot spot model for explosive detonation*. in *AIP Conference Proceedings*. 2006. AIP.

108. Schwarz, A.C., *Study of factors which influence the shock-initiation sensitivity of hexanitrostilbene (HNS)*. 1981, Sandia National Laboratories: Albuquerque, NM USA. p. 16.

109. Yan-Qing, W. and H. Feng-Lei, *A micromechanical model for predicting combined damage of particles and interface debonding in PBX explosives.* Mechanics of Materials, 2009. **41**(1): p. 27-47.

110. Barua, A., et al., *Prediction of probabilistic ignition behavior of polymer-bonded explosives from microstructural stochasticity.* Journal of Applied Physics, 2013. **113**(18): p. 184907.

111. Zhou, M., A. Needleman, and R.J. Clifton, *Finite-Element Simulations of Shear Localization in Plate Impact.* Journal of the Mechanics and Physics of Solids, 1994. **42**(3): p. 423-458.

112. Kim, S., Y. Horie, and M. Zhou, *Ignition Desensitization of PBX via Aluminization.* Metallurgical and Materials Transactions A, 2015. **46**(10): p. 4578-4586.

113. Gump, J.C. and S.M. Peiris, *Isothermal equations of state of beta octahydro-1,3,5,7-tetranitro-1,3,5,7-tetrazocine at high temperatures.* Journal of Applied Physics, 2005. **97**(5): p. 053513.

114. Yoo, C.-S. and H. Cynn, *Equation of state, phase transition, decomposition of beta-HMX (octahydro-1,3,5,7-tetranitro-1,3,5,7-tetrazocine) at high pressures.* The Journal of Chemical Physics, 1999. **111**(22): p. 10229-10235.

115. Landerville, A.C., et al., *Equations of state for energetic materials from density functional theory with van der Waals, thermal, and zero-point energy corrections.* Applied Physics Letters, 2010. **97**(25): p. 251908.

116. Marsh, S.P., *LASL Shock Hugoniot data. Los Alamos series on dynamic material properties.* University of California, Berkeley, CA, 1980.

117. Mas, E.M., et al., *A Viscoelastic Model for PBX Binders.* AIP Conference Proceedings, 2002. **620**: p. 661-664.

118. Zhai, J., V. Tomar, and M. Zhou, *Micromechanical simulation of dynamic fracture using the cohesive finite element method.* Journal of Engineering Materials and Technology, 2004. **126**(2): p. 179-191.

119. Bourago, N.G., *A Survey on Contact Algorithms.* Proc. Int. Workshop on Grid Generation and Industrial Applications, 2002: p. pp. 42-59.

120. Hardin, D.B., *The Role of Viscoplasticity in the Deformation and Ignition Response of Polymer Bonded Explosives*, in *Mechanical Engineering*. 2015, Georgia Institute of Technology.

121. Kerley, G.I., *CTH equation of state package: porosity and reactive burn models.* Sandia National Laboratories report SAND92-0553, 1992.

122. Schmitt, R., et al., *CTH user's manual and input instructions version 11.2.* CTH Development Project, Sandia National Laboratories, Albuquerque, NM, 2016.

123. Solov'ev, V.S., *Some specific features of shock-wave initiation of explosives.* Combustion Explosion and Shock Waves, 2000. **36**(6): p. 734-744.

124. Molek, C.D., et al. *Microstructural Characterization of Pressed HMX Material Sets at Differing Densities*. in *APS SCCM-2015*. In press. Tampa, FL.

125. Wixom, R.R., et al., *Characterization of pore morphology in molecular crystal explosives by focused ion-beam nanotomography*. Journal of Materials Research, 2010. **25**(7): p. 1362-1370.

126. Yang, X., T. Zhou, and C. Chen, *Effective elastic modulus and atomic stress concentration of single crystal nano-plate with void.* Computational Materials Science, 2007. **40**(1): p. 51-56.

127. Hudson, R.J., *Investigating the factors influencing RDX shock sensitivity*, in *Applied Science and Engineering*. 2012, Cranfield University.

128. Hudson, R.J., P. Zioupos, and P.P. Gill, *Investigating the Mechanical Properties of RDX Crystals Using Nano-Indentation.* Propellants, Explosives, Pyrotechnics, 2012. **37**(2): p. 191-197.

129. Sewell, T.D., et al., *A molecular dynamics simulation study of elastic properties of HMX*. The Journal of Chemical Physics, 2003. **119**(14): p. 7417-7426.

130. Dimas, L.S., et al., *Random Bulk Properties of Heterogeneous Rectangular Blocks With Lognormal Young's Modulus: Effective Moduli.* Journal of Applied Mechanics, 2015. **82**(1): p. 011003-011003.

131. Liu, C., *On the minimum size of representative volume element: An experimental investigation.* Experimental Mechanics, 2005. **45**(3): p. 238-243.

132. May, C.M. and C.M. Tarver, *Modeling Short Shock Pulse Duration Initiation of LX-16 and LX-10 Charges*. AIP Conference Proceedings, 2009. **1195**(1): p. 275-278.

133. Green, L., A. Weston, and J. Van Velkinburg, *Mechanical and Frictional Behavior of Skid Test Hemispherical Billets*. 1971, California Univ., Livermore. Lawrence Livermore Lab.

134. Dickson, P.M., et al., *Frictional Heating and Ignition of Energetic Materials.* AIP Conference Proceedings, 2006. **845**(1): p. 1057-1060.

135. Barua, A., *Mesoscale computational prediction and quantification of thermomechanical ignition behavior of polymer-bonded explosives (PBXs)*, in *Mechanical Engineering*. 2013, Georgia Institute of Technology: Atlanta, GA.

136. von Neumann, J. and R.D. Richtmyer, *A Method for the Numerical Calculation of Hydrodynamic Shocks.* Journal of Applied Physics, 1950. **21**(3): p. 232-237.

137. Landshoff, R., *A numerical method for treating fluid flow in the presence of shocks*. 1955, DTIC Document.

138. Campbell, J. and R. Vignjevic, *Chap. 19 Artificial Viscosity Methods for Modelling Shock Wave Propagation*, in *Predictive Modeling of Dynamic Processes*. 2009, Springer. p. 349-365.

139. Benson, D.J., *Computational methods in Lagrangian and Eulerian hydrocodes.* Computer Methods in Applied Mechanics and Engineering, 1992. **99**(2–3): p. 235-394.

140. Simpson, R.L., F.H. Helm, and J.W. Kury, *Non-Reactive HMX Shock Hugoniot Data.* Propellants, Explosives, Pyrotechnics, 1993. **18**(3): p. 150-154.

141. James, H.R. and B.D. Lambourn, *On the systematics of particle velocity histories in the shock-to-detonation transition regime.* Journal of Applied Physics, 2006. **100**(8): p. 084906.

142. Merzhanov, A.G. and V.G. Abramov, *Thermal Explosion of Explosives and Propellants. A review.* Propellants, Explosives, Pyrotechnics, 1981. **6**(5): p. 130-148.

143. Lambourn, B.D., et al., *A simple model for the pressure field from a distribution of hotspots.* Journal of Physics: Conference Series, 2014. **500**(5): p. 052023.

144. Migault, A., *Concepts of Shock Waves*, in *Impacts on Earth*, D. Benest and C. Froeschlé, Editors. 1998, Springer Berlin Heidelberg. p. 79-112.

145. McMillan, A.R., W.M. Isbell, and A.H. Jones, *High Pressure Shock Wave Attenuation*. 1971, General Motors: Virginia.

146. Wall, C. and M. Franson, *Validation of a Pressed Pentolite Donor for the Large Scale Gap Test (LGST) at DSTO*. 2013, Defence Science and Technology Organisation: Department of Defense, Austrailia.

147. Khurana, R., et al., *Studies on Shock Attenuation in Plastic Materials and Applications in Detonation Wave Shaping.* Journal of Physics: Conference Series, 2012. **377**(1): p. 012051.

148. Welle, E.J., et al. *Microstructure effects on the initiation threshold behavior of HMX and PBXN-5*. in *15th International Detonation Symposium*. 2014.

149. Khasainov, B.A., et al., *On the effect of grain size on shock sensitivity of heterogeneous high explosives.* Shock Waves, 1997. **7**(2): p. 89-105.

150. Christensen, J.S., M. Gresshoff, and K.J. McMullen. *Probabilistic shock threshold development for LX-17*. in *15th International Detonation Symposium*. 2014.

151. Honodel, C., et al. *Shock initiation of TATB formulations*. in *Proceedings Seventh Symposium (International) on Detonation*. 1981. Annapolis, Maryland.

152. Schwarz, A.C. *Shock initiation sensitivity of hexanitrostilbene (HNS)*. in *Seventh Symposium (International) on Detonation*. 1981. Annapolis, Maryland (USA): Sandia National Labs.

153. Yarrington, C.D., et al., *Nano Aluminum Energetics: The Effect of Synthesis Method on Morphology and Combustion Performance.* Propellants Explosives Pyrotechnics, 2011. **36**(6): p. 551-557.

154. Sánchez, F., et al., *Relationship between particle size and manufacturing processing and sintered characteristics of iron powders.* Revista Latinoamericana de Metalurgia y Materiales, 2003. **23**(1): p. 35-40.

155. Miller, C., et al., *Ignition thresholds of aluminized HMX-based polymer-bonded explosives.* AIP Advances, 2019. **9**(4): p. 045103.

156. Prakash, V., et al., *Influence of aluminium on performance of HTPB-based aluminised PBXs.* Defence Science Journal, 2004. **54**(4): p. 475-482.

157. Barua, A., Y. Horie, and M. Zhou, *Microstructural level response of HMX-Estane polymer-bonded explosive under effects of transient stress waves.* Proceedings of the Royal Society a-Mathematical Physical and Engineering Sciences, 2012. **468**(2147): p. 3725-3744.

158. Sundararaman, V. and S.K. Sitaraman, *Determination of Fracture Toughness for Metal/Polymer Interfaces.* Journal of Electronic Packaging, 1999. **121**(4): p. 275-281.

159. Gogulya, M.F., et al., *Mechanical sensitivity and detonation parameters of aluminized explosives.* Combustion Explosion and Shock Waves, 2004. **40**(4): p. 445-457.

160. Li, Y.-b., et al., *The effect of wax coating, aluminum and ammonium perchlorate on impact sensitivity of HMX*. Defence Technology, 2017. **13**(6): p. 422-427.

161. Gogulya, M., et al., *Explosive characteristics of aluminized HMX-based nanocomposites.* Combustion, Explosion, and Shock Waves, 2008. **44**(2): p. 198-212.

162. Dick, J.J., et al., *The Hugoniot and shock sensitivity of a plastic-bonded TATB explosive PBX 9502.* Journal of Applied Physics, 1988. **63**(10): p. 4881-4888.

163. Peterson, J.R., C.A. Wight, and M. Berzins, *Applying High-performance Computing to Petascale Explosive Simulations.* Procedia Computer Science, 2013. **18**: p. 2259-2268.

164. Starkenberg, J. and T.M. Dorsey, *An Assessment of the Performance of the History Variable Reactive Bum Explosive Initiation Model in the CTH Code*. 1998, Army Research Lab, Aberdeen Proving Ground, MD, USA.

165. Hardin, D.B., J.J. Rimoli, and M. Zhou, *Analysis of thermomechanical response of polycrystalline HMX under impact loading through mesoscale simulations.* AIP Advances, 2014. **4**(9): p. 097136.

166. Ramos, K., M. Cawkwell, and D. Hooks. *Defect characterization and the effect of pre-existing and shock-induced defects on the shock response of single crystal explosives*. in *17th Biennial International Conference of the APS Topical Group on Shock Compression of Condensed Matter*. 2011. Chicago, Illinois: Bulletin of the American Physical Society

167. Hua, C., et al., *Research on the Size of Defects inside RDX/HMX Crystal and Shock Sensitivity.* Propellants Explosives Pyrotechnics, 2013. **38**(6): p. 775-780.

168. Menikoff, R., Sewell, T.D., *Constituent properties of HMX needed for meso-scale simulaitons.* Los Alamos National Lab., 2001(Report LA-UR-00-3804-rev).

169. Herring, S.D., T.C. Germann, and N. Grønbech-Jensen, *Effects of void size, density, and arrangement on deflagration and detonation sensitivity of a reactive empirical bond order high explosive.* Physical Review B, 2010. **82**(21): p. 214108.

170. Yarrington, C., R.R. Wixom, and D.L. Damm, *Mesoscale Simulations Using Realistic Microstructure and First Principles Equation of State*. 2012, Sandia National Lab.(SNL-NM), Albuquerque, NM (United States).

171. Gibbs, T.R. and A. Popolato, *LASL Explosive Property Data*. 1980: University of California, Berkeley.

172. Garcia, F., K.S. Vandersall, and C.M. Tarver. *Shock initiation experiments with ignition and growth modeling on low density HMX*. in *Journal of Physics: Conference Series*. 2014. IOP Publishing.

173. Wei, Y., et al., *Integrated Lagrangian and Eulerian 3D microstructure-explicit simulations for predicting macroscopic probabilistic SDT thresholds of energetic materials.* Computational Mechanics, 2019.

174. Mulford, R.N. and D.C. Swift, *Mesoscale modelling of shock initiation in HMX-based explosives.* Shock Compression of Condensed Matter-2001, Pts 1 and 2, Proceedings, 2002. **620**: p. 415-418.

175. Tokmakoff, A., M.D. Fayer, and D.D. Dlott, *Chemical-Reaction Initiation and Hot-Spot Formation in Shocked Energetic Molecular Materials.* Journal of Physical Chemistry, 1993. **97**(9): p. 1901-1913.

176. Mader, C.L., *Numerical modeling of explosives and propellants (Chap. 4)*. Vol. 1. 1997: CRC press.

177. Mader, C.L., *Numerical modeling of detonations.* Los Alamos Series in Basic and Applied Sciences, Berkeley: University of California Press, 1979, 1979.